HIGH ASPECT RATIO MICROSTRUCTURE COUPLER

A Thesis Submitted to the

College of Graduate Studies and Research

In Partial Fulfillment of the Requirements

For the Degree of Master of Science

In the Department of Electrical and Computer Engineering

University of Saskatchewan

Saskatoon

By

Melissa Schaffer

Permission to Use

In presenting this thesis in partial fulfilment of the requirements for a Postgraduate degree from the University of Saskatchewan, I agree that the Libraries of this University may make it freely available for inspection. I further agree that permission for copying of this thesis in any manner, in whole or in part, for scholarly purposes may be granted by the professor or professors who supervised my thesis work or, in their absence, by the Head of the Department or the Dean of the College in which my thesis work was done. It is understood that any copying or publication or use of this thesis or parts thereof for financial gain shall not be allowed without my written permission. It is also understood that due recognition shall be given to me and to the University of Saskatchewan in any scholarly use which may be made of any material in my thesis.

Requests for permission to copy or to make other use of material in this thesis in whole or part should be addressed to:

Head of the Department of Electrical and Computer Engineering
University of Saskatchewan
Saskatoon, Saskatchewan, Canada
S7N 5A9

ABSTRACT

Couplers are one of the most frequently used passive devices in microwave circuitry. The main function of a coupler is to divide (or combine) a radio frequency signal into (from) two separate signals by a specific ratio and phase difference. With the need for smaller electronic devices, a reduction in the area of a distributed coupler would prove to be valuable. The purpose of this research is to develop, simulate, fabricate and test high aspect ratio microstructure couplers that are smaller in area than existing distributed couplers, and have comparable or better performance. One method used to reduce the area of a distributed coupler is to replace single or multiple transmission lines with lumped element equivalent circuits. One category of lumped elements that has not been extensively implemented is high aspect ratio lumped elements. High aspect ratio lumped elements fabricated with deep X-ray lithography are able to take advantage of using the vertical dimension, and reduce their planar area. In this thesis high aspect ratio lumped elements are used in the design of 3-dB microstructure couplers that show significant area reduction compared to equivalent distributed couplers.

The designs of the microstructure couplers were based on the lumped element equivalent circuits of a 3-dB branch-line and a 3-dB rat-race distributed coupler. Simulations were performed to determine the lumped element values that would provide the largest 3-dB bandwidth while still maintaining close to ideal coupling and through values, return loss bandwidth, isolation bandwidth, and phase. These lumped element values were then implemented in the microstructure coupler designs as high aspect ratio microstructure lumped elements. 3-D electromagnetic simulations were performed which verified that the structures behaved electrically as couplers. The microstructure couplers were designed to be 220 μm tall nickel structures with capacitance gap widths of 6 μm.

Fabrication of the microstructure couplers using deep X-ray lithography was performed by the microfabrication group at IMT/KIT in Karlsruhe, Germany. Before testing, detailed visual inspection and the etching of the structures was performed at the Canadian Light Source.

A total of five microstructure couplers were tested. Four of the tested couplers were based on the 3-dB branch-line coupler, and the fifth coupler was based on the 3-dB rat-race coupler. The microstructure branch-line design that had the best overall results was

fabricated on quartz glass substrate and had an operation frequency of 5.3 GHz. The 3-dB bandwidth of the coupler was measured to be better than 75.5% and extrapolated to be 95.0%. At the centre frequency the through and coupled values were -4.32 dB and -4.44 dB. The phase difference between the couplers output ports was designed to be 90.0° and was measured to be 95.8°. The ±5° phase bandwidth was measured to be 12.7% and the isolation bandwidth was 28.8%. The measured results from the other couplers were comparable to simulation results.

The main advantage of the microstructure coupler designs over existing distributed couplers is that the microstructure couplers show a significant area reduction. The branch-line microstructure designs were at least 85% smaller in area than their distributed equivalent on quartz glass. The rat-race microstructure design showed an area reduction of 90% when compared to its distributed equivalent on quartz glass.

ACKNOWLEDGEMENTS

I would like to thank my supervisor, Dr. David Klymyshyn for all of his guidance, support, encouragement and assistance throughout this project.

I would also like to thank Garth Wells and Darcy Haluzan, of the Canadian Light Source, for all of their efforts and assistance during the etching and testing of the fabricated microstructure couplers.

For providing advice on microfabrication, I would like to thank Dr. Sven Achenbach of the University of Saskatchewan.

I am also very grateful for all of the time and effort Dr. Martin Boerner, Stephanie Kissling and the microfabrication group at IMT/KIT spent on fabricating the microstructure coupler devices.

For providing financial assistance during this project I would like to acknowledge NSERC, the College of Engineering, and TRLabs.

In addition to financial assistance I would like to thank TRLabs for providing the simulation software, testing facility, and personnel required for this project. In particular I would like to thank Jack Hanson for his assistance with testing equipment, and Edwin Gono-Santosa for his assistance with inductor design.

Finally, I would like to thank my family and friends for all of their encouragement, and patience throughout this project. It means so much to me knowing that you are always cheering me on.

TABLE OF CONTENTS

LIST OF TABLES

LIST OF FIGURES

LIST OF ABBREVIATIONS

ADS	Advanced Design System
C	Capacitance
C	Coupling value
C	speed of light [meters/second]
D	gap size
DI	de-ionized
D-XRL	deep X-ray lithography
EDA	electronic design automation
EM	Electromagnetic
ESR	equivalent series resistance
F	frequency [Hz]
f_0	Centre frequency [Hz]
FEM	finite element method
H	Height
HF	Hydro-fluoric
HFSS	high frequency structure simulator
GSG	Ground signal ground
IC	integrated circuit
KIT	Karlsruhe Institute of Technology
KNMF	Karlsruhe Nano Micro Facility
L	Inductance
L	Length
MEMS	microelectromechanical systems
perfect E	perfect electric conductor
PMMA	Polymethylmethacrylate
Q	quality factor
RF	radio frequency
SEM	Scanning electron microscope
SOLT	short, open, load, thru
S-parameters	scattering parameters
XRL	X-ray lithography
Y	Admittance
Z	Impedance
Z_0	characteristic impedance
Bl	electrical length [radians]
E_0	permittivity of vacuum, 8.854×10^{-12} [F/m]
ε_r	relative permittivity
Λ	wavelength [meters]
Ω	angular frequency [radians/second]

CHAPTER 1
INTRODUCTION

1.1 Motivation

The demand for smaller electronic devices with increased functionality continues to provide challenges to radio frequency (RF) microwave hardware designers. Many microwave circuits require couplers. The 3-dB coupler is among the most frequently used passive devices in an RF band receiver/transmitter system [1]. As part of receiver/transmitter systems, couplers are used in microwave applications such as bandpass filters [2], phase shifters [3], and antenna array feeds [4], [5].

Conventional distributed couplers are often impractical to implement at low GHz frequencies due to the length of their transmission lines being wavelength dependant. A technique used to reduce the area of the conventional distributed coupler is to replace the distributed elements with lumped elements [3], [6]. Unfortunately in practice the lumped elements are non-ideal and the performance of the coupler circuit is degraded. Discrete lumped elements introduce parasitics into the coupler circuit and the required interconnections introduce loss. Also, at high frequencies the reactive elements available in integrated circuit (IC) technologies typically suffer from low quality (Q) factor.

Recently, high Q capacitors [7], [8] and inductors [9], [10] have been implemented with high aspect ratio (ratio of the maximum structure height to the smallest horizontal feature of the structure, in this case 20:1 or higher) RF microelectromechanical systems (MEMS). In these cases the microstructured lumped elements were fabricated directly on the substrate with a single thick metal layer process using deep X-ray lithography (XRL). If these were structurally compatible and fabricated together in a single metal layer, additional interconnections and jumper wires between the lumped components and signal lines could be eliminated, potentially resulting in a high performance circuit. Also, a coupler implemented with high aspect ratio lumped elements could have minimal loss, simple single mask, single

layer fabrication, and have a significant reduction in area compared to the conventional distributed coupler since the area would depend on the lumped elements size rather than on wavelength. Figure 1.1 illustrates the potential area reduction that microstructure lumped element circuits proposed in this thesis could provide for a coupler circuit. The dimensions of the distributed coupler are based on a quartz glass substrate and an operating frequency of 5.4 GHz. In this example, the area is reduced by approximately 85%.

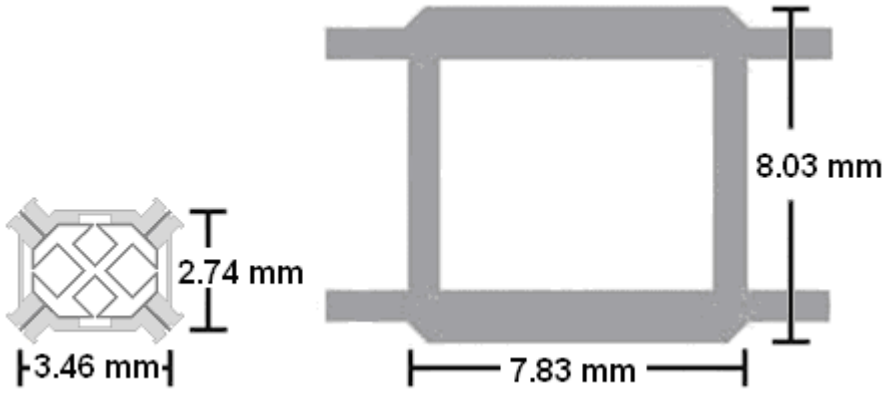

Figure 1.1: Example of Area Reduction Achievable using Microstructure Lumped Elements over Distributed Transmission Lines

1.2 Background and Literature Review

The objective of a 3-dB coupler design is to divide the input signal into two output signals that are equal to half of the power of the input signal. Typically a desired phase difference between the two output signals is also required. The microstructure couplers described and fabricated for this thesis were designed to have a 90° or 180° phase shift between the output signals.

Popular styles of coupler designs implemented in previous work include distributed couplers, lumped element couplers, and coupled line couplers [11], [12]. Distributed couplers such as the branch-line [11] in Figure 1.1 (right) or the rat-race [11] are perhaps the most popular, and are simply made from transmission lines (microstrip, stripline, etc.) of a length that is based on a centre frequency (wavelength dependant). Lumped element couplers are typically the lumped element equivalent of a distributed coupler. This is the approach taken in this thesis. Detailed analysis and comparison of distributed and lumped element branch-line and rat-race couplers is presented in Chapter 2.

Some coupler designs replace all of the transmission lines with lumped elements, but quasi lumped element hybrid couplers have also been designed in previous work [3] to reduce the area of a distributed coupler as shown in Figure 1.2.

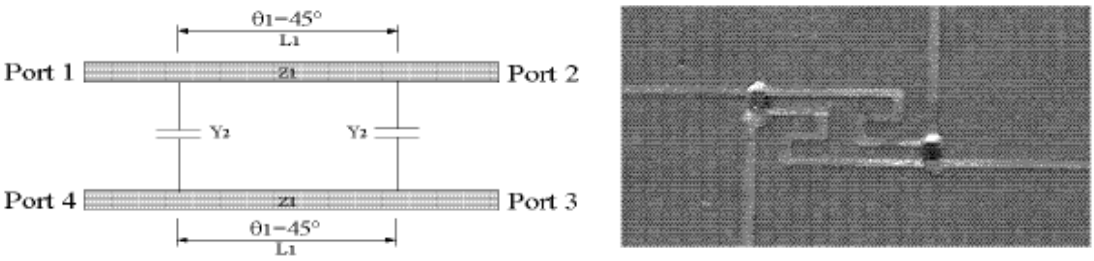

(a) (b)

Figure 1.2: (a) Schematic of Quadrature Quasi-Lumped Hybrid Coupler (b) Fabricated Quadrature Quasi-Lumped Hybrid Coupler from [3]

At the centre frequency the coupling (S_{21}) and throughput (S_{31}) signals are equal and at -3 dB as desired. The input reflection (return loss at Port 1) and the isolation (between ports 1 and 4) are both better than -25 dB at the centre frequency. Overall, the performance of the quasi-lumped coupler is closer to the performance of a coupled line coupler than to the purely distributed and purely lumped element couplers.

The simplest version of a coupled line coupler is constructed by placing two transmission lines in close proximity. One of the lines is provided with a signal and the signal is transferred to the second line through the separation gap between the two transmission lines. The strength of the transferred signal is proportional to the size of the separation gap and the coupling area (height and length) of the transmission line. An example of the classic planar coupled line coupler is shown in Figure 1.3.

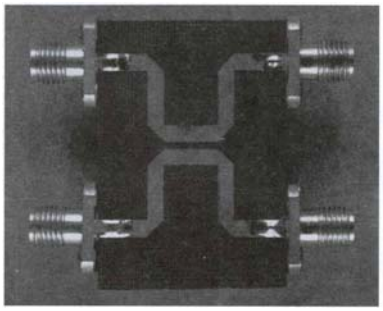

Figure 1.3: Single Stage Microstrip Coupled Line Coupler [11]

It is often difficult to achieve 3-dB coupling from coupled line couplers. Interdigital couplers, such as the Lange coupler [11], [12], use multiple lines in parallel to increase the coupling between edge-coupled lines. By using multiple lines the fringing fields at both edges of a line contribute to the coupling [11]. The disadvantage of the Lange coupler and interdigital couplers in general, is that the length of their transmission lines depends on wavelength, and since multiple coupled lines are being used their overall design is more complicated than the 3-dB branch-line hybrid coupler. Also, the jumper wires required for the connections of the multiple lines introduces loss into the coupler and complicates implementation.

One way to improve the coupling of coupled line couplers is to increase the height of the transmission lines to increase the coupling area. A high aspect ratio 3-dB coupled line coupler was designed, simulated, fabricated and tested in [13]. The high aspect ratio coupler used two quarter wavelength transmission lines that were 220 μm in height to achieve approximately 3-dB coupling at 18 GHz in simulation. The coupling performance results of the fabricated coupler were -4.07 dB at 18.2 GHz, with a 3-dB operating bandwidth of 6.8 GHz. An illustration of a section of the fabricated high aspect ratio coupler is shown in Figure 1.4.

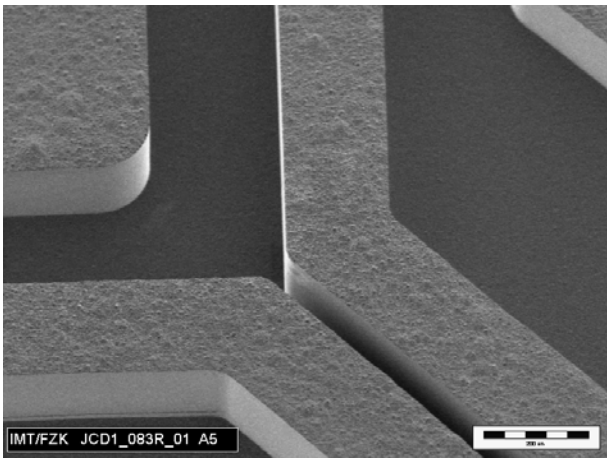

Figure 1.4: Section of a High Aspect Ratio 3-dB Coupled Line Coupler [13]

The advantage of the high aspect ratio 3-dB coupler is that it consumes less area than its Lange equivalent, and is able to achieve tight coupling using only two transmission lines. The disadvantage of the high aspect ratio coupler is the length of its transmission lines is dependent on wavelength.

The high aspect ratio 3-dB couplers were fabricated using deep X-ray lithography (D-XRL) with metal electroplating. More information on the fabrication process is provided in the next section.

1.3 Deep XRL Fabrication Process

The high aspect ratio microstructure couplers designed for this thesis were fabricated using deep XRL with metal electroplating at IMT/KIT in Karlsruhe Germany. The huge advantage that D-XRL has over other types of fabrication processes is the ability to achieve nearly vertical side walls, and high aspect ratios with a very low sidewall surface roughness [14]. Another advantage D-XRL fabrication provides for RF-MEMS devices is that it is non-silicon dependant and as a result a variety of functional materials can be used to fabricate the devices [15]. The final devices can range from electroplated metals and alloys to polymers, and ceramics, on a variety of dielectric substrates.

There are many steps involved in deep X-ray lithography. Some of the initial steps include selecting the type of resist (positive or negative tone), and fabricating the mask. After X-ray exposure positive tone resist is dissolvable in the exposed areas, where negative tone resist is dissolvable in the unexposed areas.

The two main types of resist used in the D-XRL process for the fabrication of RF-MEMS devices are Polymethyl-methacrylate (PMMA), which is a positive resist, and Epon SU-8, which is a negative resist. The advantage of using PMMA is that after exposure it is easily dissolvable in developers. A disadvantage of PMMA is that it requires high exposure doses. Epon SU-8 is more sensitive to exposure than PMMA which results in lower exposure doses (300 times smaller than that of PMMA [16]) and shorter exposure times (about 20 times shorter than that of PMMA [16]). The disadvantage of using Epon SU-8 is that it is extremely difficult to remove the exposed resist, which is required for metal RF devices.

After fabricating the mask for the device, the main steps that were performed for the fabrication of the microstructure coupler were exposure, development, electroforming, and resist stripping. Each of these steps is illustrated in Figure 1.5 and is explained briefly.

1) Exposure

   During exposure X-rays from a synchrotron radiation source are used to transfer the pattern on the mask to the resist. The X-rays cause chemical bonds to be broken in

polymer chains of positive tone resists so the exposed areas become dissolvable by a developer. Crosslinking of polymer chains in negative tone resists is produced by the X-rays which causes the exposed areas to become un-dissolvable by the developer.

2) Development

Development is dissolving the unwanted areas of the resist by placing the exposed wafer into a special chemical called a developer. The unwanted areas of the resist must be completely dissolved to expose the metal seed layer. For positive tone resist (used in the fabrication of the couplers for this thesis), the exposed areas of the resist are dissolved. When negative tone resist is used the unexposed areas of the resist are dissolved.

3) Electroforming

During electroforming metal is deposited into the voids of the resist of the developed wafer, starting at the metal seed layer. This process of depositing metal is called electroplating. Electroplating occurs in a chemical solution that contains metal ions (also called an electrolytic solution). The wafer is connected to a cathode, which is then submersed in the electrolytic solution along with an anode. A voltage is applied between the anode and the cathode to induce an electric field in the solution. The electric field causes the metal ions to travel towards the cathode and become deposited onto the conductive areas of the developed wafer. Electroplating continues until the desired metal height is achieved for the device. The growth rate of the metal is approximately a few microns per hour.

4) Resist stripping

Resist stripping is the process of removing the resist that was not dissolved during development. One way to remove the positive tone resist is to expose the entire wafer with synchrotron radiation (flood exposure) and then develop it. For removing negative tone resist the entire wafer can be placed into a plasma ashing machine, to remove the left over resist or chemical etching can be used. Removing exposed negative tone resist, such as SU-8, is very difficult compared to removing positive tone resist, such as PMMA.

A more detailed description of each of the steps involved in the D-XRL fabrication process can be found in [17].

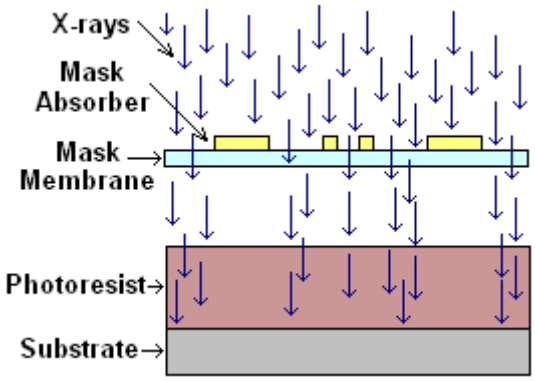

(a)

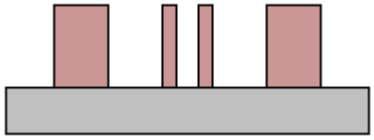

(b)

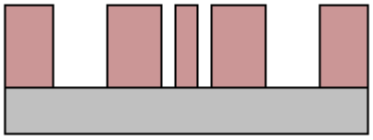

(c)

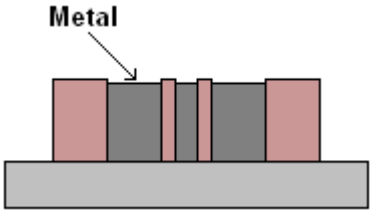

(d)

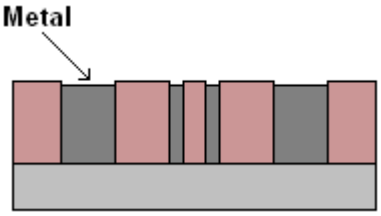

(e)

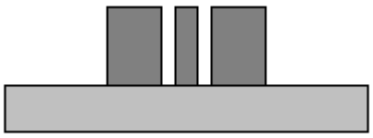

(f)

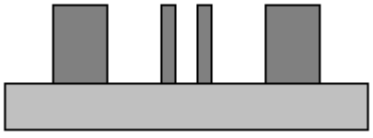

(g)

Figure 1.5: Deep XRL Process - (a) Exposure, (b) Positive Tone Resist Development, (c) Negative Tone Resist Development, (d) & (e) Electroforming, (f) & (g) Resist Stripping

1.4 Research Objectives

The purpose of this research is to develop, simulate, fabricate and test high aspect ratio 3-dB couplers that are smaller in area than existing distributed couplers. The 3-dB coupler design is to incorporate microstructure lumped elements. A single metal layer design is required so that a single exposure thick metal D-XRL process can be used for fabrication. The main objectives of this research are to:

1) Review existing 3-dB coupler designs with a focus on distributed and lumped element designs. Compare the performance between the distributed and lumped element couplers and determine the values for a lumped element 3-dB coupler that will maximize the 3-dB bandwidth and still have acceptable return loss and isolation between the input and unused port at the centre frequency of the coupler.
2) Review the theory and design of high aspect ratio lumped element microstructures fabricated by D-XRL and the limitations of this fabrication process.
3) Design 3-dB microstructure couplers based on the lumped element designs that achieve the greatest 3-dB bandwidth, and the high aspect ratio lumped element microstructures.
4) Fabricate sample microstructure couplers with D-XRL.
5) Test the microstructure couplers and compare their performance with simulation results.

1.5 Thesis Organization

This thesis is organized into five chapters. Chapter 2 covers a comparison between ideal distributed, ideal lumped, and the implemented lumped element couplers, with the implemented lumped element coupler being used as the base design for the microstructure couplers. The lumped element values of the implemented lumped element coupler are slightly different from the ideal lumped element coupler and provide the largest 3-dB bandwidth over the ideal distributed and ideal lumped coupler styles, while experiencing a trade off of smaller isolation or phase bandwidth.

Chapter 3 provides the background on existing designs of microstructure capacitors and inductors. The simulated performance of the inductors and capacitors designed for the microstructure couplers are provided. Also in chapter 3, the design of two different styles of

microstructure couplers are revealed and the simulated performance is discussed. The performance of the microstructure couplers is then compared to the performance of ideal and implemented lumped element couplers. The chapter is completed with the description of the key advantages and disadvantages of the microstructure design over the distributed design.

In chapter 4 the fabrication and test results of the branch-line and rat-race microstructure couplers are provided. This chapter includes the mask layout of the microstructure couplers, explains the testing procedures used and the results achieved.

The final chapter of this thesis is chapter 5. The performance results of the microstructure couplers are discussed and the future work involved in this project is described.

CHAPTER 2
DISTRIBUTED AND LUMPED ELEMENT COUPLER PERFORMANCE AND OPTIMIZATION

2.1 Coupler Background

The general symbol used in this thesis to represent a coupler is shown in Figure 2.1. Port 1 is the input port, ports 2 and 3 are the output ports, and port 4 is the isolated port and ideally has no output signal. The couplers discussed in this thesis will use the configuration of port 2 as the through output, and port 3 as the coupled output.

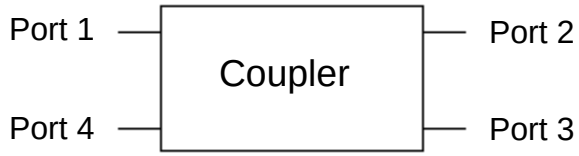

Figure 2.1: General Coupler Symbol

Important factors used to characterize couplers are coupling, through, isolation, and directivity as shown in equations 2.1 to 2.4, where P_1 is the power of the input signal (at port 1), P_2, P_3, and P_4 represent the power of the output signal at ports 2, 3 and 4 respectively. The relationship to the S-parameters of the coupler is also provided in these equations. Similar equations can be found in [11].

$$\text{Coupling (dB): } C = 10\log\left(\frac{P_1}{P_3}\right) = -20\log|S_{13}| \tag{2.1}$$

$$\text{Through (dB): } T = 10\log\left(\frac{P_1}{P_2}\right) = -20\log|S_{12}| \tag{2.2}$$

$$\text{Isolation (dB): } I = 10\log\left(\frac{P_1}{P_4}\right) = -20\log|S_{14}| \tag{2.3}$$

$$\text{Directivity (dB): } D = 10\log\left(\frac{P_3}{P_4}\right) = 20\log\frac{|S_{13}|}{|S_{14}|} \tag{2.4}$$

The coupling value, *C*, is the ratio of the input and coupled output signal power in decibels (dB) and also determines some of the values for the coupler's Scattering parameters (S-parameters) matrix. An example of a common coupling value is 3 dB. When 3 dB coupling is achieved the input signal is split equally into two signals where the signals at the coupled output (port 3) and the through output (port 2) are equal to half of the power of the input signal. The couplers in this thesis were designed to be 3-dB couplers.

The through value, *T*, of a coupler is a measure of the ratio of the input and through output signal power in dB.

The isolation of a coupler describes the amount of power that is present at the isolated port (port 4) in comparison to the input port (port 1). Ideally the output power at the isolated port should be zero, making the ideal value of isolation in dB infinite.

The directivity of a coupler is another measure of isolation except that it uses the output power of port 3 and port 4. Ideally directivity should be infinite in dB since ideally the output power at the isolated port should be zero.

S-parameters represent the ratios of output voltage waves to incident voltage waves at a device port while the remaining ports are terminated in a matched load to the system impedance (Z_0). The S-parameters of a coupler are used to determine the performance characteristics (coupling, isolation, various bandwidths, etc). For a four port coupler the general S-parameter matrix, [S], is represented by:

$$[S] = \begin{bmatrix} S_{11} & S_{12} & S_{13} & S_{14} \\ S_{21} & S_{22} & S_{23} & S_{24} \\ S_{31} & S_{32} & S_{33} & S_{34} \\ S_{41} & S_{42} & S_{43} & S_{44} \end{bmatrix}$$

where S_{21}, for example, is defined as the ratio of the output voltage wave at port 2 to the input voltage wave at port 1, while all ports (including 3 and 4) are terminated in matched loads.

Due to symmetry of some coupler types, the S-parameter matrix can be simplified as discussed in the next section.

Important bandwidths used to characterize the performance of a coupler are the 3-dB bandwidth, isolation bandwidth and phase bandwidth. The frequency ranges of these bandwidths always include the centre frequency of the coupler. In this thesis the bandwidths

are unit-less since they are expressed as a percentage of the centre frequency. The 3-dB bandwidth is normally defined as the frequency range where the magnitudes of S_{21} (through) and S_{31} (coupled) are 3 dB less than the magnitude of S_{21} and S_{31} at the centre frequency. For a 3-dB coupler the frequency range ideally occurs when the magnitudes of S_{21} and S_{31} reach -6 dB. The isolation bandwidth is the frequency range where the isolation is equal to or better than a defined level. For this thesis, the level is assumed to be -15 dB. Ideally, isolation has the value of $-\infty$ dB at the centre frequency. The phase bandwidth is the frequency range where the value of the phase difference between the outputs of the coupler is within $\pm 5°$ of the phase difference between the couplers outputs at the centre frequency. The 3-dB, isolation, and phase bandwidths will be used repeatedly in this thesis to compare various 3-dB coupler designs.

2.2 Existing Directional Coupler Designs

Two types of couplers are discussed in this section, the 90° hybrid (branch-line) coupler and the 180° hybrid (rat-race) coupler. The performance of both coupler styles in lumped element and distributed form is also shown.

2.2.1 Distributed Couplers

Distributed couplers are very popular and easy to implement. The microstrip layouts of the branch-line and rat-race coupler are shown in Figure 2.2 and Figure 2.3. Similar microstrip layouts can be found in [11] and [12]. The characteristic impedances of the transmission lines in the branch-line coupler are represented by Z_1 and Z_2, and Z_0 represents the characteristic impedance of the system. Similarly for the rat-race coupler Z_a and Z_b represent the characteristic impedances of the transmission lines, and Z_0 represents the characteristic impedance of the system.

The impedances Z_1, Z_2, Z_a, and Z_b are related to the coupling value of the coupler. Equations 2.5 to 2.8 are provided for calculating Z_1 and Z_2 for the branch-line coupler and equations 2.9 to 2.10 are provided for calculating Z_a and Z_b for the rat-race coupler, where C is the desired coupling value obtained from equation (2.1). Similar equations can be found in [11] and [12].

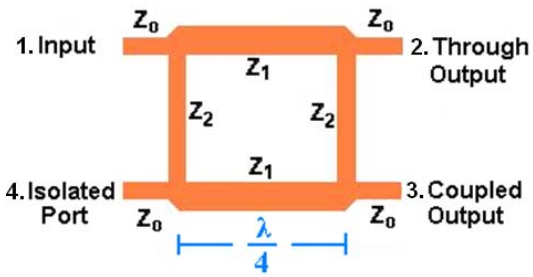

Figure 2.2: Microstrip Layout of a Branch-Line Coupler

$$|S_{31}| = 10^{\frac{-C}{20}} \tag{2.5}$$

$$|S_{21}| = \sqrt{1 - |S_{31}|^2} \tag{2.6}$$

$$Z_1 = Z_0 |S_{21}| \tag{2.7}$$

$$Z_2 = \frac{Z_1}{|S_{31}|} \tag{2.8}$$

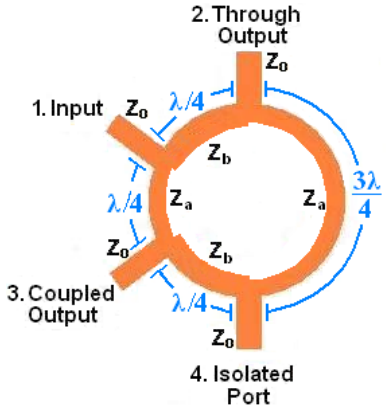

Figure 2.3: Microstrip Layout of a Rat-Race Coupler

$$Z_a = \frac{Z_0}{|S_{31}|} \tag{2.9}$$

$$Z_b = \frac{Z_0}{|S_{21}|} \tag{2.10}$$

Due to symmetry, the S-parameter matrix of the branch-line coupler and the rat-race coupler can be simplified as shown below where port 1 is the input, ports 2 and 3 are the outputs and port 4 is isolated. The simplified S-parameter matrices are valid for any frequency.

$$[S_{branch-line}] = \begin{bmatrix} S_{11} & S_{21} & S_{31} & S_{41} \\ S_{21} & S_{11} & S_{41} & S_{31} \\ S_{31} & S_{41} & S_{11} & S_{21} \\ S_{41} & S_{31} & S_{21} & S_{11} \end{bmatrix} \qquad [S_{rat-race}] = \begin{bmatrix} S_{11} & S_{21} & S_{31} & S_{41} \\ S_{21} & S_{44} & S_{41} & S_{42} \\ S_{31} & S_{41} & S_{11} & S_{21} \\ S_{41} & S_{42} & S_{21} & S_{44} \end{bmatrix}$$

The ideal S-parameter equations of the 3-dB branch-line and 3-dB rat-race couplers were derived from even and odd mode network analysis [6], [11] to determine the ABCD parameters of the couplers, then the ABCD parameters were converted to S-parameters. The magnitudes (dB) of the S-parameter equations are plotted vs. normalized frequency in Figure 2.4 and Figure 2.5. The equations are provided in Appendix A due to their length.

If Figure 2.4 and Figure 2.5 were extended to higher frequencies the re-entrant behavior of the distributed couplers would be shown. This means that from 2.5 f_0 to 3.5 f_0 the S-parameter performance would be basically the same as shown in Figure 2.4 and 2.5 since the period of the coupler is $2f_0$.

The ideal phase difference between the output ports (2 and 3) of the distributed branch-line coupler with port 1 as the input, output ports (2 and 3) of the distributed rat-race coupler with port 1 as the input, and the output ports (2 and 3) of the distributed rat-race coupler with port 4 as the input is shown in Figure 2.6 to Figure 2.8.

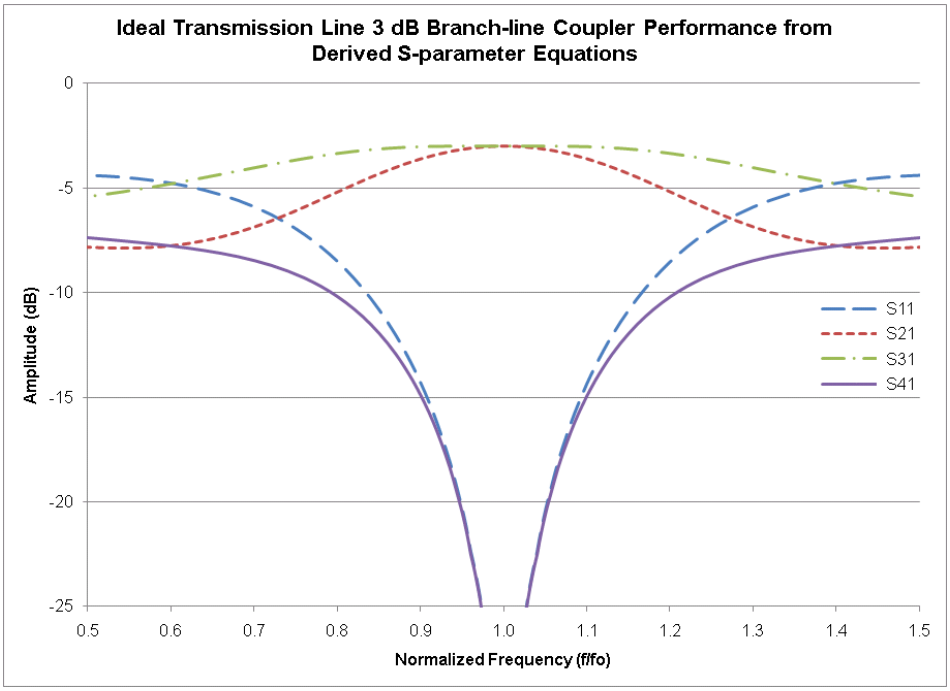

Figure 2.4: Ideal Magnitudes of S-Parameters of a 3-dB Distributed Branch-line Coupler

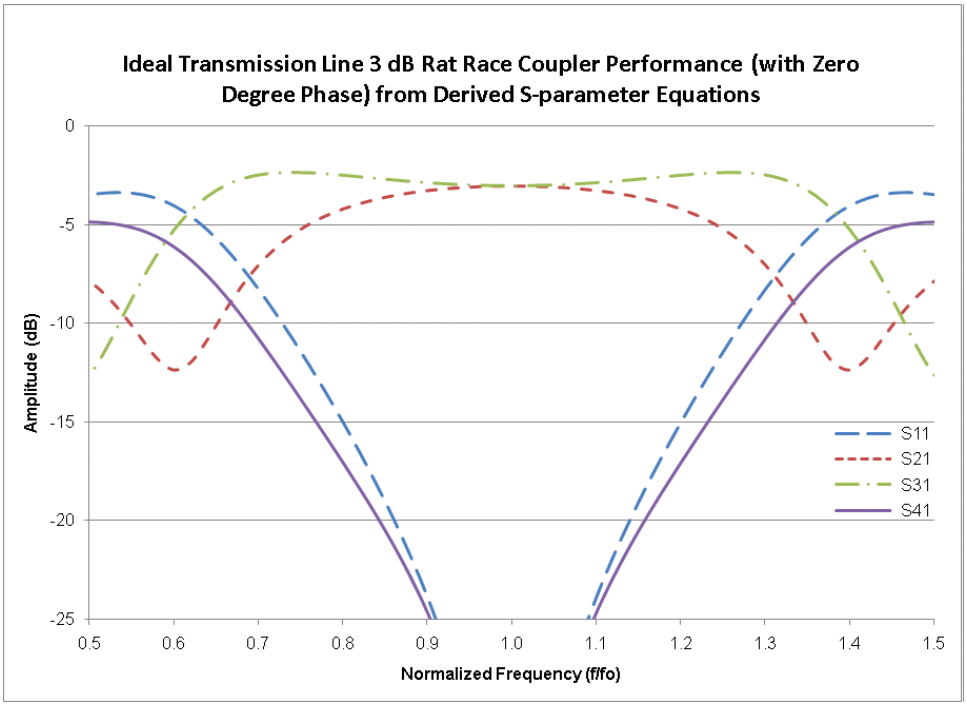

Figure 2.5: Ideal Magnitudes of S-Parameters of the 3-dB Distributed Rat-Race Coupler

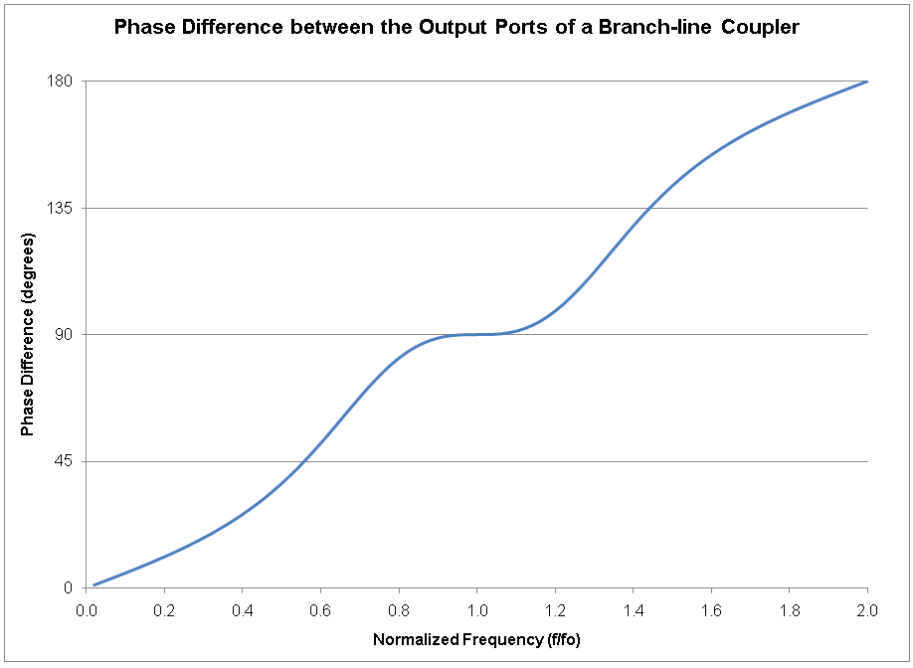

Figure 2.6: Ideal Phase Difference between the Output Ports (2 and 3) of a Distributed Branch-line Coupler

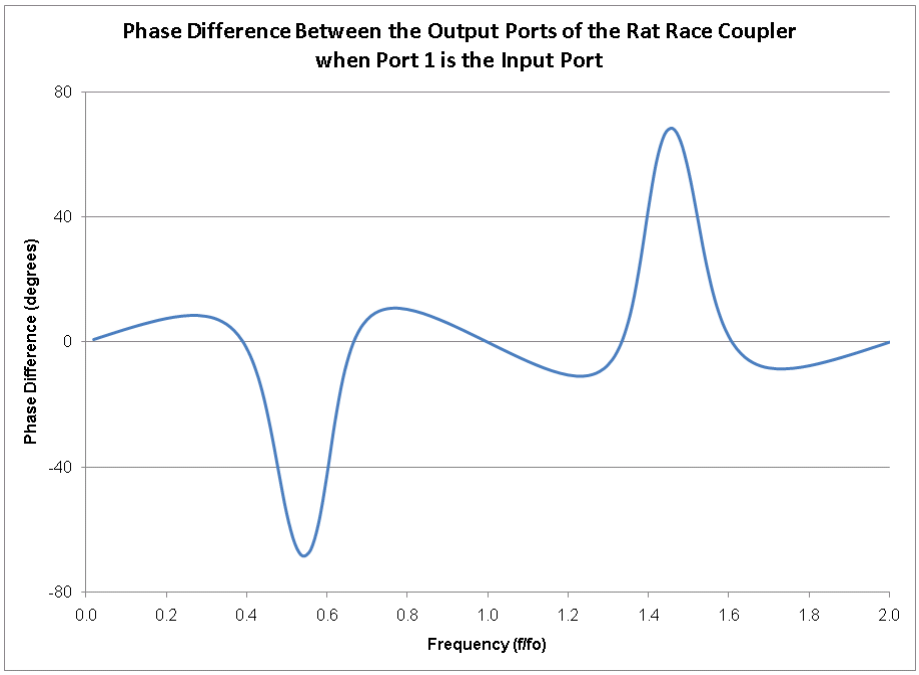

Figure 2.7: Ideal Phase Difference between the Output Ports (2 and 3) of the Distributed Rat-Race Coupler when Port 1 is the Input Port

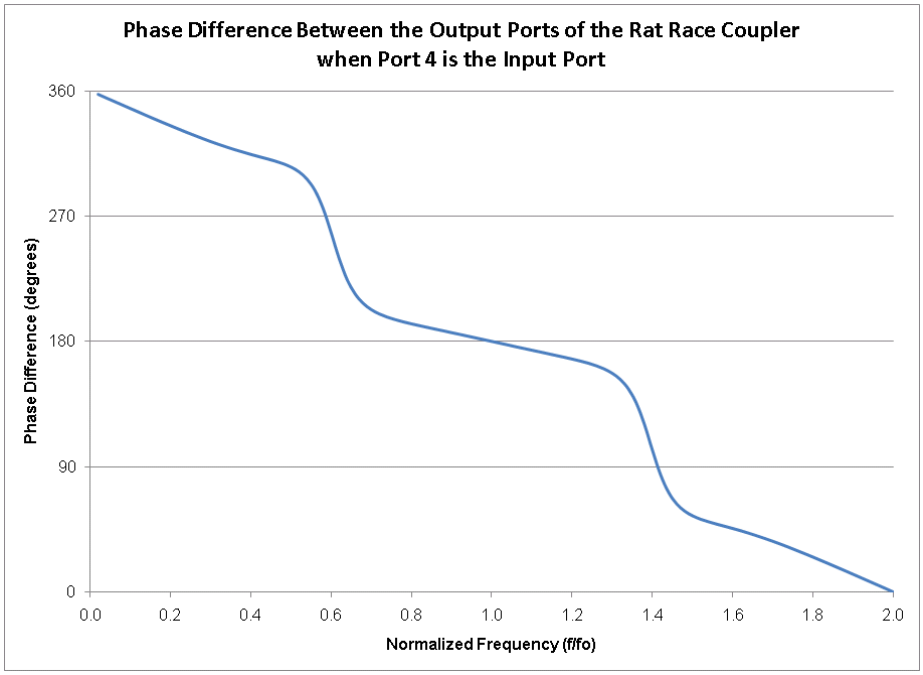

Figure 2.8: Ideal Phase Difference Between the Output Ports (2 and 3) of a Distributed Rat-Race Coupler when Port 4 is the Input Port

The phase of the output signals from the couplers depends on the length of the transmission lines with respect to the operating frequency. Due to the symmetry of the branch line coupler having each transmission line length equal $\frac{\lambda}{4}$ at the centre frequency, the output signals will always be 90° out of phase from each other no matter which port is used as the input. The rat-race coupler can achieve two different phase differences depending on which port is used as the input due to the transmission lines being $\frac{\lambda}{4}$ or $\frac{3\lambda}{4}$ in length at the centre frequency. If port 1 is used as the input, the output ports are ports 2 and 3 and the phase difference between the output ports is 0°. If port 4 is the input port, ports 2 and 3 are the output ports and the phase difference between the outputs is 180° at the centre frequency.

The similarities between the performance of the branch-line and rat-race couplers are they both achieve 3-dB coupling at the centre frequency and have excellent return loss and isolation. In this thesis the 3-dB bandwidth was calculated based on the smallest frequency span where the $|S_{21}|$ and $|S_{31}|$ are 3 dB less than their value at the centre frequency. Figure 2.9 provides an example of how the 3-dB bandwidth of a coupler is determined.

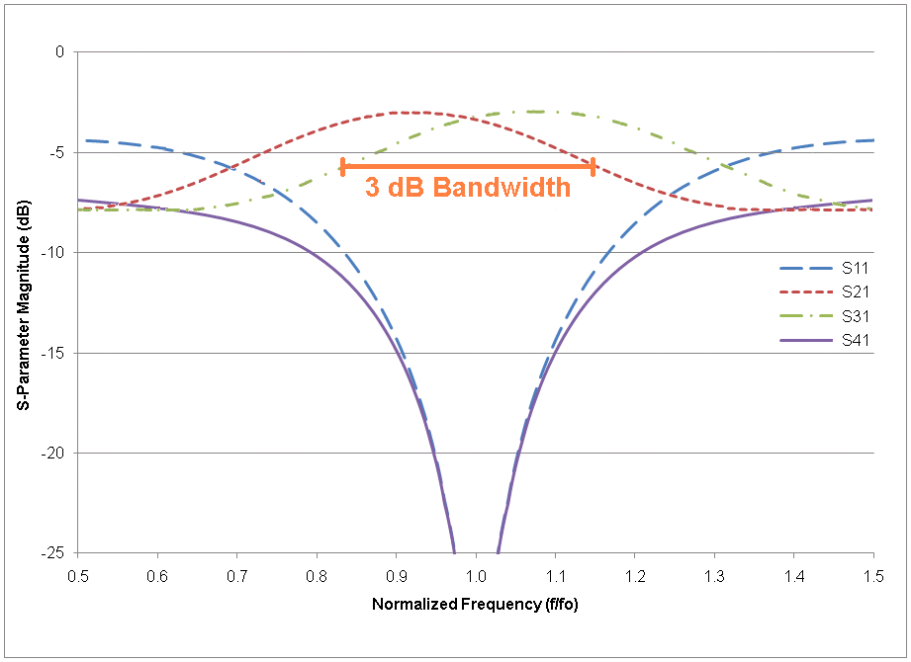

Figure 2.9: 3-dB Bandwidth Example

The difference in performance between the rat-race and branch-line couplers is that the rat-race coupler has larger 3-dB bandwidth of 55.2% vs. 49.2%, and isolation bandwidth of 46.4% vs. 19.6%, but a smaller ±5° phase bandwidth of 16% vs. 32.8%.

The area of a distributed coupler such as the branch-line or rat-race coupler is wavelength dependant. Due to the dependency on wavelength the only way to decrease the area of a distributed coupler is to increase the dielectric constant (relative permittivity, ε_r) of the substrate to reduce the wavelength at the centre frequency as shown in equation 2.11

$$\lambda = \frac{c}{f\sqrt{\varepsilon_r}}, \tag{2.11}$$

where λ is the wavelength, c is the speed of light, f is the centre frequency, and ε_r is the relative permittivity of the substrate. Lumped element couplers do not have this strict dependency on wavelength. Instead the area of these couplers depends on the area of the lumped elements. Lumped element couplers are explained in the next section.

2.2.2 Lumped Element Couplers

Lumped element couplers can be used as a replacement for distributed couplers. The values of the lumped elements can be derived by replacing each of the transmission lines of the distributed coupler by a lumped element equivalent circuit. Four possible ideal lumped element equivalent circuits used to replace a transmission line are shown in Figure 2.10. In order from left to right the lumped element equivalent circuits are the low pass π, high pass π, low pass T and high pass T.

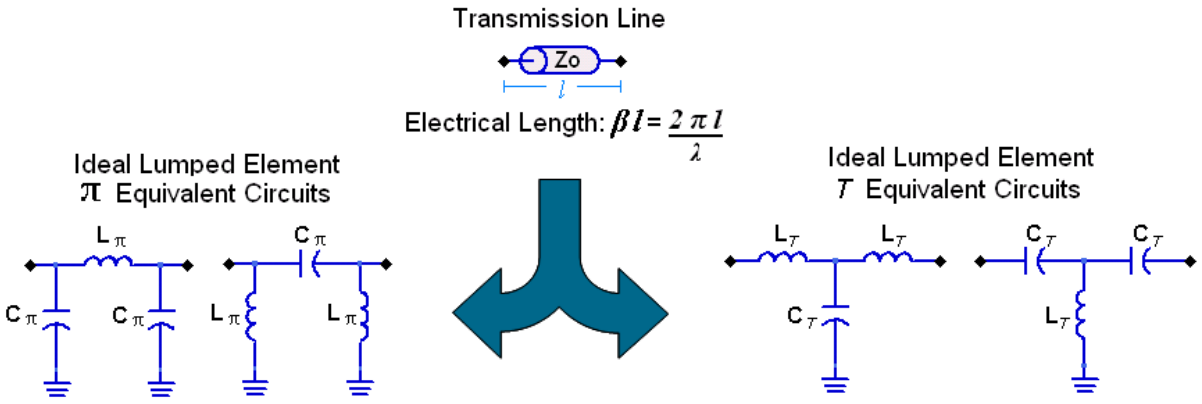

Figure 2.10: Lumped Element Equivalent Circuits of a Transmission Line

The lumped element equivalent circuit values (L's and C's) are derived from using two port network analysis and equating the ABCD parameters of a transmission line with the ABCD parameters of π and T networks, similar to the technique used in [18].

The equations and the ABCD matrices used to find the C_π and L_π values of the low pass π model are shown below.

$$[ABCD]_{TL} = \begin{bmatrix} \cos\beta l & jZ_0 \sin\beta l \\ jY_0 \sin\beta l & \cos\beta l \end{bmatrix} \tag{2.12}$$

$$[ABCD]_{LP\_\pi\_Model} = \begin{bmatrix} 1 & 0 \\ Y_C & 1 \end{bmatrix} \begin{bmatrix} 1 & Z_L \\ 0 & 1 \end{bmatrix} \begin{bmatrix} 1 & 0 \\ Y_C & 1 \end{bmatrix} \tag{2.13}$$

After matrix multiplication the ABCD parameters of the low pass π model are:

$$[ABCD]_{LP\_\pi\_Model} = \begin{bmatrix} 1+Y_C Z_L & Z_L \\ Y_C(2+Y_C Z_L) & 1+Y_C Z_L \end{bmatrix}. \tag{2.14}$$

Equating the A, B and D parameters of the transmission line and low pass π model and solving for Y_C and Z_L. yields:

$$Z_L = jZ_0 \sin\beta l \tag{2.15}$$

$$Y_C = \frac{\cos\beta l - 1}{Z_L}. \tag{2.16}$$

Substituting $Y_C = j\omega C$ and $Z_L = j\omega L$, (where $\omega = 2\pi f_0$ and f_0 is the centre frequency) and solving for L and C of the low pass π model yields:

$$L_{LP\_\pi} = \frac{Z_0 \sin\beta l}{\omega} \tag{2.17}$$

$$C_{LP\_\pi} = \frac{1-\cos\beta l}{\omega^2 L_{LP\_\pi}}, \tag{2.18}$$

where Z_0 is the characteristic impedance of the transmission line.

Equating the C parameters of the transmission line and low pass π model and substituting $Y_C = j\omega C$, $Z_L = j\omega L$, and equation 2.18 in for C yields:

$$L_{LP\_\pi} = \frac{Z_0(\cos\beta l + 1)\tan\frac{\beta l}{2}}{\omega}, \tag{2.19}$$

which provides equivalent results of L_{LP_π} to equation 2.17 for all βl except for $\beta l = \pi$ or multiples of π.

The performance of a lumped element coupler will be equal to the performance of a distributed coupler at the centre frequency, since the lumped element value calculations are based on the value of the characteristic impedance of the equivalent transmission line at the centre frequency. At frequencies other than the centre frequency the performance of the two coupler styles will begin to differ as the frequency moves away from the centre frequency. This is because the equivalent lumped elements will vary with frequency as shown in equations 2.17 to 2.19. The major difference between the lumped element couplers and the distributed couplers is that the lumped element coupler will not have re-entrant behavior. Section 2.4 investigates the equivalency of the lumped element and distributed coupler and compares the bandwidths of both coupler styles.

As shown in the equations of L and C for the low pass π model, the values of inductance and capacitance depend on the electrical length of the transmission line, βl. Some electrical lengths result in invalid L and C values, since L or C become negative. Table 2.1 shows examples of βl values and if the resulting L and C values are valid.

Table 2.1: Capacitor and Inductor Values of the Low Pass π Model for Different Electrical Lengths of Transmission Line

Bl (radians)	C_{LP_π}	L_{LP_π}	*Result*
π/4	Positive	Positive	Valid L and C for βl
π/2	Positive	Positive	Valid L and C for βl
3π/4	Positive	Positive	Valid L and C for βl
π	Infinite	Zero	Invalid L and C for βl
5π/4	Negative	Negative	Invalid L and C for βl
3π/2	Negative	Negative	Invalid L and C for βl
7π/4	Negative	Negative	Invalid L and C for βl
2π	Infinite	Zero	Invalid L and C for βl

The equations for the lumped element values of the other lumped element equivalent circuits from Figure 2.10 also were determined and had ranges of transmission line lengths that were invalid. It was also found in [18] that the lumped equivalent low pass π models of

a transmission line were preferred over the high pass π models because using fewer inductors resulted in a circuit that had less loss. Based on the invalid regions and the preference to using the minimum amount of inductors the lumped element equivalent circuit used to replace $\frac{\lambda}{4}$ is shown in Figure 2.11 (a). Figure 2.11 (b) shows the lumped element equivalent circuit to replace a $\frac{3\lambda}{4}$ transmission line.

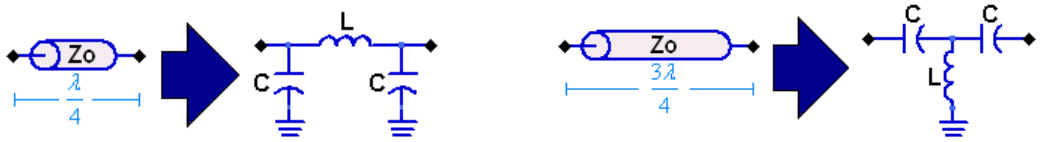

(a) (b)

Figure 2.11: (a) Quarter Wavelength Transmission Line and Lumped Element Equivalent
(b) Three Quarter Wavelength Transmission Line and Lumped Element Equivalent

The derivation of L_T and C_T equations of the high pass T-model are provided in equations 2.20 to 2.26 and begins with equating the ABCD parameters of the high pass T-model (equation 2.21) to the ABCD parameters of a transmission line (equation 2.12).

$$[ABCD]_{HP\_T\_Model} = \begin{bmatrix} 1 & Z_C \\ 0 & 1 \end{bmatrix} \begin{bmatrix} 1 & 0 \\ Y_L & 1 \end{bmatrix} \begin{bmatrix} 1 & Z_C \\ 0 & 1 \end{bmatrix} \tag{2.20}$$

After matrix multiplication the ABCD parameters of the high pass T-model are:

$$[ABCD]_{HP\_T\_Model} = \begin{bmatrix} 1+Z_C Y_L & Z_C(2+Z_C Y_L) \\ Y_L & 1+Z_C Y_L \end{bmatrix}. \tag{2.21}$$

Equating the A, C and D parameters of the transmission line and high pass T-model and solving for Y_L. and Z_C results in:

$$Y_L = jY_0 \sin \beta l \tag{2.22}$$

$$Z_C = \frac{\cos \beta l - 1}{Y_L}. \tag{2.23}$$

Substituting $Y_L = \frac{-j}{\omega L}$ and $Z_C = \frac{-j}{\omega C}$, (where $\omega = 2\pi f_0$ and f_0 is the centre frequency) and solving for L and C of the high pass T-model yields:

$$L_{HP\_T} = \frac{-1}{\omega Y_0 \sin \beta l} \tag{2.24}$$

$$C_{HP\_T} = \frac{-1}{\omega^2 L_{HP\_T} (\cos \beta l - 1)} \tag{2.25}$$

where Y_0 is the characteristic admittance of the transmission line.

Equating the B parameters of the transmission line and high pass T-model and substituting $Y_L = \frac{-j}{\omega L}$ and $Z_C = \frac{-j}{\omega C}$ and equation 2.23 in for Z_C, followed by trigonometric substitution to simplify the expression yields:

$$L_{HP\_T} = \frac{-Z_0}{\omega(\cos \beta l + 1) \tan \frac{\beta l}{2}}, \tag{2.26}$$

which provides equivalent results of L_{HP_T} to equation 2.24 for all βl except for $\beta l = \pi$ or multiples of π.

The lumped element equivalent circuits of the distributed branch-line and rat-race couplers were based on the lumped element equivalent circuits for the $\frac{\lambda}{4}$ and $\frac{3\lambda}{4}$ transmission lines and are shown in Figure 2.12 and Figure 2.13.

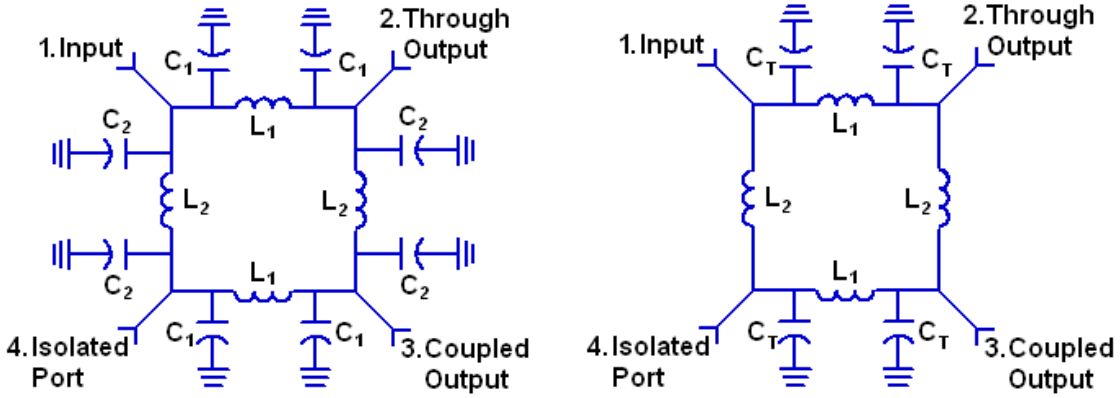

Figure 2.12: (a) Lumped Element Branch-line Coupler, (b) Simplified Lumped Element Branch-line Coupler where C_T is Equal to the Sum of C_1 and C_2

The equations used to calculate the value of inductors and capacitors in Figure 2.12 are based on the equations 2.17 to 2.19 of the low pass π model equivalent circuit of a transmission line. In the case of the lumped element branch-line coupler shown in Figure 2.12, the lumped element low pass π model equivalent circuits replaced $\frac{\lambda}{4}$ transmission line lengths. The $\frac{\lambda}{4}$ length provides a βl of $\frac{\pi}{2}$, which causes the trigonometric terms in equations 2.17 to 2.19 to reduce to 0's and 1's, resulting in equations 2.27 to 2.31, where Z_1 and Z_2 represent the characteristic impedance of the equivalent transmission line.

$$L_1 = \frac{Z_1}{2\pi f_0} \tag{2.27}$$

$$L_2 = \frac{Z_2}{2\pi f_0} \tag{2.28}$$

$$C_1 = \frac{1}{Z_1 2\pi f_0} \tag{2.29}$$

$$C_2 = \frac{1}{Z_2 2\pi f_0} \tag{2.30}$$

$$C_T = C_1 + C_2 \tag{2.31}$$

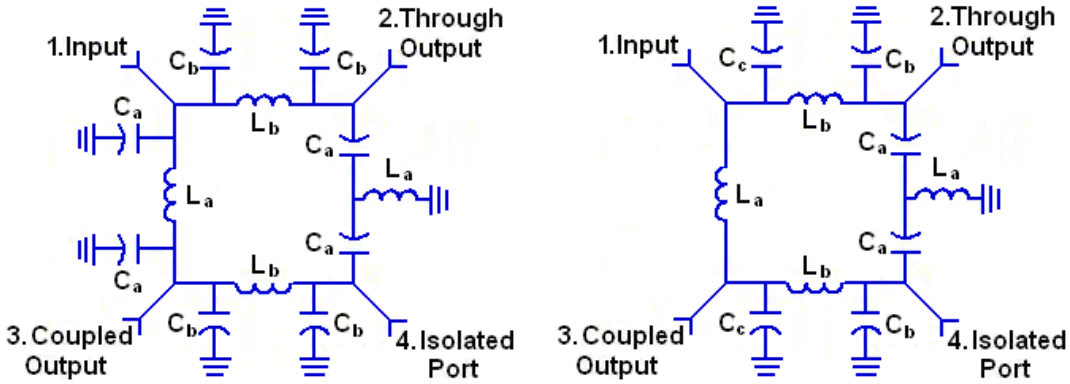

(a) (b)

Figure 2.13 : (a) Lumped Element Rat-Race Coupler, (b) Simplified Lumped Element Rat-Race Coupler where C_c is Equal to the Sum of C_a and C_b

The equations used to calculate the value of the inductors and capacitors in Figure 2.13 are based on equations 2.17 to 2.19 and 2.24 to 2.26. The lumped element low pass π

equivalent circuits replaced $\frac{\lambda}{4}$ transmission line lengths and the lumped element high pass T-equivalent circuits replaced $\frac{3\lambda}{4}$ transmission line lengths of the distributed rat-race coupler. The $\frac{\lambda}{4}$ and $\frac{3\lambda}{4}$ transmission line lengths created βl's of $\frac{\pi}{2}$ and $\frac{3\pi}{2}$, which caused the trigonometric terms in equations 2.17 to 2.19 and 2.24 to 2.26 to reduce to 0's and 1's, resulting in equations 2.32 to 2.36,.where Z_a and Z_b represent the characteristic impedance of the equivalent transmission line.

$$L_a = \frac{Z_a}{2\pi f_0} \tag{2.32}$$

$$L_b = \frac{Z_b}{2\pi f_0} \tag{2.33}$$

$$C_a = \frac{1}{Z_a 2\pi f_0} \tag{2.34}$$

$$C_b = \frac{1}{Z_b 2\pi f_0} \tag{2.35}$$

$$C_c = C_a + C_b \tag{2.36}$$

Section 2.3 discusses the performance of the ideal lumped element coupler, and Section 2.4 investigates the equivalency of the distributed and lumped element couplers and compares the performance between the two coupler styles.

2.3 Ideal Lumped Element Coupler Performance

The distributed 3-dB branch-line and the 3-dB rat-race couplers were the starting point for the design of the microstructure couplers presented in this thesis. The distributed couplers were converted to their lumped element equivalent circuits by replacing each transmission line in the coupler with its ideal lumped element equivalent. The definition of ideal lumped element in this case is that the lumped elements were direct replacements for the transmission lines at the centre frequency, and the lumped elements had ideal performance, meaning that they were purely inductive or capacitive and did not introduce any loss into the circuit.

Using even and odd mode analysis similar to [6], the S parameter equations of the lumped element branch-line and rat-race couplers were derived. These equations are provided in Appendix B due to their length. Plots of the derived S-parameter equations vs. frequency in Figure 2.14 and Figure 2.15 show the ideal performance of the lumped element branch-line and rat-race couplers. The phase difference plots (from the phase of the derived S-parameter equations) of lumped element branch-line and rate race couplers are shown in Figure 2.16 to Figure 2.18.

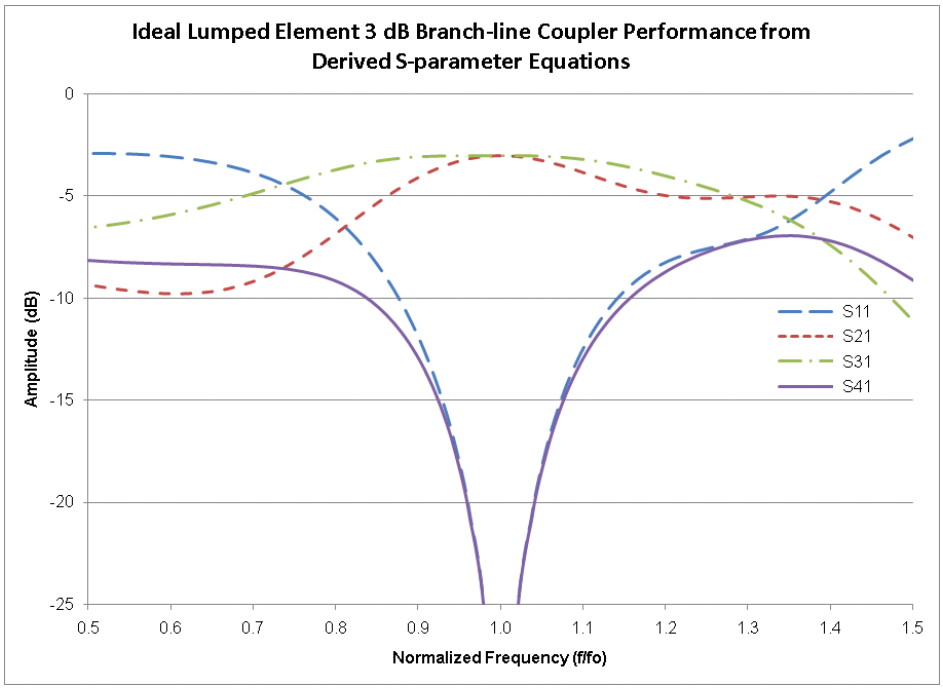

Figure 2.14: Performance of an Ideal Lumped Element Branch-Line Coupler from Derived S-Parameter Equations

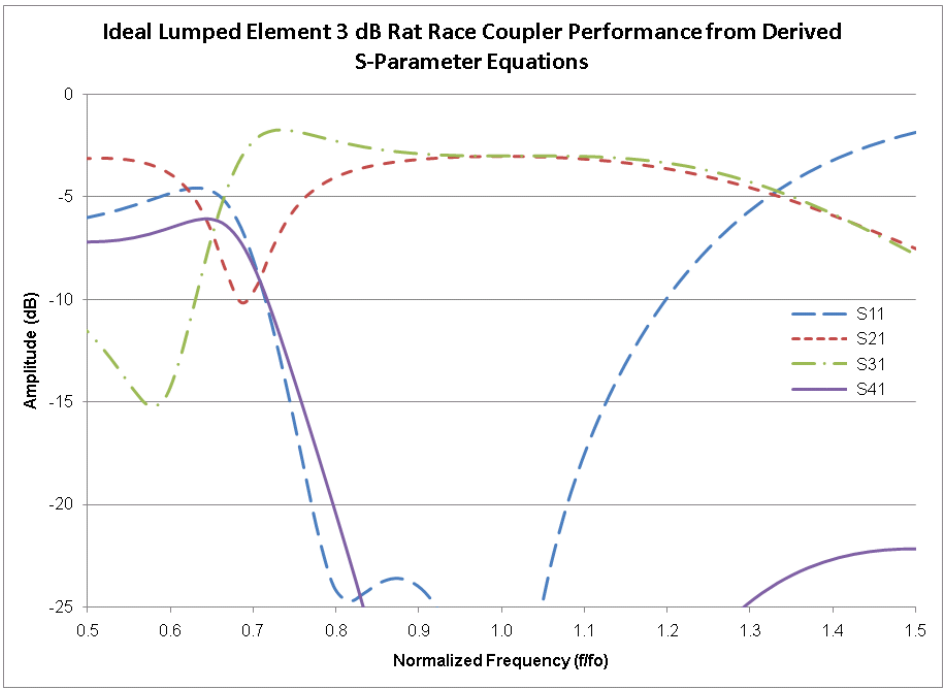

Figure 2.15: Performance of an Ideal Lumped Element Rat-Race Coupler from Derived S-Parameter Equations

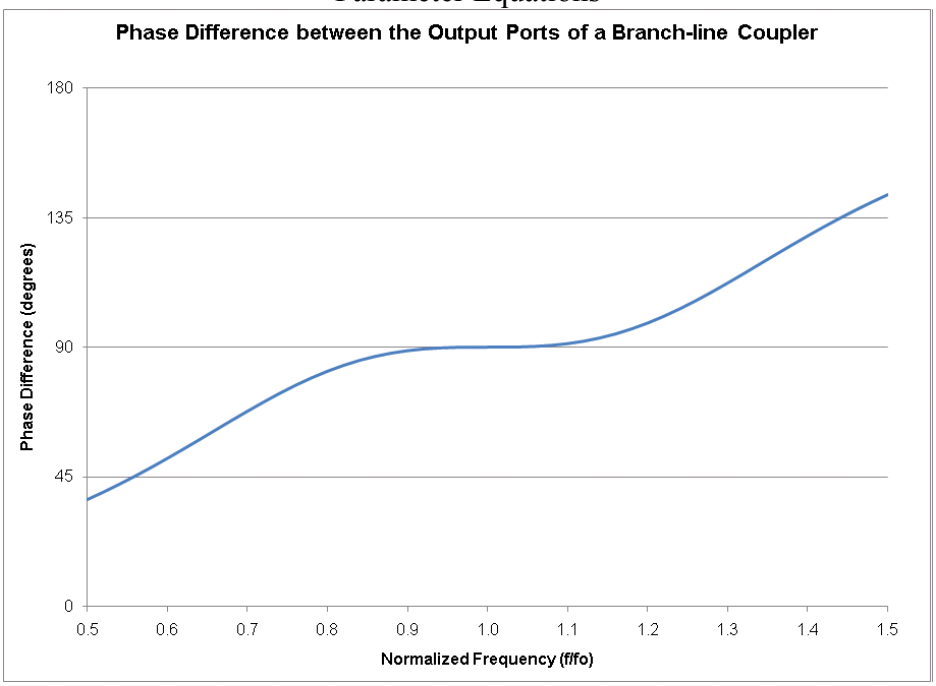

Figure 2.16: Phase Difference between the Outputs of an Ideal Lumped Element Branch-line Coupler from Derived S-Parameter Equations

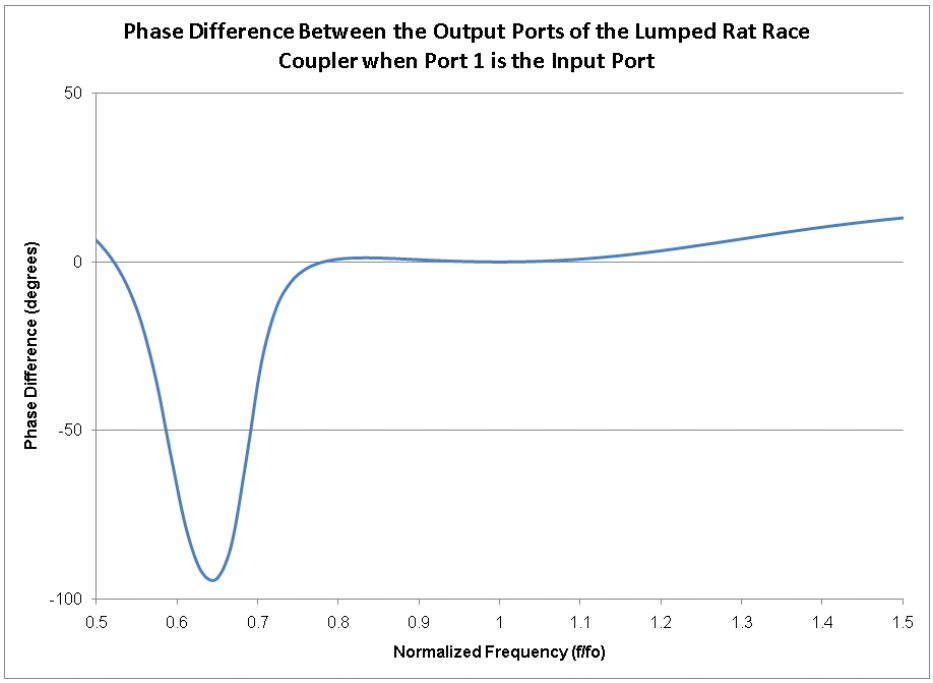

Figure 2.17: Phase Difference between the Outputs of an Ideal Lumped Element Rat-Race Coupler when Port 1 is the Input Port

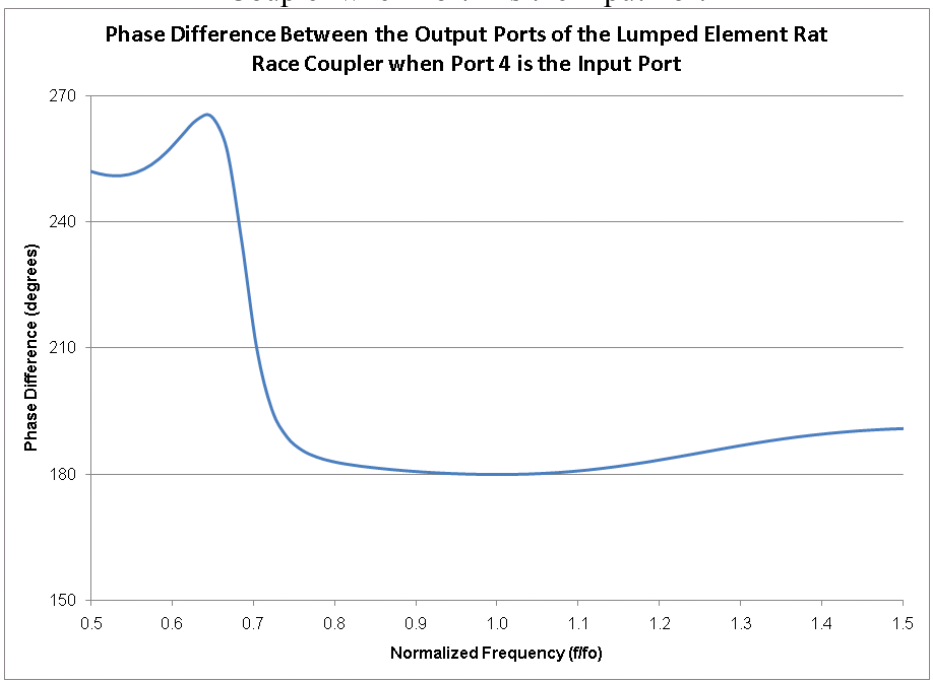

Figure 2.18: Phase Difference between the Outputs of an Ideal Lumped Element Rat-Race Coupler when Port 4 is the Input Port

The performance of the branch-line and rat-race couplers are similar because they both achieve 3-dB coupling at the centre frequency and have excellent return loss and isolation.

The difference in performance is that the rat-race coupler has larger 3-dB bandwidths of 56.5% (lumped rat-race 0°) and 66.5% (lumped rat-race 180°) vs 51.7% for the lumped branch-line, and larger ±5° phase bandwidths of 50.6% (lumped rat-race 0°) and 47.8% (lumped rat-race 180°) vs. 26.3% for the lumped branch-line. The 15 dB isolation bandwidth of the rat-race couplers could not be quantified because $|S_{41}|$ is better than -15 dB for frequencies higher than f_0.

In Section 2.4 the performance of the distributed branch-line and rat-race couplers are compared to their lumped element equivalent. Agilent's Advanced Design System (ADS) software [19] is used to perform the network analysis to determine the S-parameters of the different coupler styles since it is more convenient than determining the S-parameter equations each time a lumped element value is changed.

2.4 Distributed and Lumped Element Simulation Results

The two microstructure couplers designed for this thesis were based on the 3-dB branch-line coupler and the 3-dB rat-race coupler. The general S-parameter equations for the lumped and distributed couplers as a function of frequency are complicated, and are given in Appendices A and B. At the centre frequency, the S-parameter matrices of the distributed and lumped element couplers are equal and are shown below for the branch-line and rat-race couplers.

$$\left[S_{branch-line\_at\_f_0}\right] = \frac{-1}{\sqrt{2}}\begin{bmatrix} 0 & j & 1 & 0 \\ j & 0 & 0 & 1 \\ 1 & 0 & 0 & j \\ 0 & 1 & j & 0 \end{bmatrix} \tag{2.37}$$

$$\left[S_{rat-race\_at\_f_0}\right] = \frac{-1}{\sqrt{2}}\begin{bmatrix} 0 & j & j & 0 \\ j & 0 & 0 & -j \\ j & 0 & 0 & j \\ 0 & -j & j & 0 \end{bmatrix} \tag{2.38}$$

The distributed and lumped element simulation results are separated into two sections based on the coupler type. Agilent's ADS was the simulation software used. ADS is an electronic design automation (EDA) software for RF, microwave, and high speed digital

design and verification [20]. ADS is a very powerful tool that can perform a variety of different simulations. The main components of ADS used in this research are the linear circuit simulator for S-parameter simulations and the statistical design module for optimizations. For the simulations ideal lumped elements and ideal transmission lines were used.

2.4.1 Distributed and Lumped Element 3-dB Branch-Line Coupler Simulation Results

The first step in the development of the microstructure branch-line coupler was comparing the performance (3-dB, isolation, and phase bandwidths as previously defined in this chapter) of the ideal distributed version of this coupler to the ideal lumped element version. The lumped element and distributed branch-line couplers were implemented with ADS's ideal lumped elements and ideal $\frac{\lambda}{4}$ transmission lines. The ADS coupler schematics for a 5.4 GHz design are provided in Figures 2.19 and 2.20. The simulation results of the S-parameters for the ideal distributed and lumped element branch-line couplers are shown in Figure 2.21 and Figure 2.22, and the phase performance is shown in Figure 2.23.

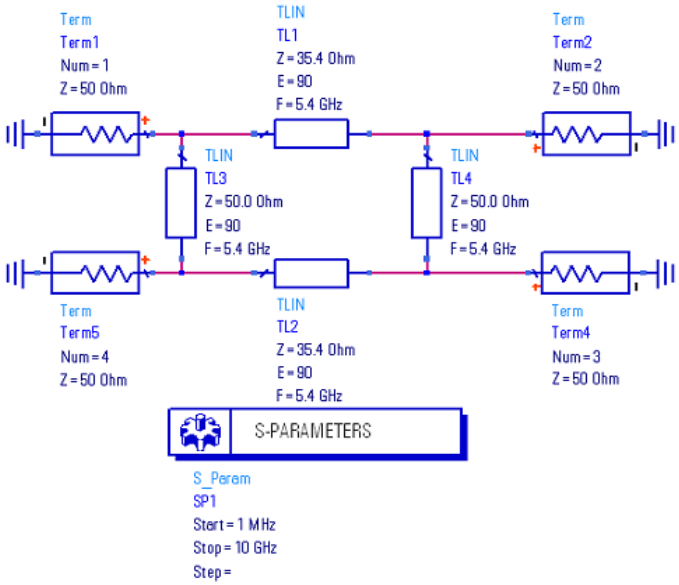

Figure 2.19: ADS Schematic of the Ideal Distributed Branch-line Coupler

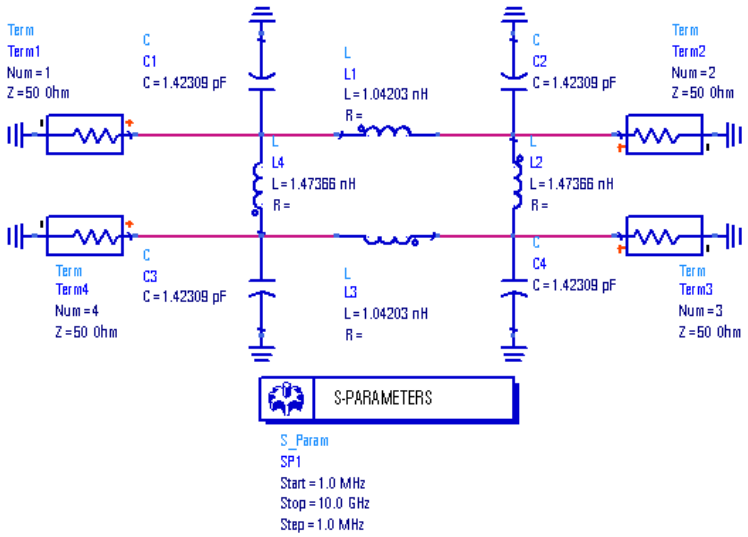

Figure 2.20: ADS Schematic of the Ideal Lumped Element Branch-line Coupler

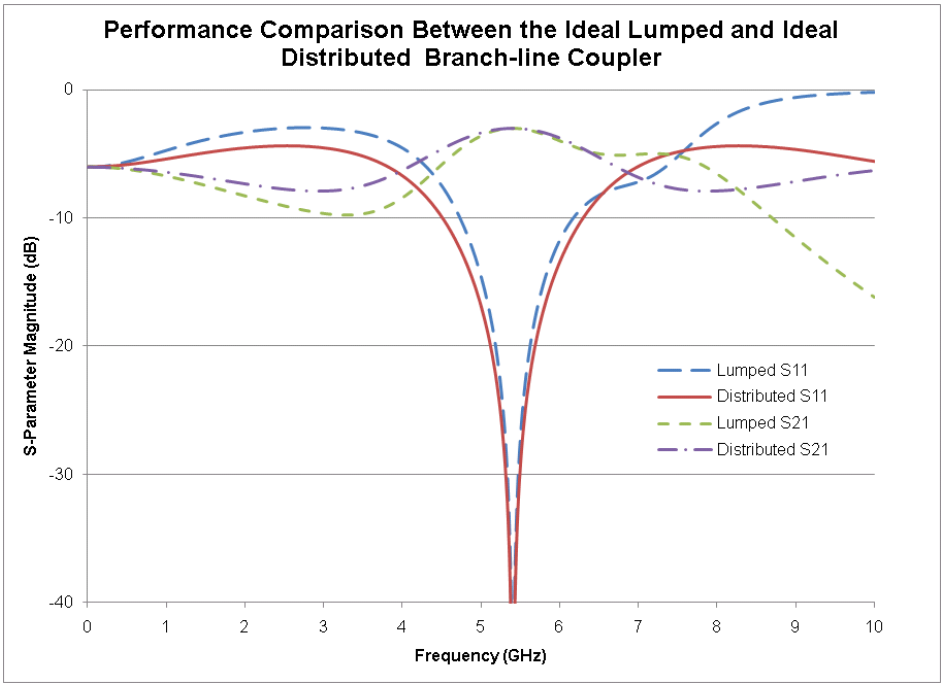

Figure 2.21: $|S_{11}|$ and $|S_{21}|$ Performance Comparison Between the Ideal Lumped Element and the Ideal Distributed Branch-Line Couplers

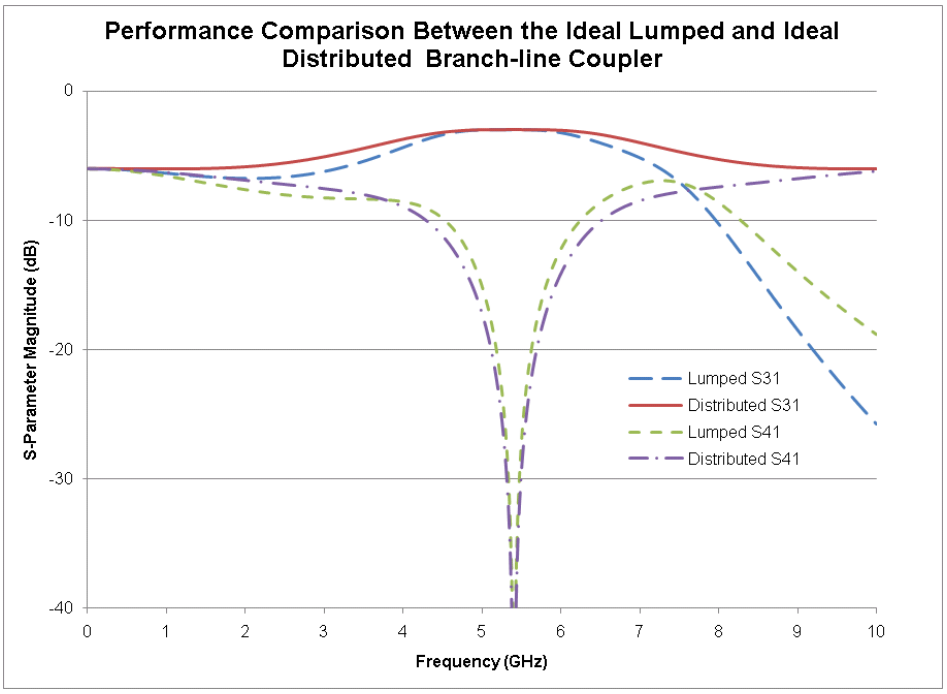

Figure 2.22: $|S_{31}|$ and $|S_{41}|$ Performance Comparison Between the Ideal Lumped Element and the Ideal Distributed Branch-Line Couplers

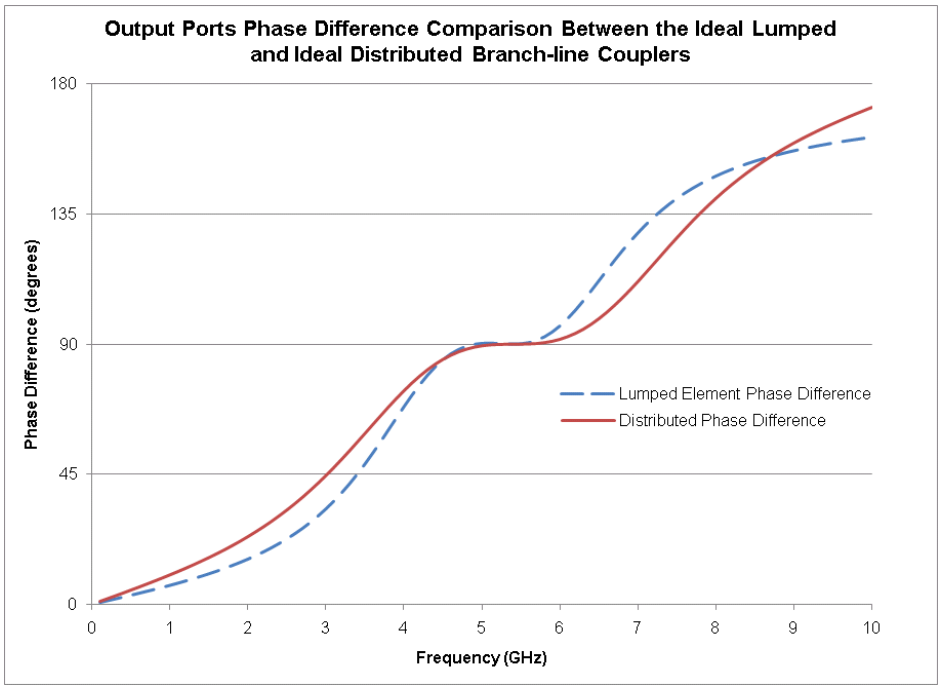

Figure 2.23: Output Ports Phase Difference Comparison Between the Ideal Lumped Element and the Ideal Distributed Branch-line Couplers

The ideal distributed and ideal lumped element couplers were simulated using ADS with ideal transmission lines and ideal lumped elements for an operating frequency of 5.4 GHz. The simulation results of the coupler comparison in Figure 2.21 and Figure 2.22 show that at 5.4 GHz, both coupler styles have the appropriate amplitude characteristics ($|S_{21}|$, $|S_{31}|$) of 3 dB power division between the output ports, while the isolation ($|S_{41}|$) and return loss ($|S_{11}|$) are greater than 15 dB over approximately 800 MHz. The coupled (S_{31}) and through (S_{21}) signals of both coupler styles are 90º out of phase at 5.4 GHz. Table 2.2 provides a summary of comparison between both coupler styles and shows that the performance is similar, however the ideal lumped element coupler has a wider 3-dB bandwidth than the ideal distributed coupler.

The difference between the two styles of couplers occurs at higher frequencies (greater than 8 GHz) due to the λ/4 electrical length of each transmission line in the distributed model, which results in re-entrant coupling behaviour. Another reason for the difference in performance is the ideal lumped element coupler was implemented with low pass π model lumped element circuits, which cause the signals at the output ports of the coupler to decrease at high frequencies, similar to the behavior of a low pass filter.

Table 2.2: Distributed and Lumped Element Branch-Line Coupler Performance Comparison

5.4 GHz Branch-Line Coupler Comparison						
Type	3-dB % BW	$\|S_{21}\|$ at 5.4 GHz (dB)	$\|S_{31}\|$ at 5.4 GHz (dB)	Phase difference between Port 2 and Port 3 at 5.4 GHz	Isolation BW %	Phase BW %
Ideal Lumped	51.7	-3.01	-3.01	90.0°	15.2	26.3
Ideal Distributed	49.2	-3.02	-3.00	90.0°	19.7	32.8
Optimized Lumped	54.2	-3.10	-3.01	89.9°	15.8	26.1

Since the simulation results prove that the lumped element coupler performance is comparable to the performance of the distributed coupler, the lumped element coupler components (inductors and capacitors) were optimized to try increase the 3-dB percent bandwidth of the lumped element coupler.

Optimization of the inductor and capacitor values were performed using ADS with lossless inductors and capacitors. The gradient optimization method was chosen. Random

and gradient optimizations are amongst the most popular optimizations methods used in ADS because they are suitable for most types of circuits [21]. The gradient optimizer was chosen over the random optimizer because only slight variations in the circuit component values were desired since the calculated values were known to provide suitable performance. Also, since the random optimizer uses a pseudo-random generator to determine the next variable value, different results can occur for optimization of the same circuit, where as with the gradient optimizer the next variable value is determined by the gradient of the network's error function (the gradient of the error function indicates the direction to move a set of parameter values in order to reduce the error function)[21], and since only slight changes are made to the variable at a time, running a gradient optimization on two of the same circuits, should yield the same results.

Four goals were set up for the optimization to try maximize the 3-dB bandwidth while at the same time not sacrificing any of the isolation $|S_{41}|$ bandwidth. The goals were to hold $|S_{21}|$ and $|S_{31}|$ between -3.01 dB and -3.50 dB over the frequency range 3.95 GHz to 8.10 GHz, and for $|S_{11}|$ and $|S_{41}|$ to have a maximum value of -20 dB over the frequency range 5.3 GHz to 5.5 GHz. All goals were weighted with equal value.

The largest increase in the 3-dB bandwidth occurred when the value of C_T (Figure 2.12 (b)) was decreased from 1.420 pF to 1.341 pF. Changing C_T to its optimized value while keeping the inductors at the original values of 1.042 nH and 1.474 nH, resulted in an increase in 3-dB percent bandwidth from 51.7% to 54.1%. In addition to increasing the 3-dB bandwidth of the coupler, the phase and isolation percent bandwidths, as well as the power division between the output ports of the optimized lumped coupler remained comparable to the results of the ideal lumped element coupler. The optimized lumped element coupler is used as the model for the design of the 3-dB branch-line microstructure coupler since its simulated performance, as a function of frequency, is better than the lumped element coupler with the ideal lumped element calculated values that matched the distributed coupler at the centre frequency. Table 2.2 summarizes the performance of the optimized lumped element coupler.

2.4.2 Distributed and Lumped Element 3-dB Rat-Race Coupler Simulation Results

The procedure for the design of the rat-race coupler has the same steps as the design of the branch-line coupler. The first step was to determine if the distributed and lumped element rat-race couplers had similar performance. Both coupler styles were simulated using ADS with ideal transmission lines and ideal lumped elements. The simulation results of the S-parameters and the phase performance is shown in Figure 2.24 through Figure 2.27.

Table 2.3 displays the relevant values and bandwidths obtained from simulations to compare the different styles of couplers. The simulation results revealed that both couplers had the appropriate output power division and a phase difference between output ports of 180°. The advantage of the ideal lumped element model is that it had a 32% wider ±5° phase bandwidth than the distributed model and also had a 10% larger 3-dB bandwidth. The return loss bandwidth was also determined to compare the two couplers. The return loss bandwidth is a measure of the frequency band that occurs between the two points of $|S_{11}|$ that were less than -9.54 dB. The lumped element model had a 6% smaller return loss bandwidth than the distributed model. Isolation bandwidth was not used as a comparison for the rat-race couplers because at frequencies higher than 5.4 GHz the isolation continues to stay below -15 dB. Since the simulation results show that the lumped element rat-race coupler has very similar, if not better performance than the distributed rat-race model, the lumped element coupler components (inductors and capacitors) were optimized, using gradient optimization with similar goals as in the previous section, to try to increase the 3-dB bandwidth of the rat-race lumped model.

The best results found through optimization occurred when four of the six capacitors in Figure 2.13 (b) were changed. Referring to Figure 2.13 (b), when the capacitors connected to ground that are labeled C_b are decreased from 0.417 pF to 0.168 pF, and the capacitors labeled C_c are increased from 0.417 pF to 0.566 pF the 3-dB bandwidth of the rat-race lumped model coupler is increased by approximately 20% and the phase and return loss bandwidths are both increased by approximately 10%. The values of the inductors and capacitors labeled C_a used in the optimized model remained the same as in the ideal lumped element rat-race model at 2.084 nH and 0.417 pF. The inductors and capacitors used in the optimization model were ideal lossless lumped elements.

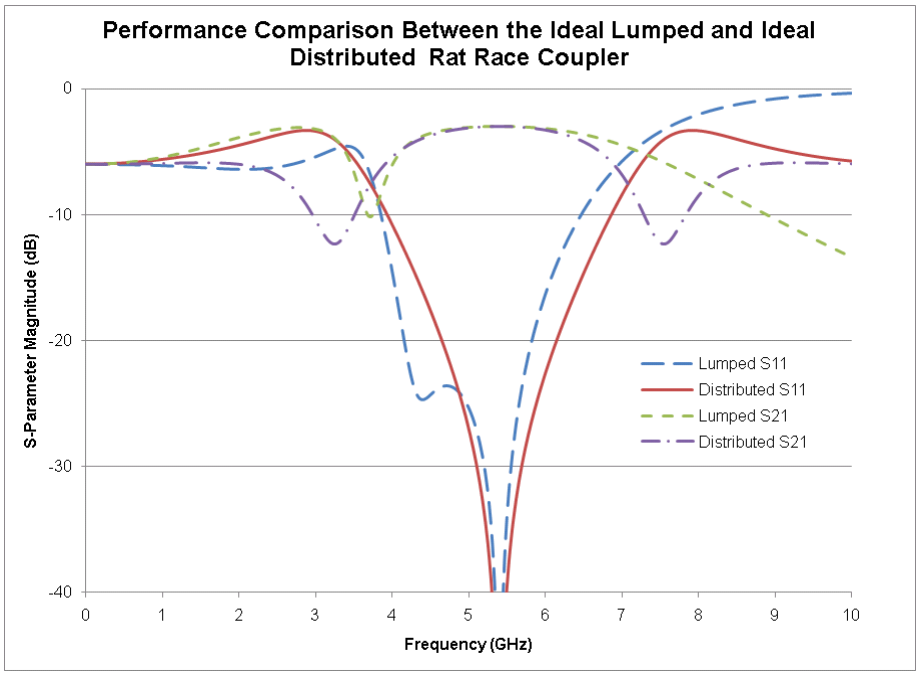

Figure 2.24: $|S_{11}|$ and $|S_{21}|$ Performance Comparison Between the Ideal Lumped Element and the Ideal Distributed Rat-Race Couplers

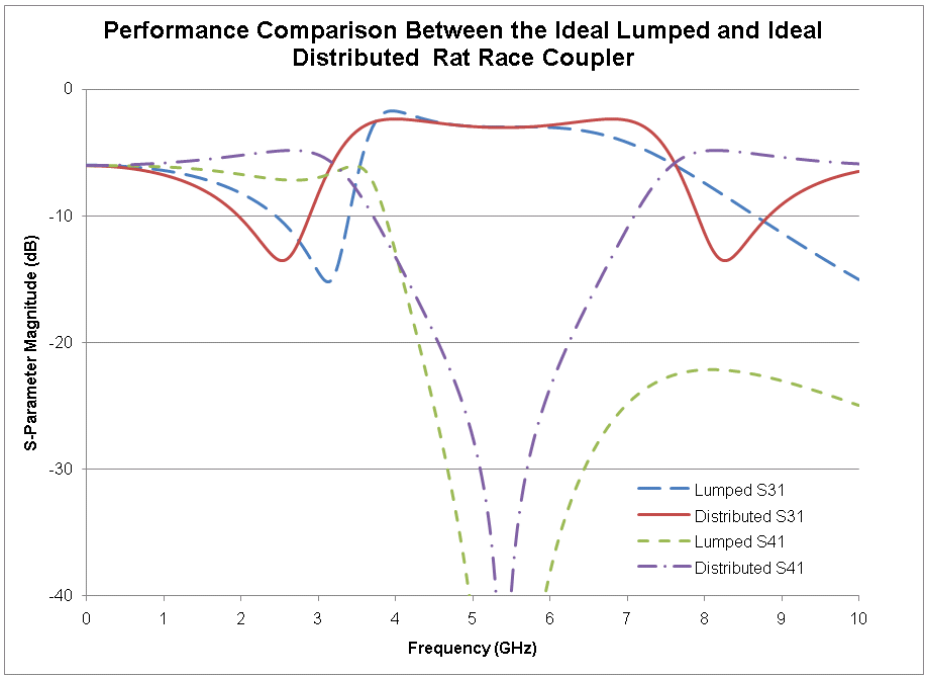

Figure 2.25: $|S_{11}|$ and $|S_{21}|$ Performance Comparison Between the Ideal Lumped Element and the Ideal Distributed Rat-Race Couplers

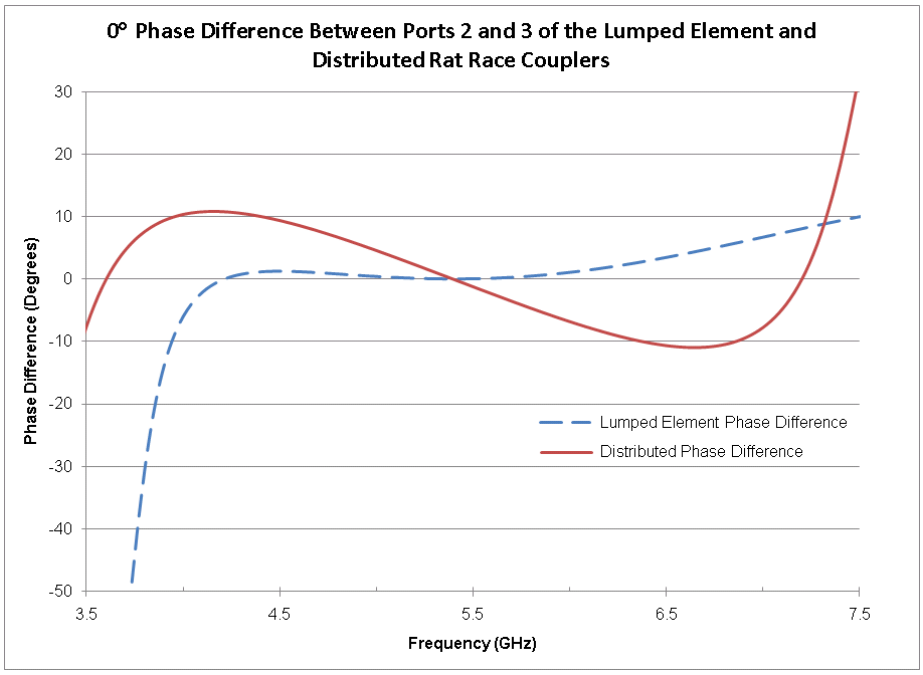

Figure 2.26: Phase Difference Between Ports 2 and 3 of the Ideal Lumped Element and the Ideal Distributed Rat-Race Couplers when Port 1 is the Input Port

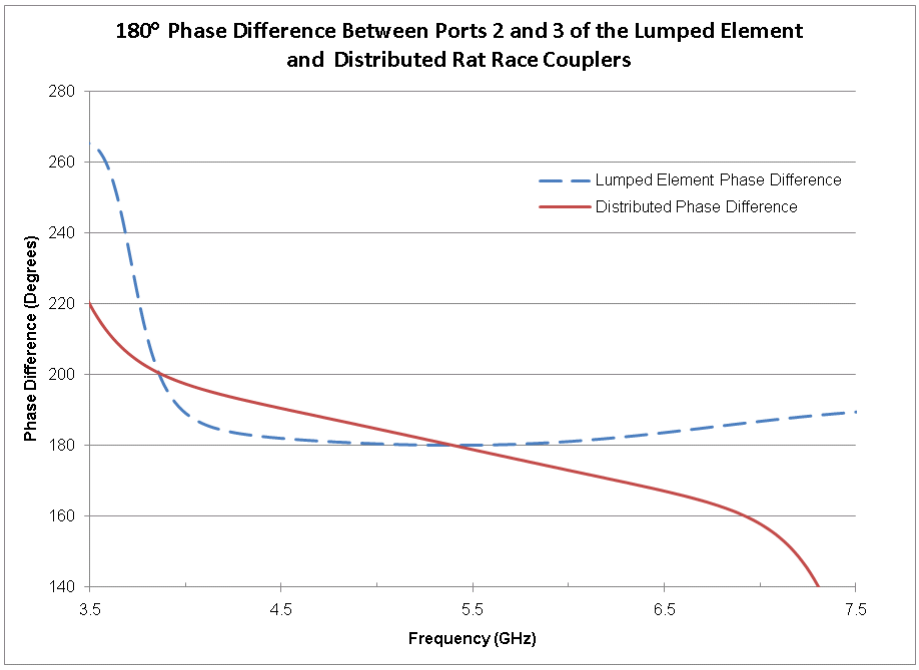

Figure 2.27: Phase Difference Between Ports 2 and 3 of the Ideal Lumped Element and the Ideal Distributed Rat-Race Couplers when Port 1 is the Input Port

Table 2.3 also provides a comparison of the optimized lumped element rat-race coupler to the ideal lumped element and ideal distributed rat-race models. Since the optimized model

had even better performance than the lumped element model, it was chosen as the starting point for the structural design of the microstructure rat-race coupler.

Table 2.3: Distributed and Lumped Element 180° Rat-Race Coupler Performance Comparison

5.4 GHz 180° Rat-Race Coupler Comparison						
Type	3-dB BW (%)	$\|S_{21}\|$ at 5.4 GHz (dB)	$\|S_{31}\|$ at 5.4 GHz (dB)	Phase difference between Port 2 and Port 3 at 5.4 GHz	Return Loss BW (%)	180° Case Phase BW (%)
Ideal Distributed	55.3	-3.01	-3.01	180.0°	55.8	15.8
Ideal Lumped	66.5	-3.01	-3.01	180.0°	49.6	47.7
Optimized Lumped	88.1	-3.05	-3.06	179.0°	59.2	57.8

CHAPTER 3
LUMPED ELEMENT MICROSTRUCTURES AND SIMULATED MICROSTRUCTURE COUPLER DESIGNS

This chapter presents the background information on microstructure capacitors and inductors, as well as the structural design and simulation results of the microstructure branch-line and rat-race couplers.

3.1 Capacitors

High aspect ratio variable capacitors were designed and fabricated in [7], [22], [23]. The advantage of these capacitors is that their capacitance plates are oriented vertically, instead of horizontally, taking up less area on the substrate and less lateral electrical size. Both simulation and test results show that the capacitors have high Q in the 1-12 GHz range. The quality (Q) factor indicates the amount of loss that the lumped element will introduce into the circuit. The Q factor is calculated by:

$$Q = \frac{imaginary(Z_{lumped})}{real(Z_{lumped})}, \tag{3.1}$$

where Z_{lumped} is the impedance of the lumped element.

The high aspect ratio capacitors can be made tunable by implementing a released cantilever that changes position as a function of voltage applied to the actuator port. This feature was not used in the current thesis, but could be important in the design of future tunable lumped element circuits. Additionally, the value of capacitance can be controlled not only by the gap size, but also by the structures height, without requiring extra substrate area.

The capacitor shown in Figure 3.1 from [8] was fabricated with the deep XRL and showed high Q of 21 to 400 in the 1 to 5 GHz frequency range. The tuning range of the capacitors was 1.24:1 with the capacitance varying from 0.68 pF to 0.84 pF at the operating frequency of 4 GHz, depending on the actuator voltage. The gap size of the capacitor was fabricated to be 2.5 μm with a height of 100 μm, providing an aspect ratio of 40:1.

The metal used in electroplating of the capacitance structure was nickel. Nickel was chosen because it electroplates evenly to produce good structure quality.

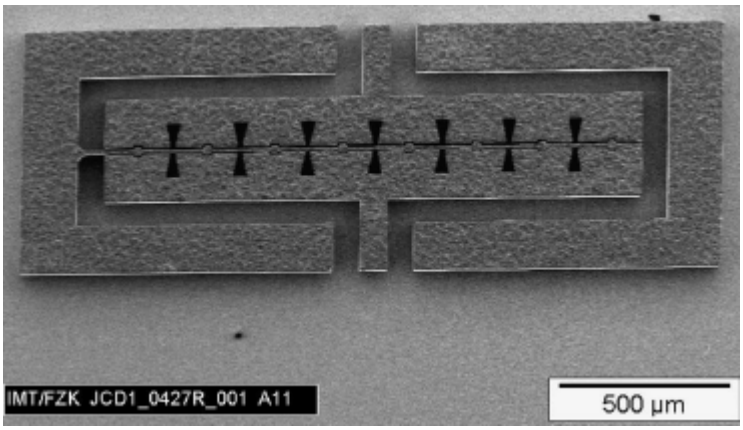

Figure 3.1: Top view of the high aspect ratio variable capacitor [8]

3.2 Inductors

High aspect ratio inductors with high Q factors have been demonstrated in [9]. These inductors were fabricated using D-XRL. The advantage of these inductors over planar spiral inductors is that they do not require bonding wires for a centre connection, which introduce extra loss into the circuitry, they are made of thick metal and have low loss, and they are structurally compatible with the tall capacitor structures.

The design of the inductors in [9] is different from [10], [24], because the coils of the inductor are touching the substrate. The inductors in this design are single loop and are 70 µm in height. Since these inductors are not suspended in air they only require a single mask and exposure for fabrication.

The main contributor to the inductance value of the structure is the self inductance caused by the length of metal used to implement the loop. Since there are not multiple loops there is no positive mutual inductance created in the structure. The opposite sides of the loop cause the structure to have a small negative mutual inductance since the current is flowing in opposite directions.

The single loop inductors were fabricated in nickel and gold on alumina and quartz glass substrate. Due to the higher conductivity of gold compared to nickel, the inductors fabricated in gold achieved a higher Q than their nickel equivalent because there was less loss caused by the metal. Another interesting point from [9] is that the inductors on quartz glass substrate

had a slightly higher Q and a higher self resonant frequency than equivalent inductors on alumina substrate. The self resonant frequency of a lumped element is the frequency which the lumped element has equal inductive and capacitive imaginary impedance. At frequencies greater than the self resonant frequency an inductor will behave a capacitor. The reason for the higher Q and higher SRF is because the quartz glass substrate has a lower dielectric constant, making the inductors electrically smaller than on alumina. A SEM image of a fabricated nickel inductor on alumina substrate is shown in Figure 3.2.

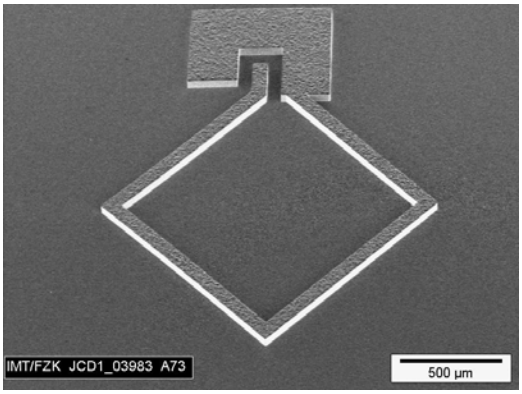

Figure 3.2: Inclined view of the 1-loop inductor from [9]

The test results of a fabricated single loop nickel inductor on quartz glass substrate show inductance of 2.5 nH and Q factor of about 20 at 4 GHz.

The D-XRL fabricated high aspect ratio capacitor and inductor features have been applied to the design of third order Chebychev lowpass filters [25], [26]. The microstructure filter design was derived from the lumped element ladder network of the low pass filter. A similar approach is taken in this thesis to extend high Q capacitor and inductor elements to lumped element coupler circuits.

3.3 Lumped Element Microstructures for the Microstructure Coupler Design

3.3.1 Structural Simulation Software

The 3-D microstructure simulations were performed using Ansoft's HFSS [27]. HFSS stands for High Frequency Structure Simulator. It uses a finite element method (FEM) for electromagnetic (EM) simulation [28]. During a simulation, HFSS divides the 3-D structure into a mesh of many tetrahedrons, and solves the EM fields at each node of a tetrahedron and then calculates the S-parameter matrix of the structure from the resulting Maxwell's equations using a numerical method.

For a simulation, a minimum of two meshes are created for the structure (the second one being finer and having more tetrahedra) to determine if the solution is accurate by monitoring the difference between the S-parameter matrices from both sets of meshes. Each time a new mesh is created it is called a pass. The maximum number of passes is set by the user in the simulation set up. The mesh is made finer during each pass for the areas of the structure that have the largest change in S-parameters. An additional new mesh is created if the difference between the S-parameters matrices from the current and previous mesh exceeds the pre-defined delta-S value (delta-S is 0.02 by default but can be set by the user) and if the maximum number of passes has not been reached. Delta-S is defined as the maximum change in the magnitude of the S-parameter matrices between two consecutive passes [28]. From [28], the values of delta-S that are generally sufficient to obtain accurate simulation results are 0.01 to 0.02. Decreasing the value of delta-S below 0.01 to increase simulation accuracy will result in a longer simulation time. When the difference between the S-parameter matrices from the current and previous meshes are less than or equal to delta-S the meshing solution has converged, and the mesh can be used to calculate the S-parameters for the structure at each frequency specified in the simulation frequency span. If the maximum number of passes occurs before convergence the S-parameters for the structure will be calculated with the last mesh, but the results will have errors since the mesh for the structure is not fine enough.

In addition to the 3-D structure under simulation and the substrate, HFSS simulations require the use of virtual objects such as an air box, lumped or wave ports, and perfect electric conductor (perfect E) boundaries. The air box is required to separate the entire structure from the background since HFSS automatically assigns all surfaces touching the background as a perfect E boundary. The air box must be large enough that the structures fields do not interfere with walls of the air box. Lumped ports and wave ports permit excitation signals to enter and leave the structure. Wave ports are best suited for simulations when excitation by a semi-infinite waveguide is required, where lumped ports simulate the results obtained from Ground-Signal-Ground ports well. Since the planned approach for testing the fabricated microstructure couplers is to use Ground-Signal-Ground probes, lumped ports and the required perfect E boundaries were used in the simulations. For simulations the impedance of each lumped port was assigned to 50Ω.

Each microstructure element was designed to be fabricated with a single metal layer with no additional jumper wires or interconnects. A single metal layer design is desired so that only one mask is needed for fabrication of the device. The metal chosen for simulation and fabrication is nickel since it is has been used before to make high quality microstructures and it is readily available for the microelectroplating processes. The substrates chosen for simulations are quartz glass and alumina. The detailed material properties of the simulated nickel, quartz glass, and alumina ceramic are provided in Table 3.1. The conductivity and relative permeability of nickel used in simulation are different from the HFSS default values since it has been shown in [29] and [30] that these properties in electroplated nickel vary with frequency, and the default values provided are for bulk nickel and do not take the frequency effect into account.

Although the inductor and capacitor elements simulated with HFSS are considered lumped, the electrical size of the structure will be minimally affected by the substrate, since the structures do have a size which will make them behave slightly distributed. It is expected that the structures on quartz glass with have better performance than the structures on alumina since the relative permittivity of quartz glass is lower, making the structure smaller in electrical size.

Table 3.1: Material Properties used in HFSS Simulation

Material Property	**Values**
1. Conductivity of Nickel, σ	1.266×10^{7} Siemens/m
2. Relative Permeability of Nickel, μ_r	3
3. Relative Permittivity of Quartz Glass Substrate, ε_r	3.78
4. Relative Permittivity of Alumina Ceramic Substrate, ε_r	9.4, and 9.8
5. Thickness of Substrate, t_s	1 mm, 0.5 mm
6. Thickness of Nickel, t_{ni}	220 µm, 110 µm

The next sections provide the simulation results for the microstructure capacitors and inductors used in the designs of the microstructure couplers.

3.3.2 Capacitor Design and Simulated Performance

The designs of the high aspect ratio microstructure capacitors are based on the capacitors in [22], but are static instead of tunable. Each microstructure capacitor consists of two tall (220 μm) metal strips separated by a 6 μm or 8 μm air gap. To determine the approximate length of each metal strip, a simple parallel plate capacitance model, equation 3.2, was used as a starting point for simulation, then the length was adjusted until the required capacitance was achieved. Referring to equation 3.2, l is the metal length of the capacitor plate in meters (m), h is the metal height of the capacitor plate (m), C is the required capacitance in Farads (F), d is the gap size between the metal strips (m), and $\varepsilon_0 = 8.8542\times10^{-12}$ F/m is the permittivity of vacuum.

$$l = \frac{Cd}{h\varepsilon_0} \tag{3.2}$$

A number of microstructure capacitors were required for the designs of the microstructure branch-line coupler and the microstructure rat-race coupler. Each capacitor had a metal height of 220 μm, a gap size of 6 or 8 μm, and a quartz glass substrate. The high aspect ratio capacitors ranged in values from 0.165 pF to 1.284 pF (l = 210 μm to 2654 μm). The simulation results showed that at 5.4 GHz all of the capacitors had a high Q factor. The lowest Q factor achieved was 109 for the 1.284 pF capacitor at 5.4 GHz.

All of the simulated microstructure capacitors had a self resonant frequency (SRF) of greater than 15.7 GHz and were low loss. Typically the SRF should be greater than twice the operating frequency [22]. To illustrate that the simulated microstructure capacitors are almost purely reactive Figure 3.3 shows a Smith Chart plot of S_{11} from the simulated capacitor shown in Figure 3.4. The trace of S_{11} closely follows the outside ring of the Smith Chart, which is the purely reactive circle. The capacitance and Q factor are also labeled at various frequencies.

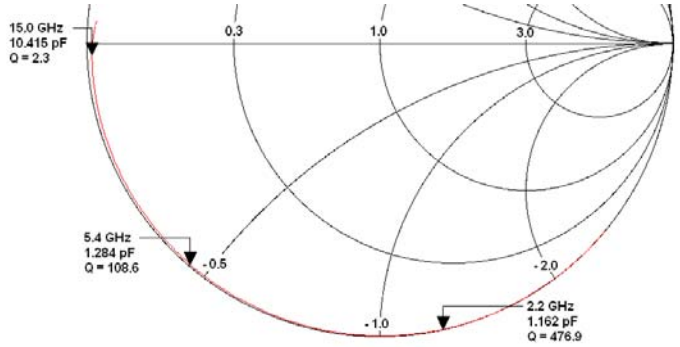

Figure 3.3: S_{11} of the 1.284 pF High Aspect Ratio Capacitors used in a Microstructure Coupler Design

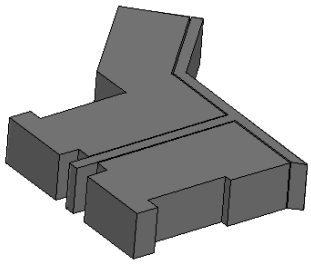

Figure 3.4: HFSS Capacitor Model of the 1.264 pF Capacitor

3.3.3 Inductor Design and Simulated Performance

The single and double loop inductors designed for the microstructure couplers are based on [9]. To calculate the approximate size of the loops the expanded Grover method [31] was used. The expanded Grover method is based on planar spiral inductors, but since the inductance value is more dependent on the length of the metal used, than the metal height, it is still a suitable method for approximating the loop size. The size of the loop was then adjusted in HFSS until the required inductance was achieved. The advantage of the single and double loop style of inductors is no air bridges or jumper wires were required since the structure does not contain a spiral coil. Each inductor was designed to be 220 μm in height with 50 μm wide lines, on a quartz glass substrate. Figure 3.5 (a) and (b) show the HFSS model of the single and double loop inductors surrounded by a ground ring. The ground ring was required for the single port simulation to ground the 2nd port of the inductor in order to obtain the structures inductance value. The ground rings added additional inductance to the devices since they are basically extra lengths of transmission lines. When the inductors are inserted into the microstructure coupler design the ground ring is removed.

The simulated performance of the single and double loop inductors showed that each of the inductors had a self resonant frequency of greater than 9.4 GHz, and the lowest Q factor of the inductors at 5.4 GHz was 27.3. Simulations using ADS were also performed to investigate the inductors Q value, and how it affects performance. A 3-dB lumped element coupler circuit was simulated with non-ideal lumped elements that allowed for the Q factor of all inductors and capacitors in the design to be changed manually. The results from the simulation showed that when the Q factors of the inductors were at 27, the performance of the coupler still had coupling of better than -4 dB, with return loss and isolation values of better than -20 dB at the centre frequency, which verified that the microstructure inductor was suitable to be used in the microstructure coupler design.

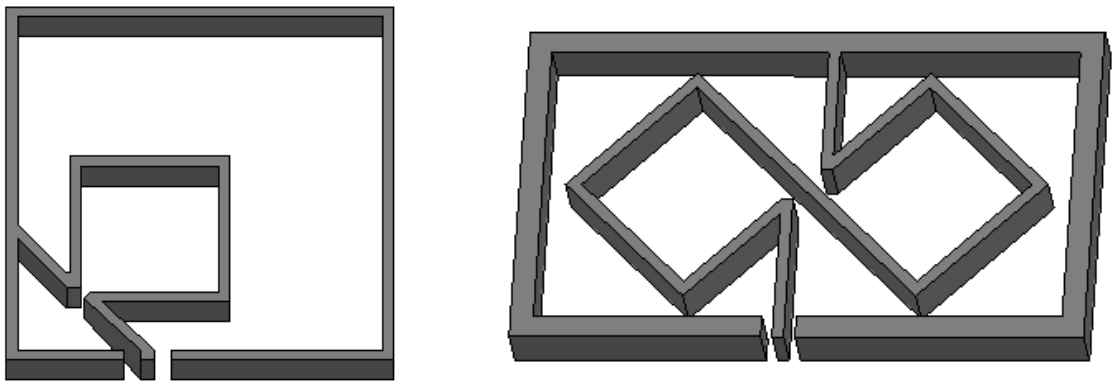

(a) (b)

Figure 3.5: HFSS Inductor Models. (a) Single Loop, (b) Double Loop

For the microstructure coupler designs the inductors ranged in value from 1.14 nH to 2.39 nH at 5.4 GHz. Figure 3.6 shows a Smith plot of S_{11} for the 2.39 nH (at 5.4 GHz) inductor simulation. The inductance and Q factors are labeled at various frequencies. The trace of S_{11} occurs in the upper region of the Smith plot indicating that the structure has inductive behavior, and since the trace follows the outer ring of the Smith Chart, it shows that the structure is low loss. The resistance in the inductor structures is higher than the capacitive structures probably due to being larger in size. The larger resistance is shown by the trace of S_{11} being further away from the outer ring of the Smith Chart. For the inductors

of smaller value, the Q factors were increased and the loss was decreased because these inductors were smaller in size, and therefore did not have as large of resistive losses.

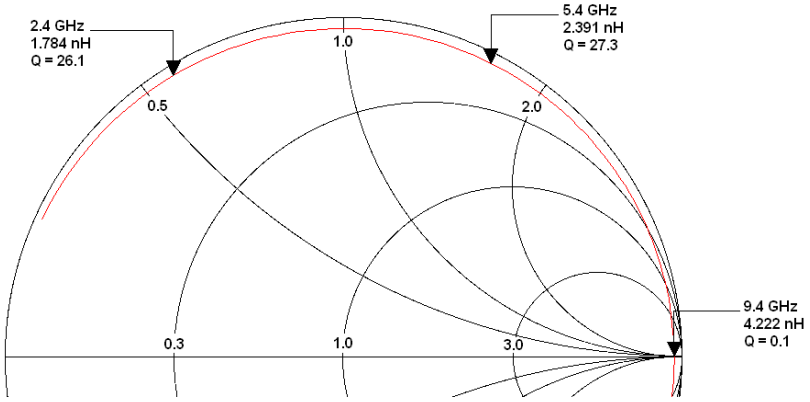

Figure 3.6: S_{11} of the 2.391 nH High Aspect Ratio Inductors used in a Microstructure Coupler Design

3.4 Microstructure Branch-Line Designs

The microstructure branch-line coupler designs are based on the schematic of the optimized lumped element branch-line coupler and the microstructure lumped elements explained in the previous two chapters. The microstructure lumped elements were simulated with a quartz glass substrate and have equivalent values to the inductor and capacitor values of the optimized lumped element branch-line coupler. To design the various microstructure branch-line couplers the microstructure lumped elements were arranged in a similar order to the optimized lumped element branch-line schematic, on a quartz glass substrate, and modified to improve the performance of the coupler.

Design A of the microstructure branch-line coupler had the dimensions of 3.87 mm by 4.59 mm with a height of 220 µm. The top view of this design is shown in Figure 3.7, along with the lumped element schematic. The thin dark grey lines represent signal lines, the light grey areas represent ground planes and the white areas are quartz glass substrate. The four single loop inductors are represented as the square structures near the middle and the four capacitors are formed by separating the signal lines and the ground plane by an 8 µm air gap.

Design A of the microstructure branch-line coupler proved to be considerably smaller (by approximately 72% area reduction) than the microstrip branch-line coupler (planar dimensions of 7.83 mm by 8.03 mm on quartz glass substrate), but still has unused area between the inductors. The large separation between the inductors was used to ensure that

the magnetic fields from the inductors did not interfere with one another. The field overlay function in HFSS was used to view the distance the magnetic fields radiated from the inductors and verified that the inductors could be moved closer together.

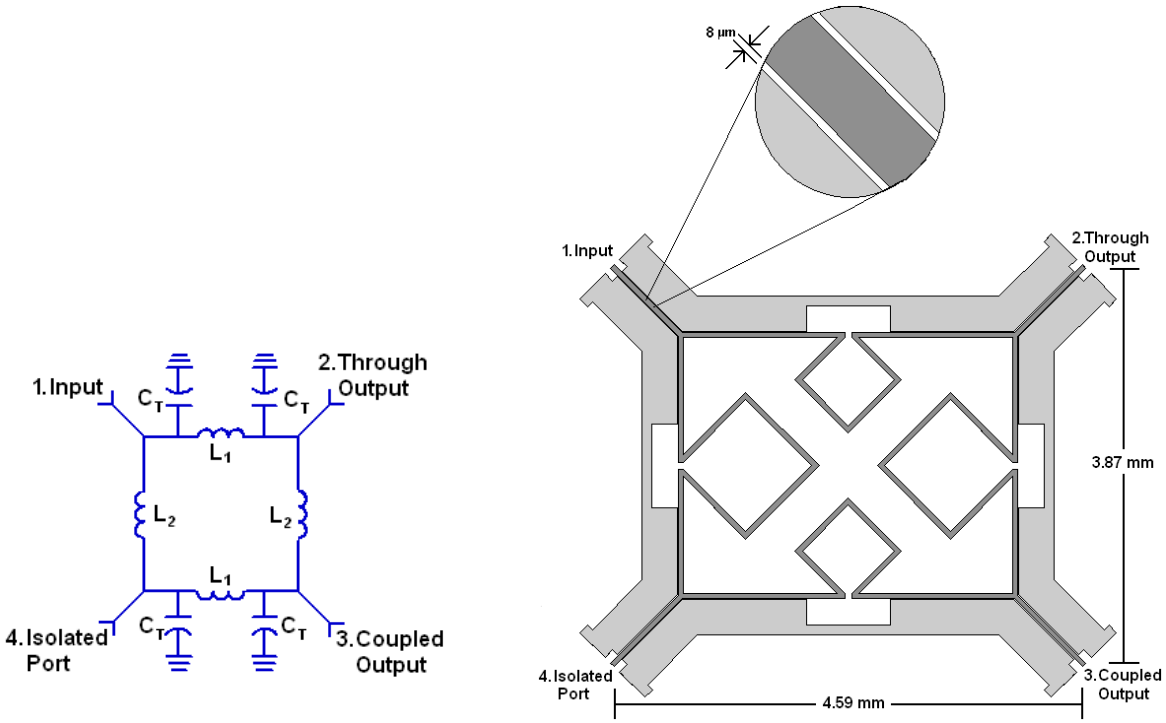

(a) (b)

Figure 3.7: Microstructure Coupler (a) Schematic (b) Design A Structure Top View

In addition to moving the inductors closer together, another way to decrease the area of the microstructure coupler was to decrease the size of the capacitors. To achieve smaller capacitors, the air gap was decreased from 8 µm to 6 µm, which increased the capacitance, and decreased the length of signal line and ground plane required for each capacitor. Figure 3.8 shows the top view and the 3-D view of Design B of the microstructure coupler. In Chapter 4, Design B will be referred to as the non-capacitance compensated coupler. Besides changing the distance between the inductors and the size of the capacitors this design also has 75 µm ports at the start of each signal line, instead of 50 µm ports, to improve testing capabilities of the fabricated design with a 150 µm pitch microprobe. The signal lines were also changed to split the signal in a T junction rather than a Y junction. This allowed for the signal line to be brought closer to the inductors and further reduce the coupler area. The

overall dimensions of Design B of the microstructure coupler are 2.73 mm by 3.44 mm with a height of 220 µm, representing an 85% area reduction over the classical distributed coupler.

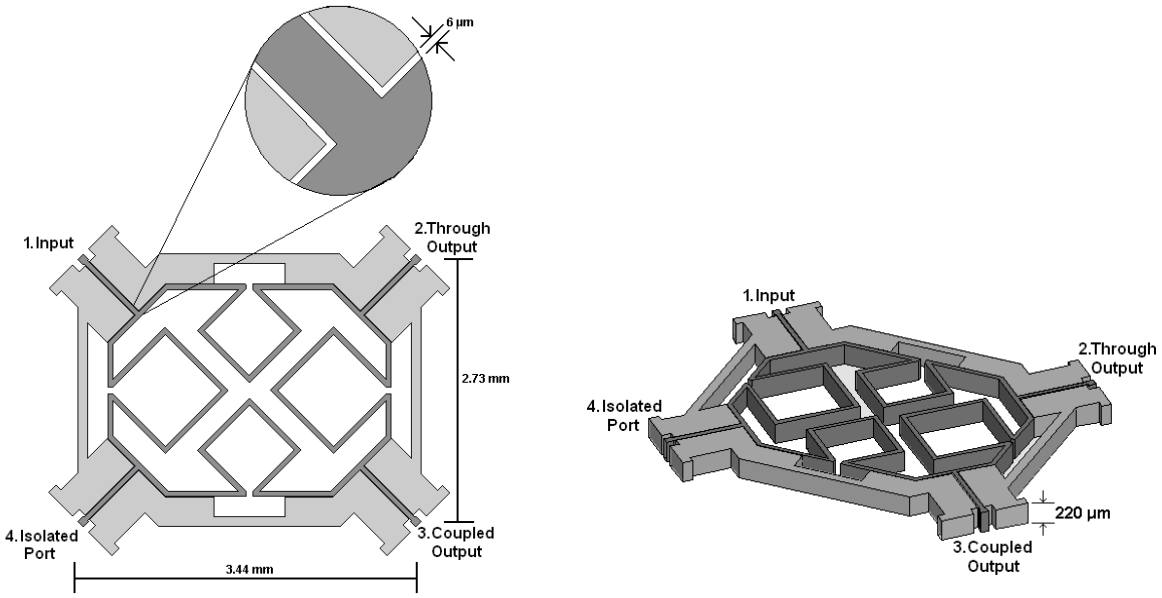

(a) (b)

Figure 3.8: Design B of the Microstructure Branch-Line Coupler (a) Top View (b) 3-D View

3.4.1 Additional Variations of the Microstructure Branch-Line Coupler Design

Two additional designs of the microstructure branch-line coupler were also completed and simulated. The first design is basically the same as the design in Figure 3.8, but with the inductors moved even closer together, further reducing the overall coupler area to 2.60 mm by 3.05 mm. The problem with this design is that the magnetic fields of the inductors did slightly interfere, and as a result the output signals of the coupler were slightly lossier than Design B. The simulation results of the reduced area coupler are provided in Table 3.2. The second additional design is a scaled down version of the branch-line coupler shown in Figure 3.8. Every component was scaled by 50% in the x, y, and z direction, making the signal lines 25 µm wide, the gap sizes 3 µm wide, and the height 110 µm. A problem that may occur with this design is that the smaller gap sizes may not be achievable for fabrication. The purpose of scaled design is to determine a relationship between scaling factor and coupler operating frequency.

3.5 Microstructure Branch-Line Simulation Results

HFSS was used to simulate the performance of the branch-line microstructure couplers shown in Figures 3.7 and 3.8, and the scaled version of the branch-line microstructure coupler. The results are shown in Figure 3.9 to Figure 3.15. The performance of the ideal optimized lumped element coupler is also shown in Figure 3.11 to Figure 3.13 to illustrate the similarities between the two coupler styles. The simulated results are discussed in Section 3.6.

3.5.1 Simulation Results of Design A of the Microstructure Branch-line Coupler

Figure 3.9 and Figure 3.10 show the ideal performance results of Design A of the microstructure branch-line coupler (shown in Figure 3.7) from 3.5 GHz to 7.5 GHz, on a quartz glass substrate with thickness of 1.0 mm, $\varepsilon_r = 3.78$, and $\tan \delta = 0$.

Figure 3.9 is a plot of the ideal reflection ($|S_{11}|$), isolation ($|S_{41}|$), through ($|S_{21}|$) and coupled ($|S_{31}|$) outputs of the large microstructure branch-line coupler. Figure 3.10 shows the ideal phase difference between the through (Port 2) and coupled (Port 3) outputs of Design A of the microstructure coupler.

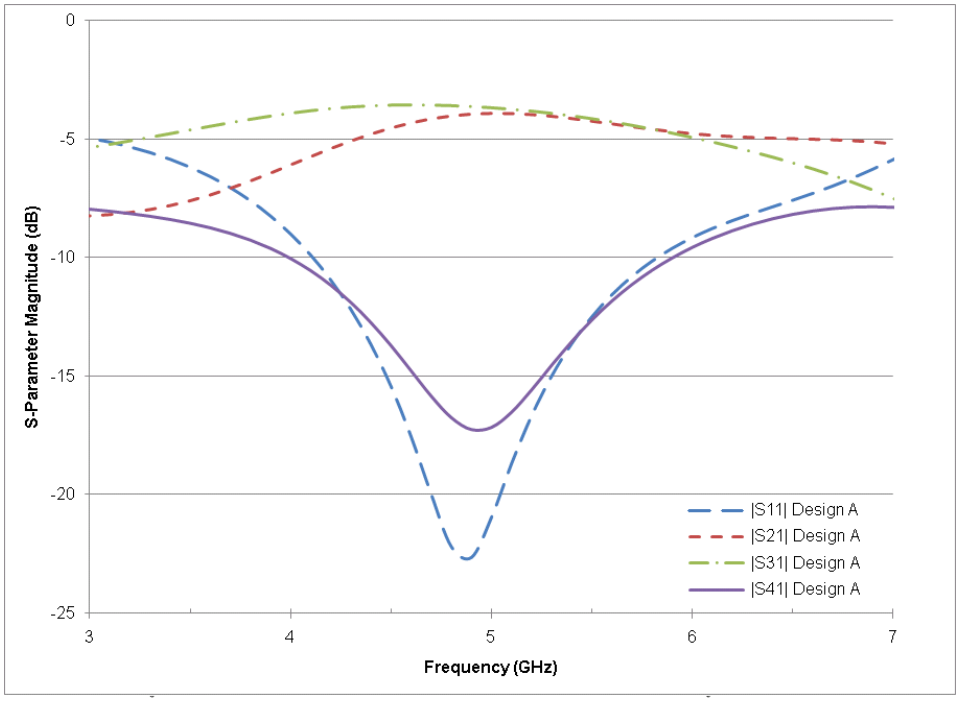

Figure 3.9: Simulated (HFSS) S-parameters of Design A of the Microstructure Branch-line Coupler

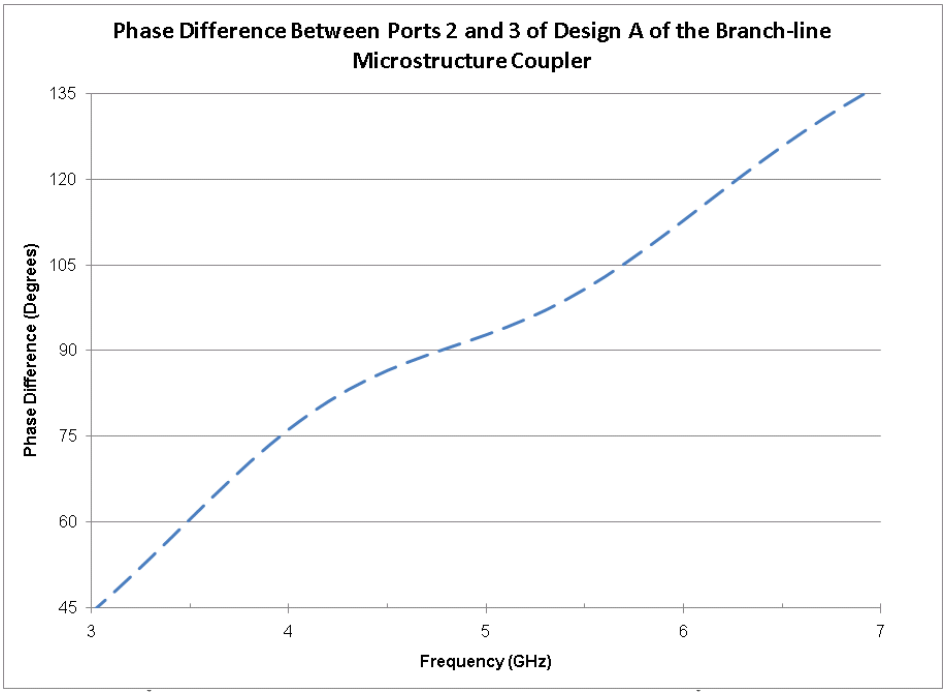

Figure 3.10: Simulated (HFSS) Phase Difference between the Through and Coupled Outputs of Design A of the Microstructure Branch-line Coupler

3.5.2 Simulation Results of Design B of the Microstructure Branch-line Coupler

Figure 3.11 to Figure 3.13 shows the ideal performance results of Design B of the microstructure coupler (shown in Figure 3.8) from 3.5 GHz to 7.5 GHz, on a quartz glass substrate (thickness = 1 mm, ε_r = 3.78, and tan δ = 0). The layout of Design B was also simulated on an alumina substrate (thickness = 1 mm, ε_r = 9.4, tan δ = 0.006) for comparison, to show how the performance vs. frequency of the coupler design is affected with a change in substrate.

Figure 3.11 is a plot of the ideal reflection ($|S_{11}|$) and through output ($|S_{21}|$) of Design B of the microstructure branch-line coupler, with the ideal optimized lumped element reflection and through output plotted on the same graph. Figure 3.12 shows the ideal coupled output ($|S_{31}|$) and isolation ($|S_{41}|$) of Design B of the microstructure coupler, with the ideal optimized lumped element isolation and coupled output also shown for comparison. Figure 3.13 shows the ideal phase difference between the through (Port 2) and coupled (Port 3) outputs of the coupler, with the ideal optimized lumped element phase difference also included.

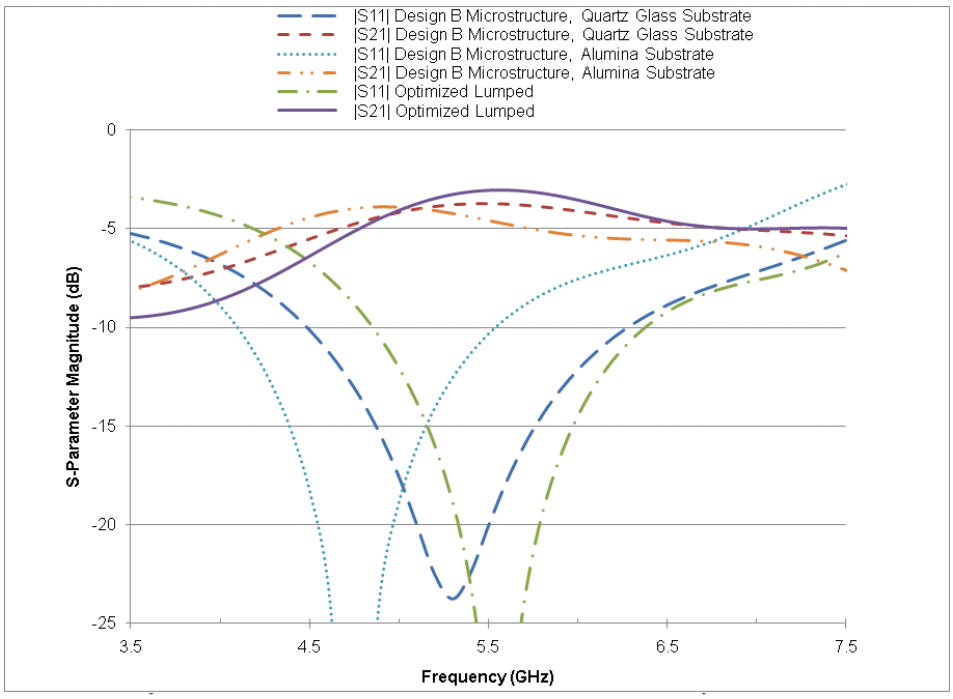

Figure 3.11: Simulated $|S_{11}|$ and $|S_{21}|$ of Design B of the Microstructure Branch-line Coupler

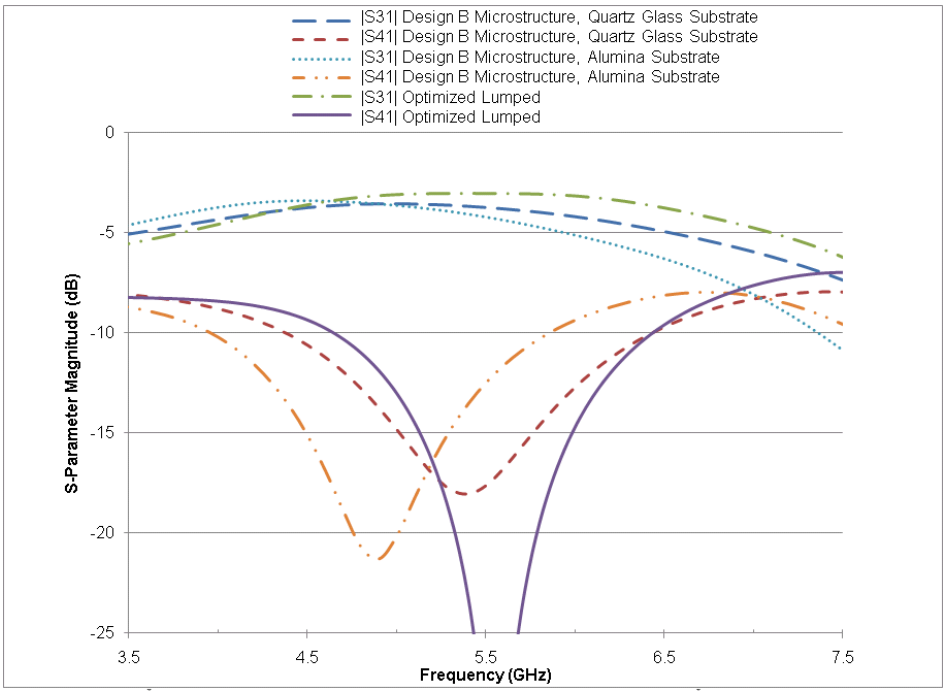

Figure 3.12: Simulated $|S_{31}|$ and $|S_{41}|$ of Design B of the Microstructure Branch-line Coupler

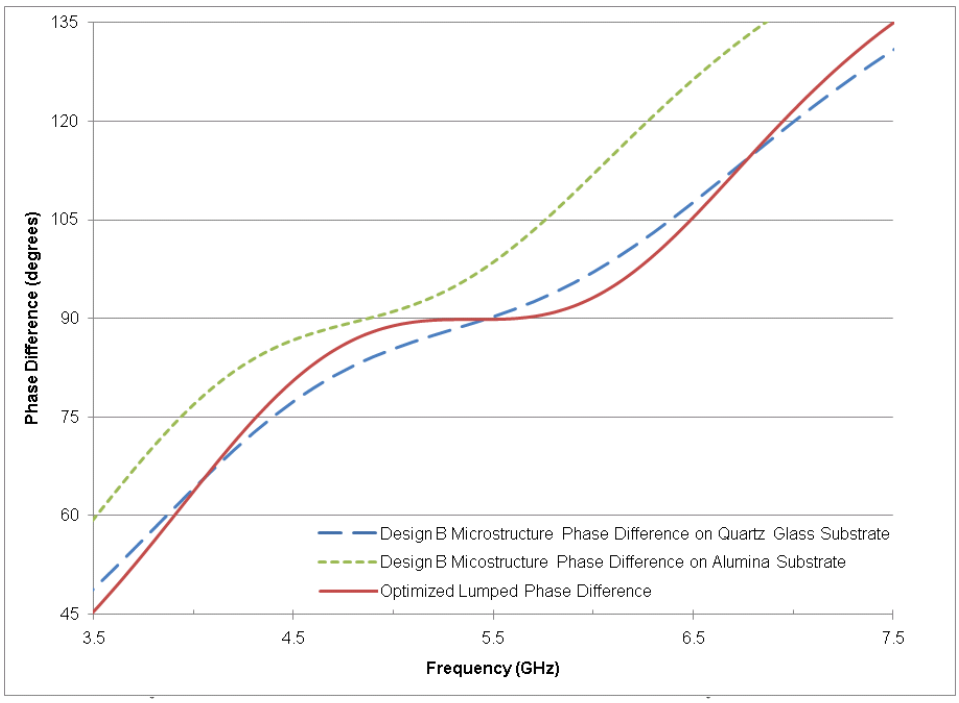

Figure 3.13: Simulated Phase Difference between the Through and Coupled Output Ports of Design B of the Microstructure Branch-line Coupler

3.5.3 Simulation Results of the Scaled Microstructure Branch-line Coupler

Figure 3.14 to Figure 3.15 shows the ideal performance results of the scaled version of the microstructure coupler (same design as shown in Figure 3.8, but all dimensions (length, height, width, gap sizes) decreased by 50%) for 7 GHz to 11 GHz, on a quartz glass substrate.

Figure 3.14 is a plot of the ideal reflection ($|S_{11}|$), isolation ($|S_{41}|$), through ($|S_{21}|$) and coupled outputs ($|S_{31}|$) of the scaled microstructure branch-line coupler. Figure 3.15 shows the ideal phase difference between the through (Port 2) and coupled (Port 3) outputs of the scaled microstructure coupler.

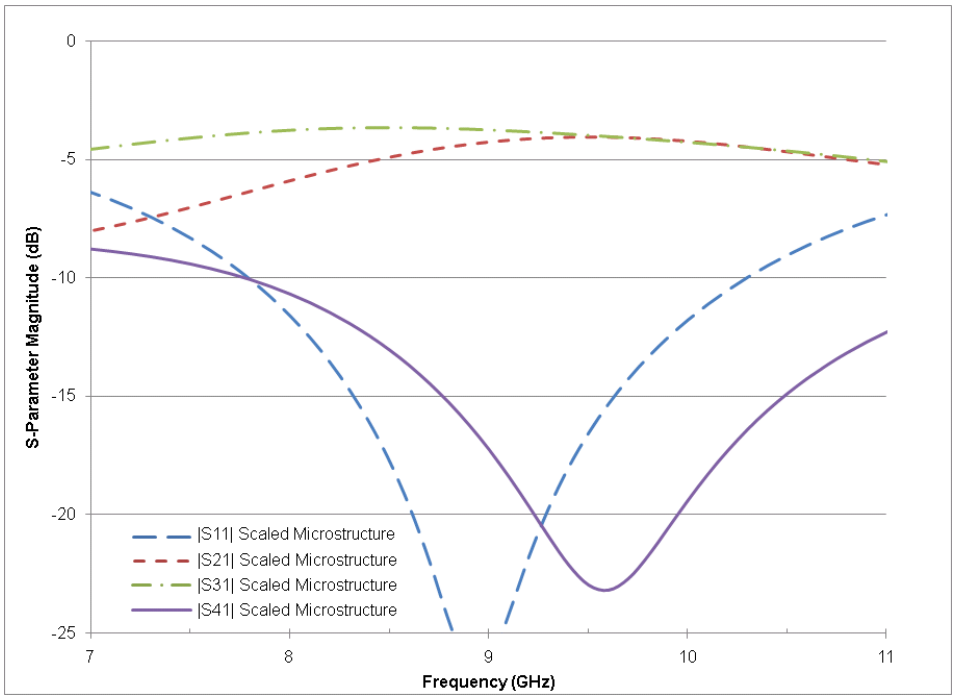

Figure 3.14: Simulated S-parameters of the Scaled Microstructure Branch-line Coupler

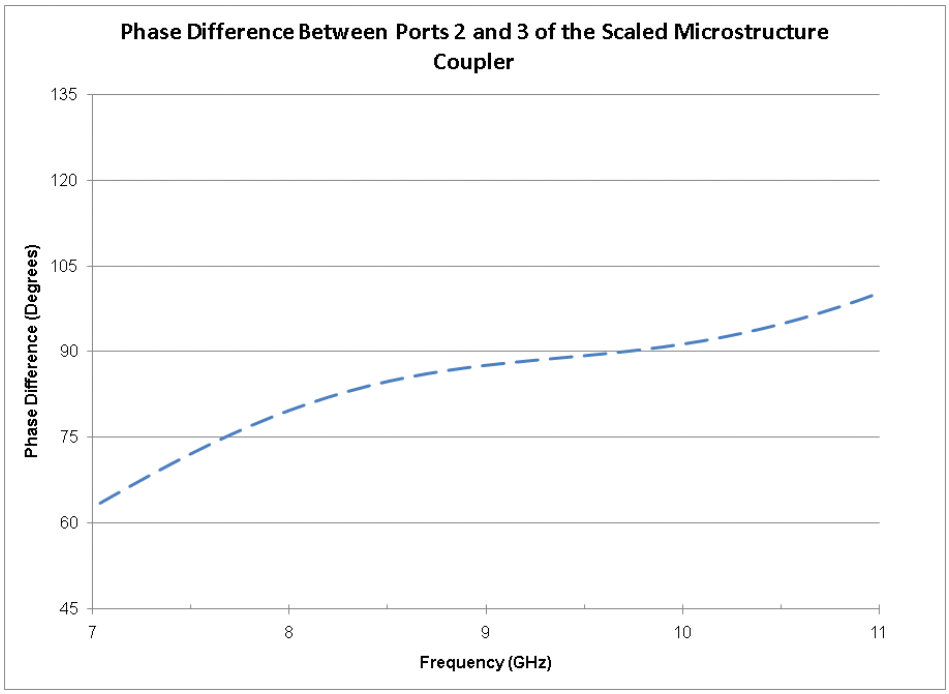

Figure 3.15: Simulated Phase Difference between the Coupled and Through Output Ports of the Scaled Microstructure Coupler

3.6 Discussion of the Microstructure Branch-Line Design and Simulation Results

The simulated microstructure branch-line couplers presented in the previous section have advantages and disadvantages when compared to transmission line and lumped element couplers. One key advantage of the microstructure branch-line design (in particular, Design B) is that the overall area of the coupler is much smaller compared to its distributed equivalent. This microstructure coupler design is 3.44 mm x 2.73 mm. The distributed 5.4 GHz branch-line coupler on quartz glass substrate is 7.83 mm x 8.03 mm. By changing the substrate type to alumina the distributed 5.4 GHz branch-line coupler is reduced to 5.18 mm x 5.38 mm. A graph showing the area reduction of Design B of the microstructure branch-line coupler compared to its distributed equivalent is shown in Figure 3.16 illustrating how much smaller the microstructure design is compared to the distributed coupler design.

Simulations revealed that the microstructure branch-line coupler is essentially lumped, which means that no re-entrant behavior was observed at frequencies simulated up to 20 GHz, so the physical size of the coupler structure will remain the same for the coupler on quartz and alumina. The effect of changing the substrate from quartz to alumina resulted in a shift in the couplers operating frequency by 500 MHz from 5.4 GHz for a quartz glass substrate, to 4.9 GHz for an alumina substrate. The performance of the coupler on alumina substrate was quite comparable to the coupler on quartz glass. One difference between the performance was the power division between the couplers output ports was more even for the coupler on quartz glass substrate (-3.73 dB and -3.64 dB, compared to -3.88 dB and -3.57 dB). These values are slightly less then the ideal value of -3 dB most likely due to the metal losses introduced from simulating non-ideal nickel. The other main differences in performance were the coupler on alumina substrate had a slightly smaller 3-dB bandwidth (55.1% compared to 59.3%), but slightly larger isolation bandwidth (16.3% compared to 14.8%) and slightly larger phase bandwidth (18.4% compared to 16.7%).

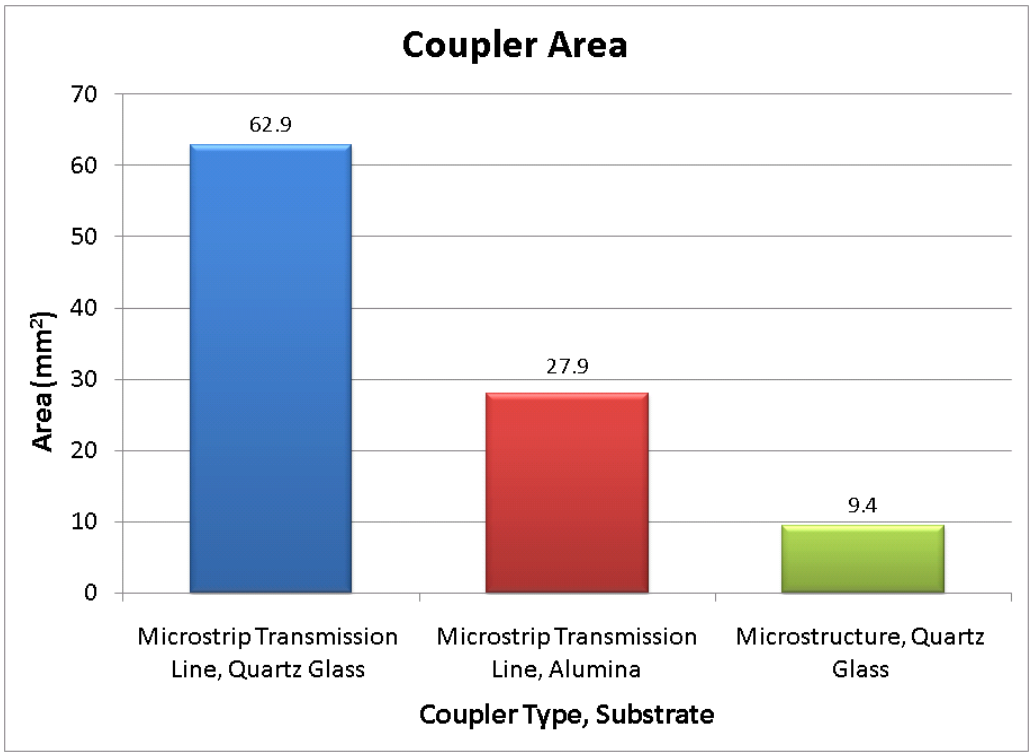

Figure 3.16: Distributed and Microstructure Branch-line Design B Coupler Area

In simulation, Design B of the microstructure branch-line coupler, on quartz glass substrate, had a larger 3-dB bandwidth of 59.3% compared to 54.2% of its optimized lumped element equivalent. The optimized lumped element equivalent of Design B was modeled using ideal lossless lumped elements. The isolation bandwidth of Design B is 1% less than the optimized lumped element coupler. The phase difference between Port 2 and Port 3 at the operating frequency of this structural design is 89.3°. This is quite comparable to the phase difference of the optimized lumped element coupler of 89.9°. The ±5° phase bandwidth of this structural design is 16.7%, which is about 9.5% smaller than the optimized lumped element couplers. The other branch-line microstructure coupler designs had comparable performance, and sometimes larger bandwidths, but these larger bandwidths resulted in a trade off of lossier $|S_{21}|$ and $|S_{31}|$ values, or more uneven power division between ports 2 and 3. A summary of the performance of the microstructure branch-line coupler designs is provided in Table 3.2. Design B of the microstructure branch-line coupler was chosen as one of the designs to be fabricated because it had the most even power division between ports 2 and 3, with a larger 3-dB bandwidth, and comparable output phase difference and isolation bandwidth to the optimized lumped element coupler. The reduced

area version of Design B, with very close inductors was also chosen for fabrication since this coupler was even smaller in area and still had acceptable performance.

Table 3.2 provides a summary of the performance for the various designs of the microstructure branch-line coupler. The optimized lumped element branch-line coupler is also included for comparison.

Table 3.2: Performance Summary of the Microstructure Branch-line Coupler Designs

Branch-Line Coupler Comparison							
Type	Op. Freq (GHz)	3-dB BW (%)	$\|S_{21}\|$ at Op. Freq. (dB)	$\|S_{31}\|$ at Op. Freq. (dB)	Phase difference between Port 2 and Port 3 at Op. Freq.	Isolation BW (%)	Phase BW (%)
Optimized Lumped	5.40	54.2	-3.10	-3.01	89.9°	15.8	26.1
Design A, Quartz Glass	4.90	61.2	-3.96	-3.60	91.7°	6.1	16.3
Design B, Quartz Glass	5.40	59.3	-3.73	-3.64	89.3°	14.8	16.7
Design B, Alumina ε_r=9.4	4.90	55.1	-3.88	-3.57	90.3°	16.3	18.4
Reduced Area Microstructure, Alumina ε_r=9.8	5.05	63.3	-3.77	-3.61	90.0°	15.6	19.2
Rescaled Microstructure	9.40	53.8	-4.08	-3.86	88.8°	18.2	21.5

3.7 Microstructure Rat-Race Design

The microstructure rat-race coupler design is based on the schematic of the lumped element rat-race coupler using the lumped element values found through optimization in Section 2.4.2, and the microstructure lumped elements discussed previously. The microstructure rat-race coupler design has the dimensions of 3.99 mm by 4.78 mm with a height of 220 μm and is shown in Figure 3.17 along with the lumped element schematic. The dark grey lines are signal lines, and the lighter grey areas represent ground planes. There are three single loop inductors represented by square structures near the middle of the structure, and one double loop inductor on the right hand side of the structure. The six capacitors are formed by separating the signal lines and the ground plane by a 6 μm air gap.

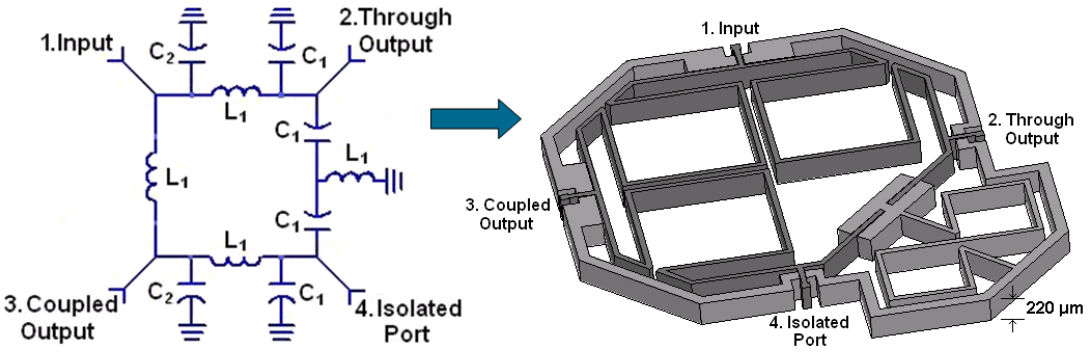

Figure 3.17: Schematic and Structural Design of the Microstructure Rat-Race Coupler

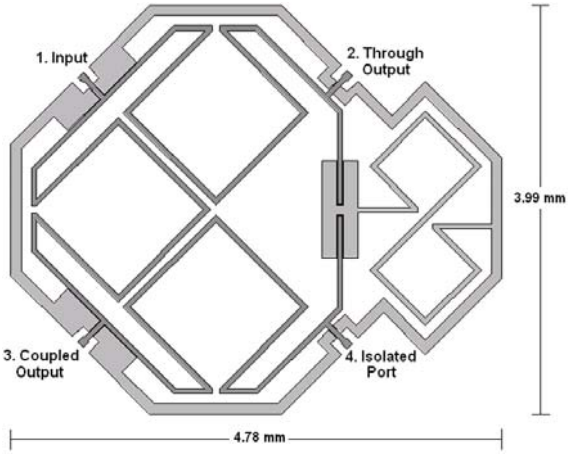

Figure 3.18: Top View of the Microstructure Rat-Race Coupler

3.8 Microstructure Rat-Race Simulation Results

The performance of the microstructure rat-race coupler on quartz glass substrate, shown in Figures 3.17 and 3.18, was simulated with HFSS. The results are shown in Figure 3.19 to Figure 3.22. The performance of the ideal lumped element rat-race coupler and the optimized lumped element rat-race coupler that achieves a larger 3-dB bandwidth is also provided to show the similarities between the lumped and microstructure design.

Figure 3.19 and Figure 3.20 show the simulated S-parameter magnitudes of the rat-race microstructure coupler from 3.5 GHz to 7.5 GHz, on a quartz glass substrate. Figure 3.21 shows the simulated phase difference between the through (Port 2) and coupled (Port 3) outputs of the rat-race coupler when Port 1 is used as the input port, and Figure 3.22 displays the simulated phase difference between the same outputs when Port 4 is used as the input port.

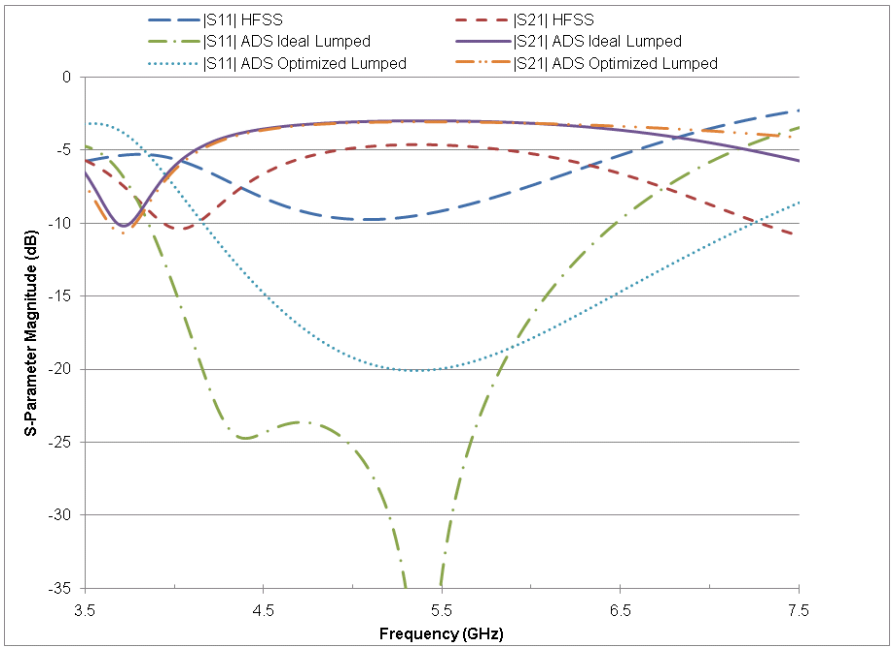

Figure 3.19: Simulated $|S_{11}|$ and $|S_{21}|$ of the Microstructure Rat-Race Coupler

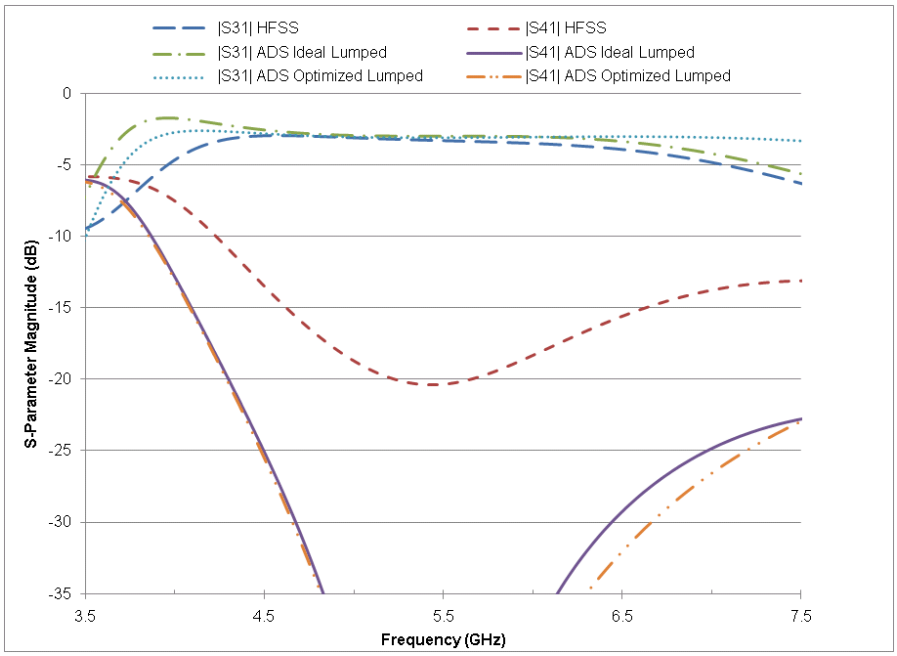

Figure 3.20: Simulated $|S_{31}|$ and $|S_{41}|$ of the Microstructure Rat-Race Coupler

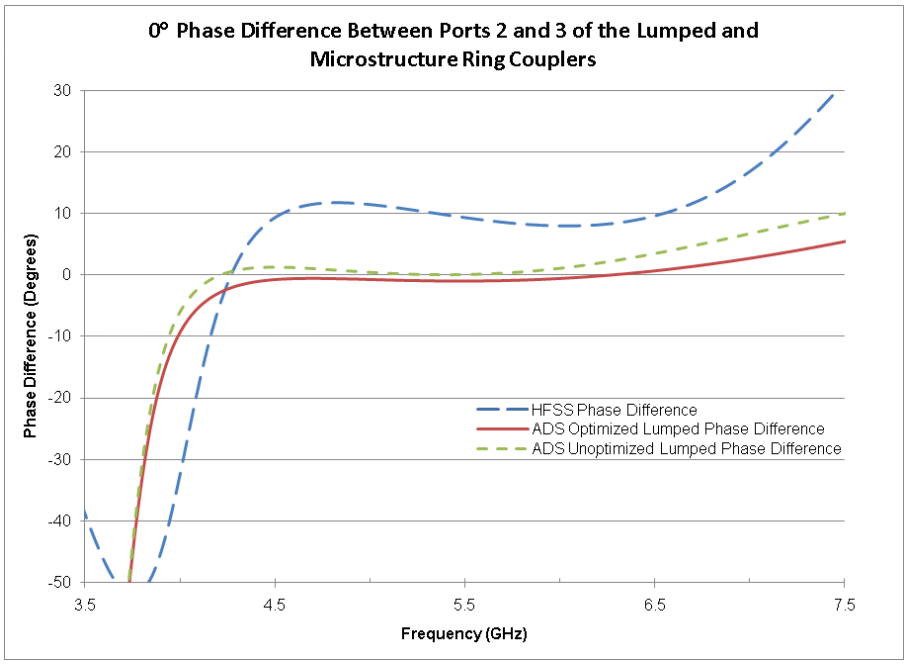

Figure 3.21: Simulated Phase Difference Between Ports 2 and 3 of the Microstructure Rat-Race Coupler when Port 1 is the Input Port

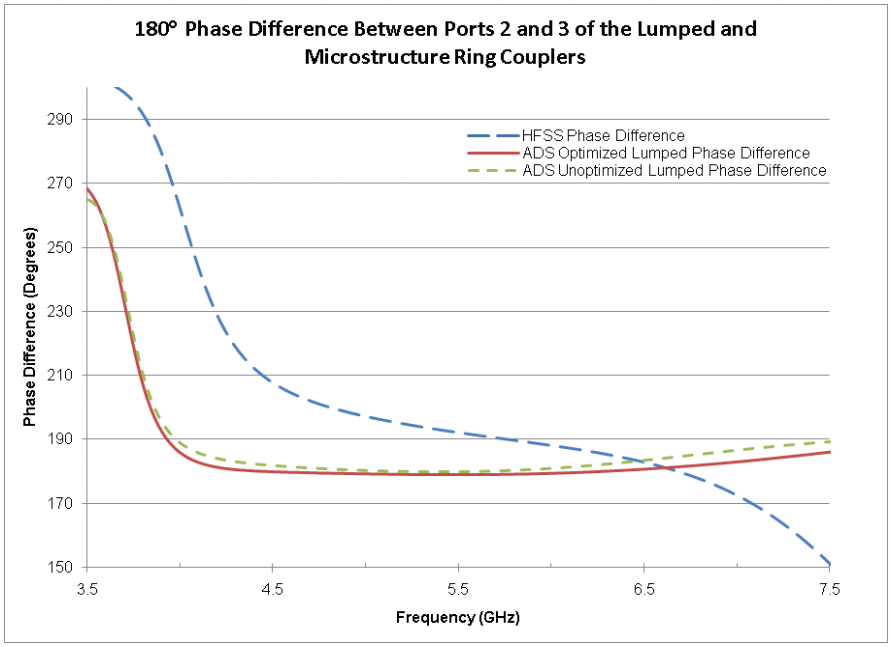

Figure 3.22: Simulated Phase Difference Between Ports 2 and 3 of the Microstructure Rat-Race Coupler when Port 4 is used as the Input Port

3.9 Discussion of the Microstructure Rat-Race Design and Simulation Results

The simulated microstructure rat-race coupler has advantages and disadvantages when compared to transmission line and lumped element couplers. The major advantage of the microstructure rat-race design over its distributed equivalent is the overall area of the microstructure coupler is much smaller. The microstructure rat-race design is 3.99 mm by 4.78 mm. The distributed 5.4 GHz rat-race coupler on quartz glass substrate is circular with a radius of 7.87 mm. The area of the distributed 5.4 GHz rat-race coupler can be reduced to a circle with a radius of 5.31 mm by changing the substrate type to alumina, which is still considerably larger than the area of the microstructure design. A graph showing the area reduction of the microstructure rat-race coupler compared to its distributed equivalent is shown in Figure 3.23.

Another advantage found through simulation that the microstructure rat-race coupler has over the distributed rat-race coupler is that it has no re-entrant behaviour since it is implemented with lumped element microstructures that have minimal distributed effects.

The performance of the microstructure rat-race coupler was found to be more lossy than its distributed and lumped element equivalents. One possible cause for the loss is the physical size of the coupler structure could be experiencing distributed losses (ie. loss per unit length). Another factor that could be contributing to the loss is the interference of the magnetic fields between the large single loop inductors. The single loop inductors were placed very close together in the rat-race structure to try to reduce the overall area, but as a result the area of the inductors magnetic fields overlap. It was important to keep the area of the coupler as small as possible so that distributed effects, such as loss per unit length and effects on performance due to the substrate would be minimized, and reentrant behavior would be avoided. The most obvious factor that results in the rat-race microstructure coupler having more loss than the presented distributed and lumped element rat-race simulations is that the distributed and lumped element simulations used ideal, lossless elements, where as the structural simulation introduced loss by using a finite conductivity for the metal. The rat-race microstructure coupler simulated values of $|S_{21}|$ and $|S_{31}|$, at the operating frequency of 5.36 GHz, were -4.59 dB and -3.23 dB. The bandwidths of the microstructure rat-race coupler were found to be 44.6% for the 3-dB bandwidth, 37.3% for the isolation bandwidth and 47.6% for the ±5° phase bandwidth where ideally the phase difference between the

through and coupled ports of the coupler would be 0° when port 1 is used as the input. The value of the phase difference found from simulation results was 10.0°. When port 4 was used as the input port the phase difference between the coupled and through outputs was found to be 193.4°, when ideally it should be 180°. The ±5° phase bandwidth in this case was determined to be 19.2%, which is slightly higher than the ideal distributed couplers ±5° phase bandwidth, but is much lower than its ideal lumped and optimized lumped element coupler equivalents. The broadband behavior of the phase difference between the output ports of the microstructure rat-race coupler shows that the structural design is more similar to its lumped element equivalent circuit than to its distributed equivalent. The phase difference of the distributed rat-race coupler, shown in Figure 2.26 and 2.27, varies almost linearly with frequency around the centre frequency. Table 3.3 provides a summary of performance for the microstructure rat-race coupler, distributed rat-race coupler, and ideal lumped and optimized lumped rat-race couplers for comparison.

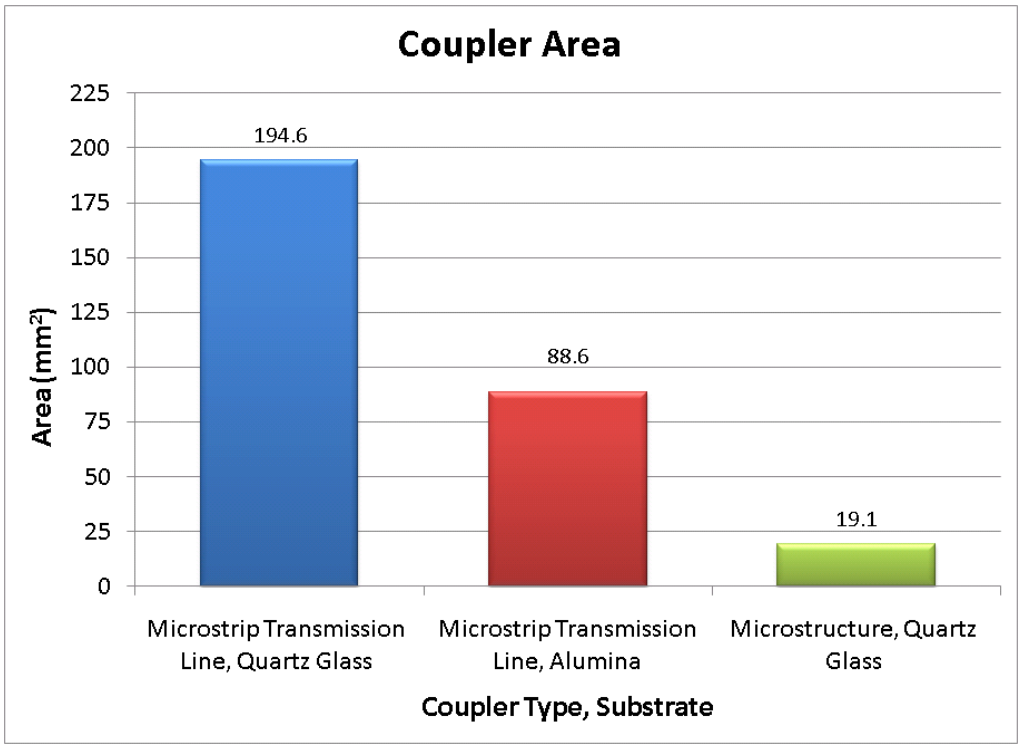

Figure 3.23: Distributed and Microstructure Rat-Race Coupler Area

Table 3.3: Performance of the Microstructure Rat-Race Coupler

180° Rat-Race Coupler Comparison							
Type	Op. Freq (GHz)	3-dB BW (%)	$\|S_{21}\|$ at Op. Freq. (dB)	$\|S_{31}\|$ at Op. Freq. (dB)	Phase difference between Port 2 and Port 3 at Op. Freq.	Return Loss BW (%)	180° Phase BW (%)
Ideal Distrubuted	5.40	55.3	-3.01	-3.01	180.0°	55.8	15.8
Ideal Lumped	5.40	66.5	-3.01	-3.01	180.0°	49.6	47.7
Optimized Lumped	5.40	88.1	-3.05	-3.06	179.0°	59.2	57.8
Microstructure	5.36	44.6	-4.59	-3.22	193.4°	12.9	19.2

3.10 Chapter Summary

In this chapter the designs and simulation results of the branch-line and rat-race microstructure couplers were revealed and discussed. The reduced area microstructure branch-line design was 85% smaller than its distributed equivalent coupler on quartz glass substrate. The performance of the reduced area microstructure branch-line coupler had almost even power division between the output ports, although the values were slightly lower than -3 dB (value obtained from lossless distributed and lossless lumped element simulations) this is acceptable because the conductivity of the metal for the structural simulation was given a finite value to simulate the loss that is expected to occur in the fabricated device, due to the metal not being a perfect conductor. This branch-line microstructure design had comparable isolation bandwidth and phase difference at the operating frequency of 5.4 GHz to its optimized lumped element equivalent coupler. Although the ±5° phase bandwidth was smaller for this microstructure design, the 3-dB bandwidth was larger than its optimized lumped element equivalent coupler. Design B and the reduced area microstructure branch-line designs were chosen for fabrication over Design A since they had more even power division and their performance was more comparable to the optimized lumped element equivalent coupler.

The microstructure rat-race coupler design was 90% smaller in area than its distributed equivalent on quartz glass substrate. The simulated performance of this design showed more loss, a phase difference between the output ports at the operating frequency that was about 10° larger than desired and generally smaller bandwidths than its distributed and lumped element equivalents. Although the simulated performance was not as good as expected due

to distributed effects, and interference between the magnetic fields of the inductors, the microstructure rat-race design did show that the device was operating as expected.

The next chapter presents the fabricated microstructure branch-line and rat-race couplers and their testing results.

CHAPTER 4
FABRICATION AND TESTING RESULTS

This chapter presents the fabricated microstructure branch-line and rat-race couplers, difficulties and challenges encountered with testing the coupler, solutions to some of the challenges, and a discussion of the testing results.

4.1 Layout Design

The layout designs of the microstructure branch-line and rat-race couplers are shown in Figure 4.1. Figure 4.1(a) is based on Design B of the microstructure branch-line coupler discussed in Chapter 3 and will be referred to as the non-capacitance compensated microstructure branch-line coupler in this chapter.

All of the layouts are slightly different from the simulated structures. The areas that will be initially fabricated as long thin polymer beams (that later form the long capacitance air gaps of the structure) require extra support so that the polymer beams do not become bent from the stress of electroplating the metal structure. To provide the extra strength the triangular shaped voids were added in the layout. The addition of the triangular shaped voids was proven to work successfully in [23]. With the addition of the triangular shaped voids, it is expected that the value of the capacitance will decrease. To compensate for the loss of capacitance, extra metal equal to the length of all the openings of the triangular shaped voids was added along the signal line to create additional capacitance. This layout is shown in Figure 4.1 (b).

Another difference between the coupler layouts and the simulated structures is the capacitance gap size. In the layout the gaps were increased from 6 μm to 8 μm. This was performed since previous structures fabricated with D-XRL experienced shrinking in their polymer beams which led to gaps that were approximately 2 μm smaller than expected.

The last difference between the simulated structures and the layouts is that all of the structures corners have been rounded on the layout. The rounded corners reduce the risk of the resist cracking during the fabrication process.

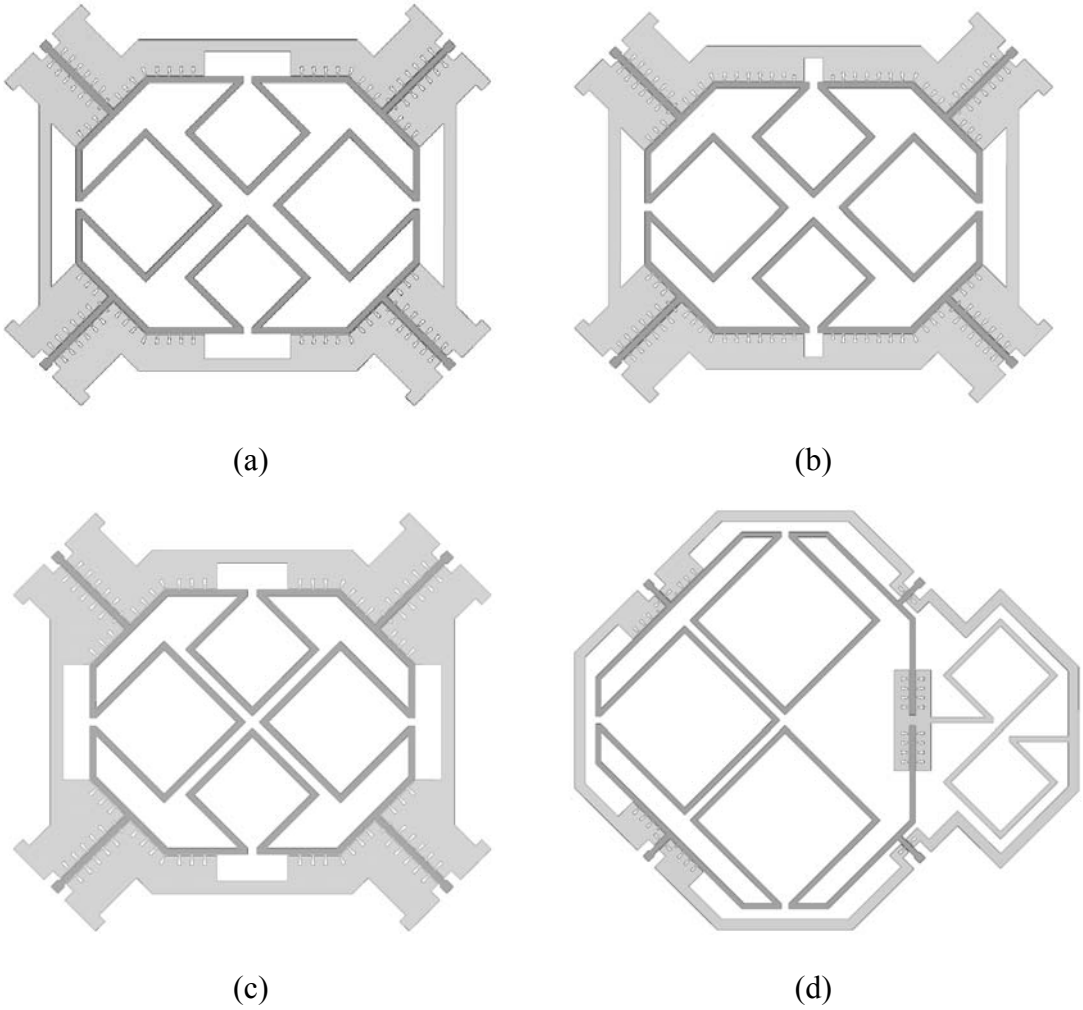

Figure 4.1: Layouts for the Microstructure Couplers (a) Branch-line Without Extra Capacitance (b) Branch-line With Extra Capacitance (c) Reduced Area Branch-line (d) Rat-Race Coupler

4.2 Fabricated Couplers

The microstructure couplers were fabricated at the Karlsruhe Nano Micro Facility (KNMF) at the Karlsruhe Institute of Technology (KIT) in Germany. X-ray exposures were performed at the KIT 2.5 GeV electron storage ring ANKA, beamline Litho2. The microstructure couplers were fabricated on 1 mm thick alumina ceramic wafers and on 0.5 mm thick quartz glass. Both substrate types were previously coated with an oxidized

titanium seed layer for electroplating. A 350 µm thick PMMA layer was added to the thin metal film prior to exposure. After the exposure and development, nickel electroplating in the voids of the polymer template was performed at room temperature as described in [32].

Scanning electron microscope images of a fabricated capacitance compensated microstructure branch-line coupler (layout of Figure 4.1 (b)) on alumina substrate are provided in Figure 4.2 to Figure 4.6. Figure 4.2 shows the overall view of the coupler. Figure 4.3 provides a closer view of the inductors where the nearly vertical side walls can be seen. Figure 4.4 shows an even closer view of the base of an inductor, which also shows the nearly vertical smooth side walls of the small capacitance gaps. A close view of one of the ports is also provided in Figure 4.5 where the capacitance gap and tall nearly vertical side walls of the structure can be viewed. Unfortunately, not all of the coupler devices on this wafer were testable due to distortions. Figure 4.6, taken at IMT/KIT, shows a distorted port that has a bend in the signal line. The distortions were caused during mask processing and also potentially by heating of the mask during X-ray exposures where certain areas of the mask, and wafer were affected by the heat more than others, due to their position with the beamline.

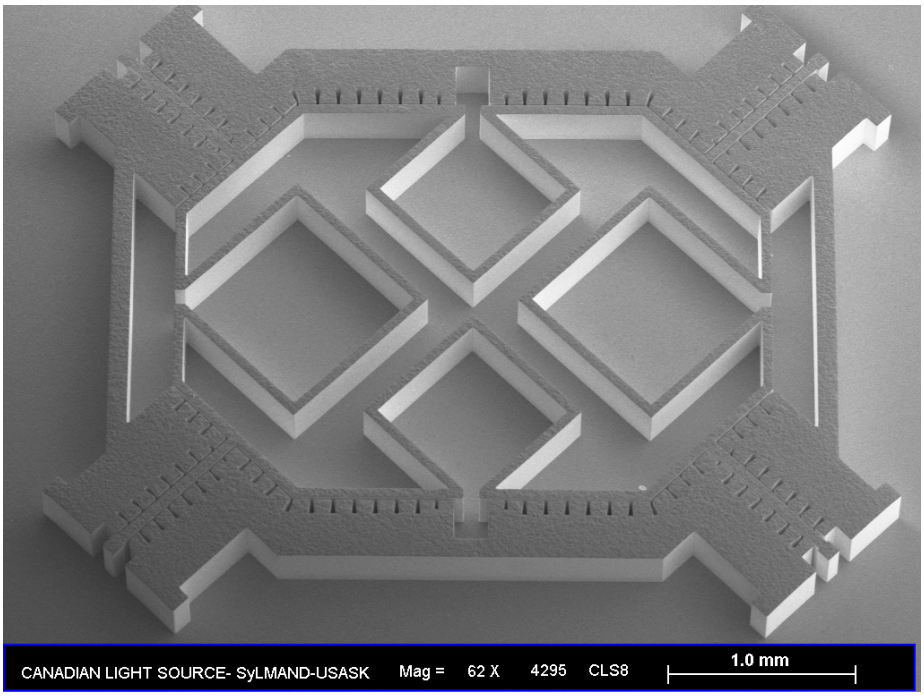

Figure 4.2: Overview of the Capacitance Compensated Branch-line Coupler (Average Nickel Height of 265 µm, Average Gap Size of 11.5 µm, on 1mm Alumina Substrate)

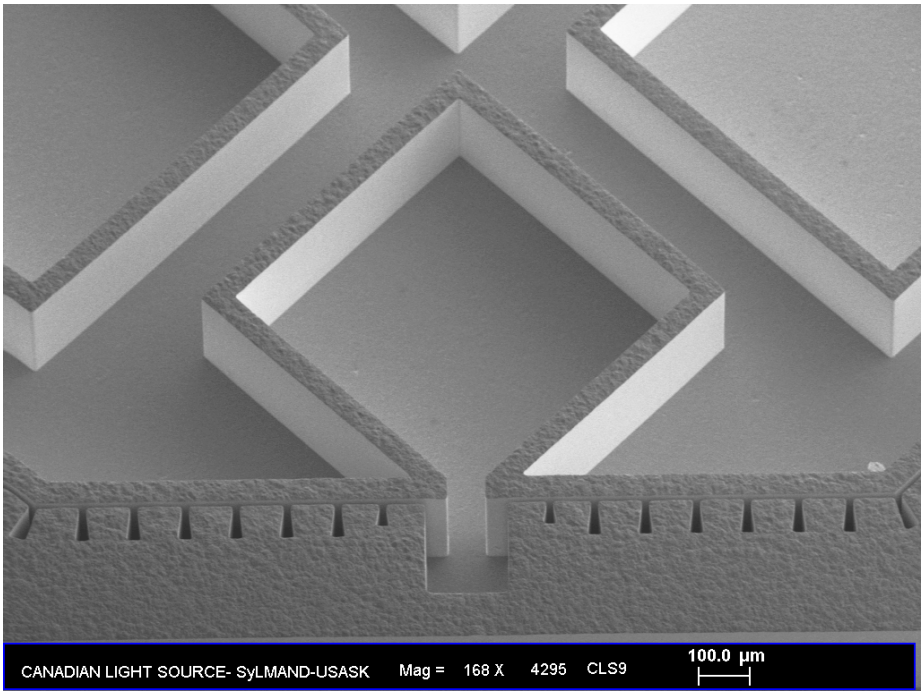

Figure 4.3: View of one of the Small Inductors in the Capacitance Compensated Branch-line Coupler (Close-up of Figure 4.2)

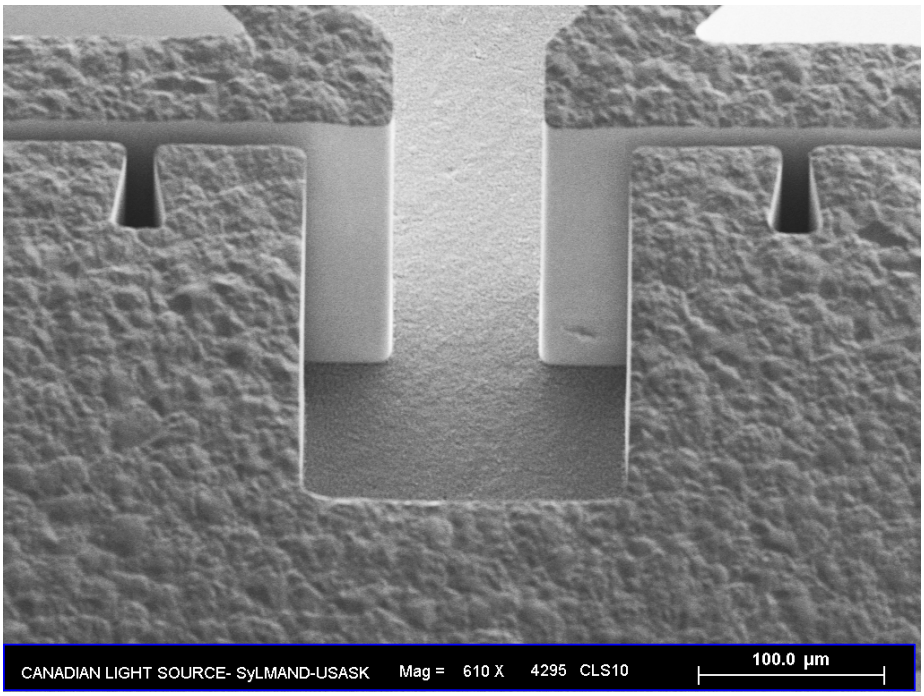

Figure 4.4: Closer View of the Base of an Inductor from the Capacitance Compensated Branch-line Coupler that also shows the Smooth Nearly Vertical Sidewalls of the Structure and a Capacitance Gap

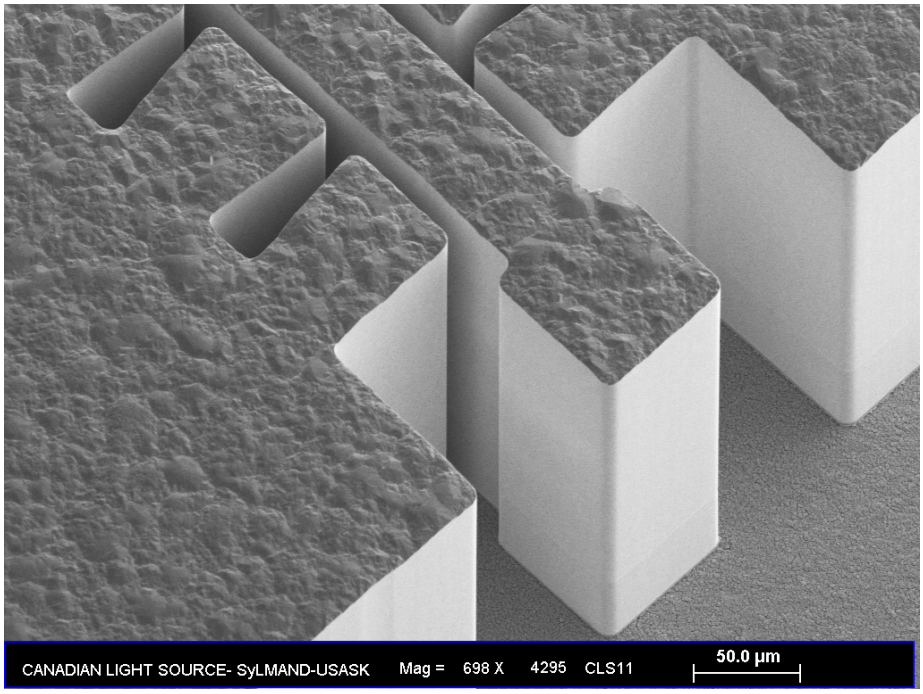

Figure 4.5: View of a Port from the Capacitance Compensated Branch-line Coupler which also shows a Capacitance Gap and Nearly Vertical Sidewalls.

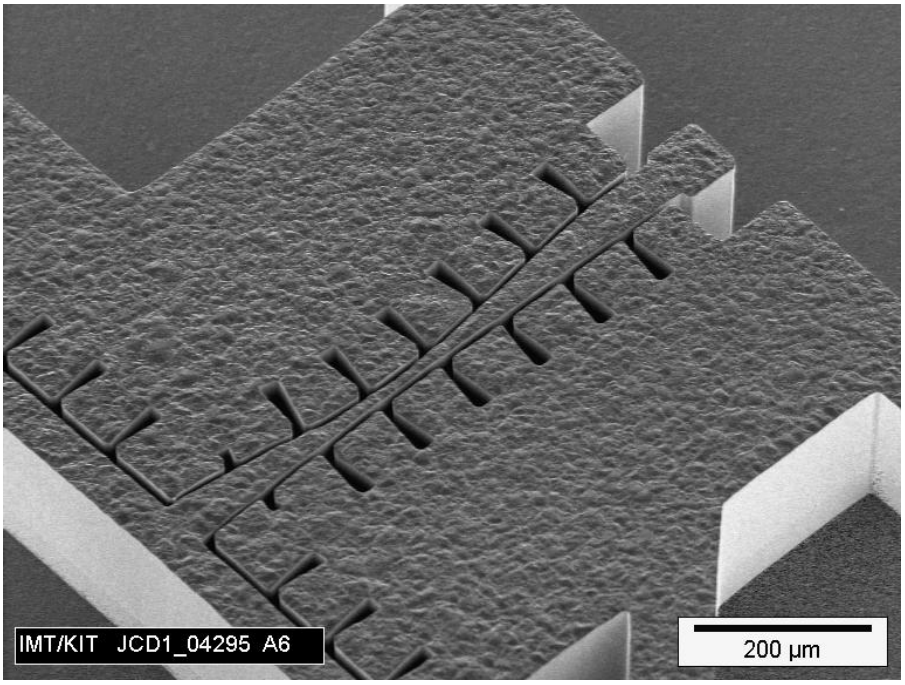

Figure 4.6: View of a Distorted Port of a Branch-line Coupler. Image courtesy of IMT/KIT.

4.3 Etching Procedures

The preliminary step before testing of the fabricated couplers was to locally remove the titanium seed layer exposed to air, while maintaining the seed layer underneath the nickel structure. Removing the exposed titanium seed layer is required so that the signal lines and ground planes are no longer electrically shorted together. Two different procedures were used to perform the etching.

4.3.1 Etching Procedure 1

In the first etching procedure the titanium seed layer was removed by placing the wafer into an etchant of 1% hydro-fluoric (HF) solution, made from 80 mL of de-ionized (DI) water, and 20 mL of 5% HF solution. Two wafers were etched with this solution, one an alumina substrate and the other a glass substrate.

For the alumina wafer, the wafer was submerged in the etchant solution for 2 min and 35 seconds, followed by intervals of 30 to 45 seconds. Between intervals, the coupler was rinsed in DI water and tested to determine if the signal lines and ground planes were still shorted by placing a ground signal ground (GSG) micro-probe that was connected to an ohm-meter on one of the couplers ports. Figure 4.7 shows one of the microstructure couplers being tested for a short. Once the ohm-meter measured that one port had an open load (infinite resistance) between the ground planes and signal line, the other ports were tested with the ohm meter and since they had the same result no further etching was required. The total time that the wafer was placed in the etching solution was 5 minutes and 15 seconds.

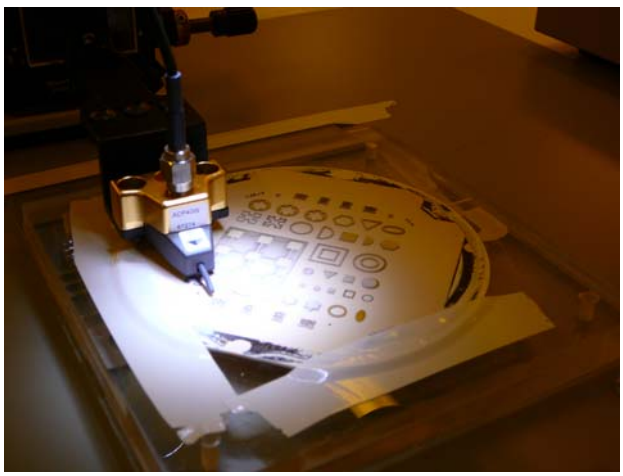

Figure 4.7: Microstructure Coupler Under Test for a Short Circuit

For the glass wafer, the wafer was submerged in the 1% HF and DI water etchant solution initially for 3 min and 6 seconds, where the majority of the titanium seed layer was removed. Since quartz glass is transparent the optical microscope was used to view (from the backside of the wafer) if there was any remaining titanium in the structures gaps instead of testing for short circuits with the GSG probes. Since titanium still remained in the gaps the wafer was re-submerged in the solution for approximately 1 minute intervals, until by visual inspection the gaps began to appear indicating that very little titanium remained. The intervals in the etchant solution were then shortened to approximately 30 seconds until it was visible with the optical microscope (by viewing the backside of the wafer) that all of the gaps were free of titanium. The total time that the glass wafer was placed in the etching solution was 9 minutes and 19 seconds.

The difference in etching times between the alumina and quartz glass wafer is due to the features of the coupler structures on these wafers being slightly different dimensions. The gap sizes of the structures on the alumina wafer were approximately double the size of the gaps of the structures on the glass wafer, making it easier for the etchant solution to travel down the larger gaps to etch away the titanium seed layer quicker. The problem of requiring such a long etchant time for the structures on the glass wafer is that the titanium layer underneath the signal line and inductor structures was almost completely removed, drastically reducing the adhesion of the signal line to the substrate. In some sections of the signal line and beneath the inductor structures there is no titanium layer remaining, so there is a small air gap between the nickel metal and the substrate in these areas. Figures 4.8 through 4.10 show the titanium layer of the coupler structure (viewed from the bottom of the wafer) after different times in the etchant solution.

In Figure 4.8, after 4 minutes and 9 seconds of etching, the coupler structure is shown as being almost completely light in color and solid, with only the dark triangular shaped voids present, but no capacitance gaps visible. The solid light color indicates the presence of the titanium seed layer. The darker color indicates that the titanium seed layer has been removed. After 7 minutes and 49 seconds in the etchant solution (Figure 4.9) the titanium seed layer is completely removed from the ends of the ports, and mostly removed from under the inductors (only a thin line of titanium, shown by the solid light color, remains on the corner of the upper inductor), but the required gaps are still not fully open. After 9 minutes

and 19 seconds in the etchant solution (Figure 4.10) the gaps are finally open, but there is no longer any titanium layer beneath the inductors. The signal line is essentially only anchored to the substrate by the remaining titanium layer in the port areas. Unfortunately, when the couplers on this quartz glass wafer were being probed for testing the signal lines became completely detached from the substrate, so no performance results could be measured.

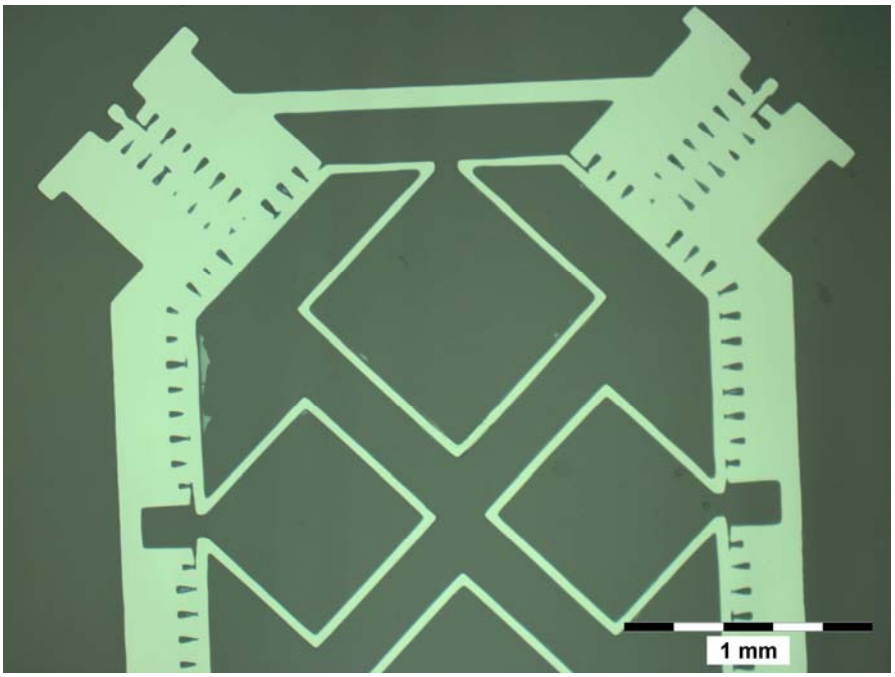

Figure 4.8: Titanium Layer after 4 minutes and 9 seconds of Etching

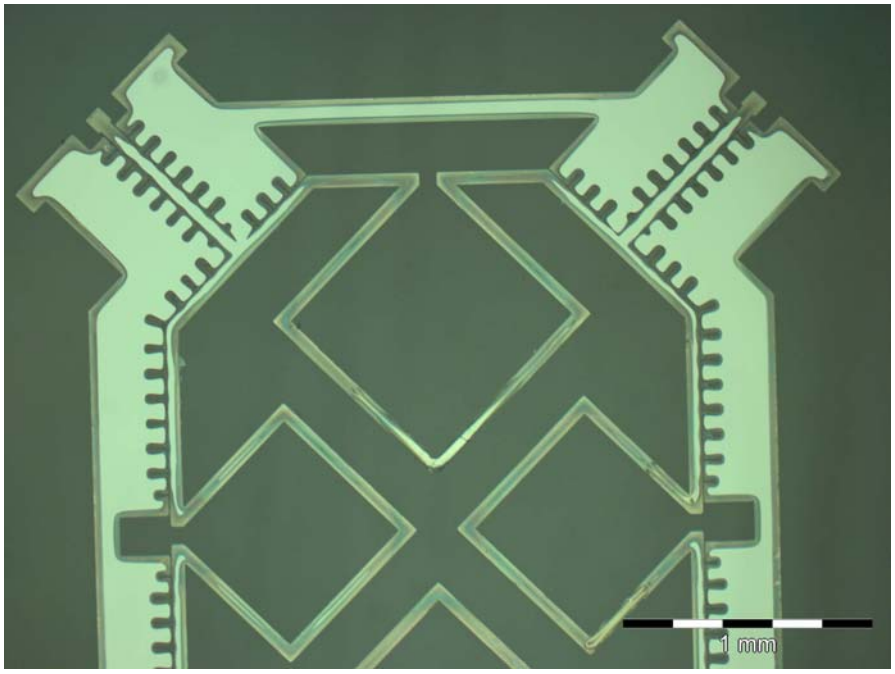

Figure 4.9: Titanium Layer after 7 minutes and 49 seconds of Etching

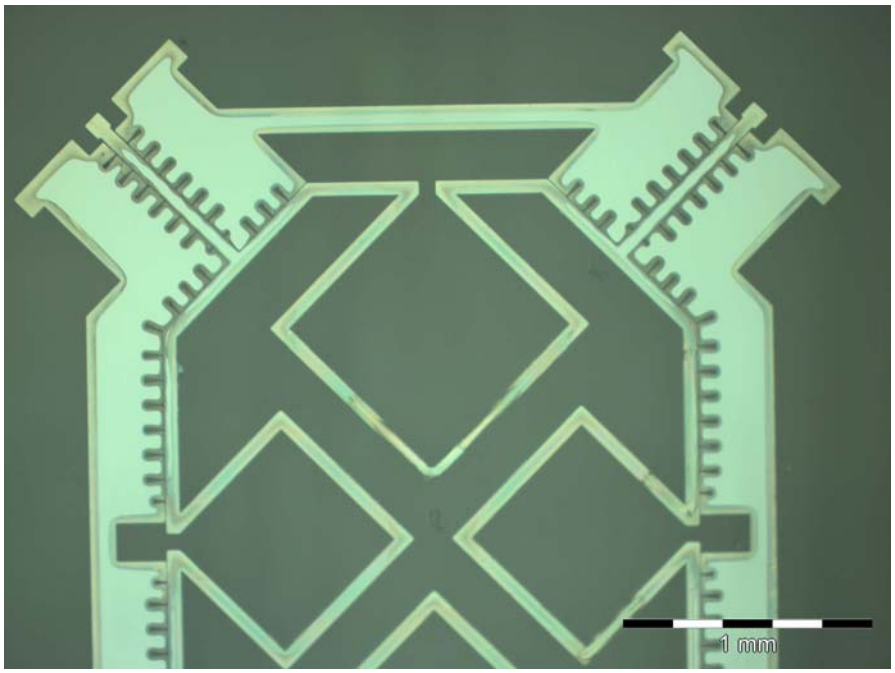

Figure 4.10: Titanium Layer after 9 minutes and 19 seconds of Etching

4.3.2 Etching Procedure 2

The objective of the second etching procedure was to find an etchant solution that was able to etch the titanium seed layer in the 6 μm gaps while not under etching the signal lines as much as in procedure 1. To increase the speed at which the etchant solution could reach the titanium seed layer in the 6 μm gaps, an etchant with a lower surface tension was chosen. The etching procedure also involved preliminary steps to ensure that the coupler structures were as clean as possible. The procedure is briefly described in the following steps:

1) Descum the wafer in oxygen plasma for two minutes using a reactive ion etcher to remove any resist residue. The plasma was set up with 80% oxygen and 20% argon, at a pressure of 20 mTorr, at 50 Watts.
2) Soak the wafer in acetone for 5 minutes to ensure that all oxides are removed.
3) Transfer the wafer from the acetone bath to an isopropanol bath and soak for 5 minutes. This step allows the isopropanol to completely fill the 6 μm gaps, and will help to draw the etchant solution into the gaps in the next step.
4) Transfer the wafer from the isopropanol bath into a 10% HF in isopropanol solution (10% HF, 10% H_20, 80% isopropanol). The 10% HF concentration was mixed by

diluting 48% HF with isopropanol instead of water, to achieve an etchant solution that has a lower surface tension than the 1% HF etchant solution used in procedure 1.

5) Leave the wafer in the HF/isopropanol etchant until the titanium seed layer is removed then transfer the wafer into a DI water bath to rinse off the excess etchant solution. If the wafer is removed from the etchant too early and needs further etching, steps 3 to 5 are repeated until the titanium seed layer is completely removed.

A glass wafer was etched using procedure 2 and it was found that less under etching occurred on the couplers signal lines compared to procedure 1, and the 6 μm capacitor gaps were still completely etched. Figure 4.11 shows a large area of a coupler's titanium layer after etching using procedure 2. Notice that the signal lines and ground planes throughout the structure are all a solid light color (indicating that the titanium seed layer is present) and all of the capacitance gaps are fully visible (dark in color).

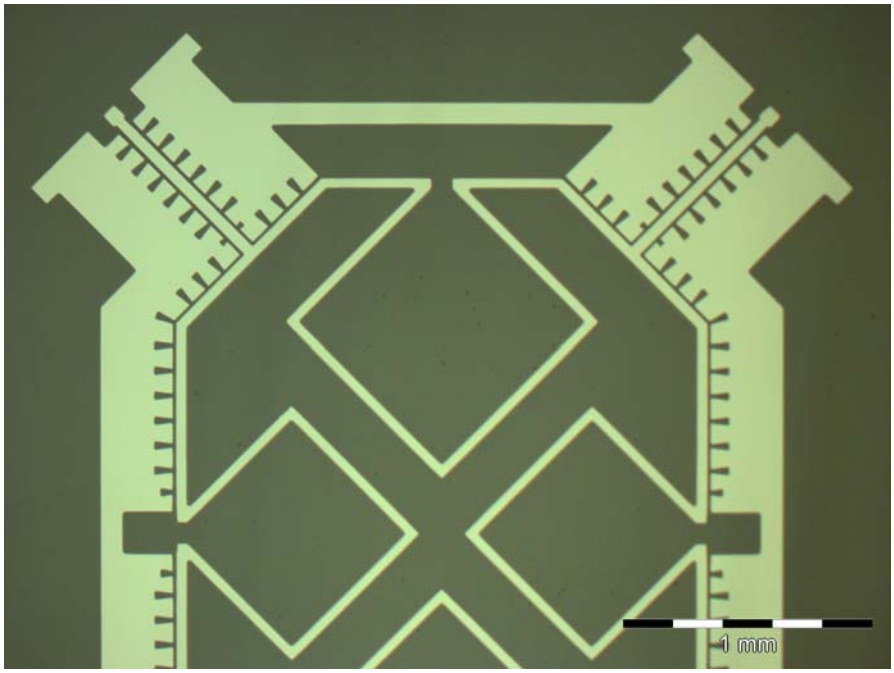

Figure 4.11: Titanium Layer after Etching using Procedure Two

Figure 4.12 is provided to show a comparison between the etching results of procedure 1 and 2. In Figure 4.12 (b), the square single loop inductors are still anchored to the substrate (this is shown by the inductors appearing solid and light in color, indicating that there is still titanium connecting the structure and the substrate). In Figure 4.12 (a) the inductors and the majority of the signal line are no longer solid or light in color. This indicates that the

titanium seed layer has been removed by etching so these portions of the structure are no longer connected to the substrate.

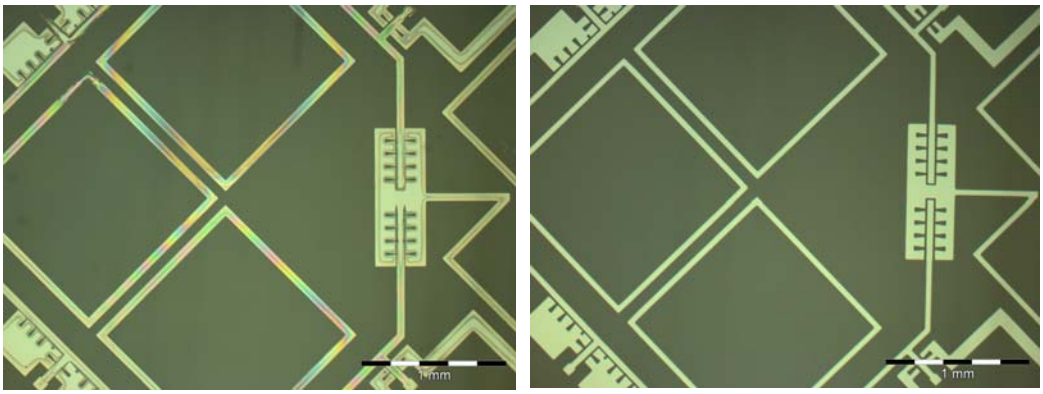

(a) (b)

Figure 4.12: Comparison of Etching Results (a) Procedure 1 (b) Procedure 2

4.4 Testing Procedure

After etching was completed the coupler structures were ready to be tested. The equipment used to measure the electrical performance of the coupler was a two port HP 8722ES vector network analyzer, four Cascade Microtech ACP40-W-GSG-150 micro-probes, four micro-positioners to hold and finely move the micro-probes, two 3.5 mm network analyzer cables, two semi-rigid 3.5 mm cables to connect the probes to the network analyzer cables, and two 20 dB attenuators for termination of the probes placed on the ports that are not connected to the network analyzer. The coupler testing apparatus is shown in Figure 4.13.

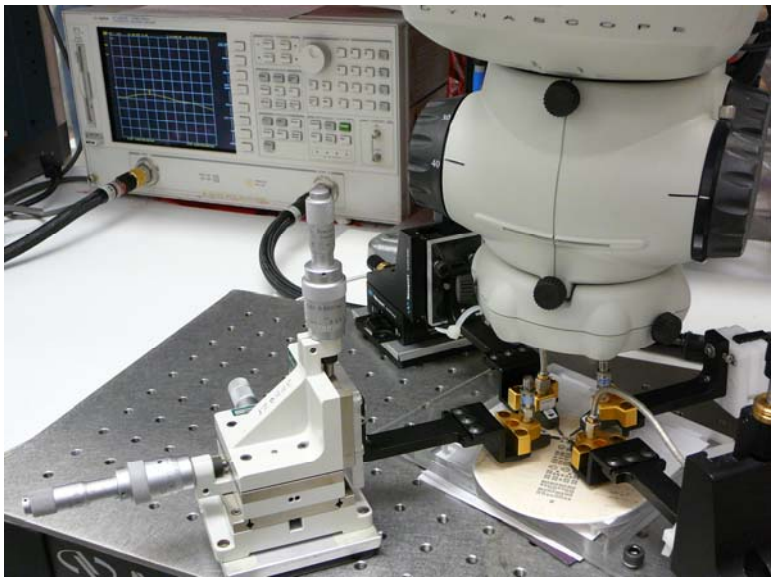

Figure 4.13: Coupler Testing Apparatus

To measure the S-parameters of the coupler the network analyzer was calibrated using a full two port short, open, load, thru (SOLT) calibration procedure, using a Cascade Microtech 101-190 impedance standard substrate, which provided short, load, and thru calibration standards. The open standards were measured with the probes tips lifted in the air. Calibration was required to remove the affects that the test set up (probes and cables) would introduce into the measurements performed on the coupler. For the S-parameter measurements the calibrated frequency sweep was set to start at either 2 GHz or 3.5 GHz and end at 7.5 GHz or 10.5 GHz (depending on the coupler style) using 1601 points, and an intermediate frequency bandwidth of 300 Hz.

To obtain the S-parameter measurements two ports of the coupler were connected to the network analyzer at time while the other two ports of the coupler were connected to micro-probes terminated with the 20 dB attenuators, to act as matched loads. Figure 4.14 illustrates the coupler connected to four micro-probes.

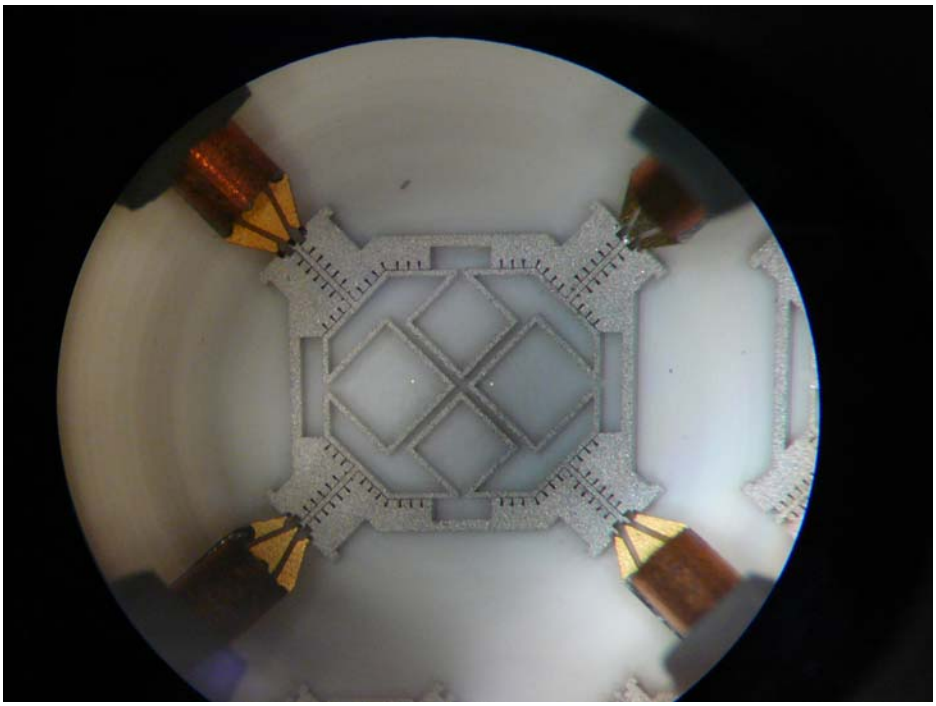

Figure 4.14: Test Set Up Showing all Four Microprobes Making Contact with the Couplers Ports

The loads and micro-probes connected to the network analyzer were moved around to the appropriate ports of the coupler to obtain measurements of S_{11}, S_{21}, S_{12}, S_{22}, S_{31}, S_{13}, S_{33}, S_{41},

S_{14}, and S_{44}. Only these S-parameters were required for bandwidth calculations and since the coupler is structurally symmetrical the performance should also be symmetrical.

To verify that the 20 dB attenuators provided matched terminations the return loss of a probe connected to a second probe (via a thru line) terminated with a 20 dB attenuator was measured. The results are shown in Figure 4.15. Over the frequency span of 4.5 GHz to 8.5 GHz, the worst value of the return loss was 17.2 dB at 8.0 GHz, and the best value of return loss was 22.5 dB at 4.6 GHz. Since the return loss measurement stays better than 15 dB, very little signal is being reflected back into the transmitting probe, indicating that the 20 dB termination is absorbing the transmitted signal, and acting as the required matched load.

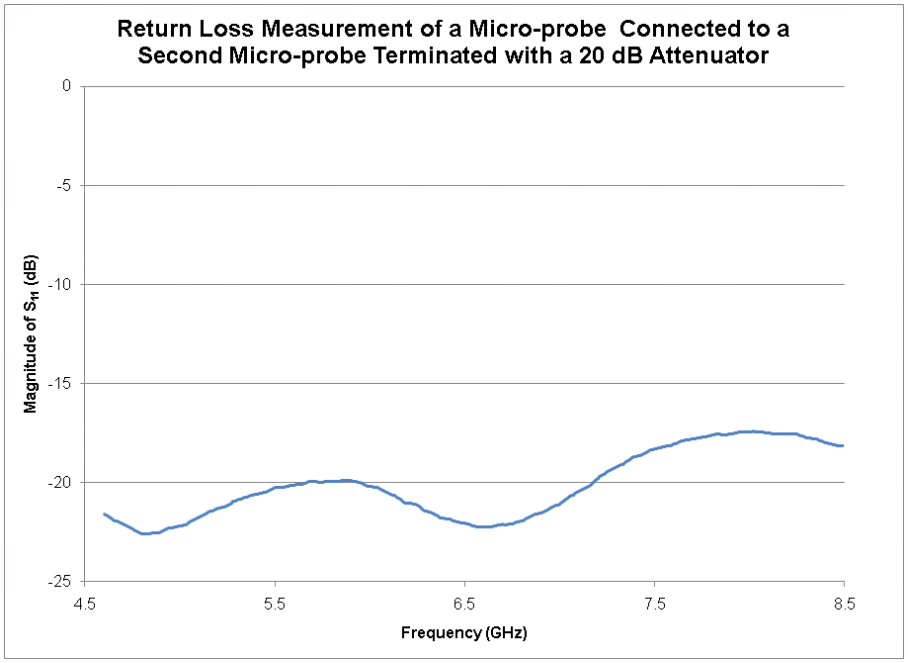

Figure 4.15: Return Loss (- dB (S_{11})) Measurement of a Micro-probe Connected to a Second Micro-probe Terminated with a 20 dB Attenuator

4.4.1 Difficulties and Challenges Encountered During Testing

In total only 5 coupler devices out of over 30 were suitable for testing. The other fabricated couplers either had major distortions, very uneven metal heights (up to 20 µm difference) between signal line and ground planes which made probing with the micro-probes impossible, resist that was stuck in the gaps, which prevented the titanium oxide seed layer from being fully etched away, resulting in the signal line and ground planes remaining

shorted together, or after etching were no longer sufficiently anchored to the substrate to endure testing.

The capacitance compensated coupler (on alumina substrate) that was tested had height differences between the signal line and neighboring ground planes at its ports that ranged from 4 μm to 9 μm. The 9 μm height difference, although not very large, still caused difficulties in contacting both ground planes and signal line at the same time with the micro-probe. When poor contact was made (ie. the signal line and only one ground plane contacting the microprobe), the performance results of the coupler were degraded due to the four ground planes not being all connected together and the port with a poor contact not being terminated properly with a matched load.

Another problem encountered with the coupler devices on certain alumina wafers is that the gap capacitance size was much larger than expected, and the metal height was also taller than expected. The larger gap size decreased the expected value of the capacitance, and the extra metal height was added to try to compensate for the lost capacitance. A problem with electroplating the metal higher is that the areas of the structure that are uneven in height continue to grow at uneven rates, making the height differences between different sections on the structure even greater. The reason that the gap sizes of the couplers on certain alumina wafers ended up larger than the designed value is because during the mask fabrication distortions occurred. The distortions were then transferred to the coupler structures by the X-ray lithography step. The mask was an experimental mask, which was fabricated with a new process, and had the advantage of being able to expose a larger area of the wafer than the previously used rectangular style mask. A rectangular style mask was later made and all structures fabricated with this mask had much closer gap sizes to the layout.

4.4.2 Polishing Technique to Reduce the Challenge of Testing Structures of Non-Uniform Height

One of the biggest issues faced during testing was trying to make contact with all the coupler's ground planes and signal lines, which often were of different heights. To make the structures height uniform a polishing technique described in detail in [33] was performed during the coupler structure's fabrication. Figure 4.16 shows a section of a non-polished coupler. Notice the roughness of the structures top surface, due to electroplating. To achieve a uniform height, the basic steps performed on the coupler structures were:

1) to polish the entire electroplated nickel wafer mechanically to a uniform height with the resist still in place to provide extra strength to the small features of the structure. The mechanical polishing causes the metal to become smeared leaving a thin overhanging edge of metal over all of the openings (gaps, triangular shaped voids, etc.) of the structure. The smeared metal almost completely covers a capacitance gap for the structure shown in Figure 4.17. This structure's resist was removed after mechanical polishing was completed for imagining purposes only.
2) to electropolish the structures to remove the thin metal overhang that resulted due to the mechanical polishing. Electropolishing is basically the reverse procedure of electroplating. As in electroplating, the wafer is placed in an electrolytic solution with an anode and a cathode, but for electropolishing is connected to the anode. When a voltage is applied between the anode and the cathode the induced electric field causes pieces of the thin metal overhang to be removed from the structure. The small metal pieces are collected at the cathode. Resist is left in place during electropolishing, to protect the sidewalls from becoming pitted. Figure 4.18 illustrates the structure after electropolishing and removing of the resist. Notice that the capacitance gaps are completely reopened.

This technique to achieve uniform height was performed on the entire wafer, which made not only the ground planes and signal lines at the coupler's ports even in height, but also both plates of the tall vertical capacitors.

A problem that was encountered during testing as a result of polishing was that some of the metal that was smeared during mechanical polishing became lodged into the structures capacitance gaps. This made these structures un-testable since the metal in the gaps causes the signal lines and ground planes to be shorted together. Another issue with polishing is that polishing reduces the height of the structure. This means that the structure would have to be electroplated greater than its required height, in order to compensate for the metal that will be removed during the polishing process.

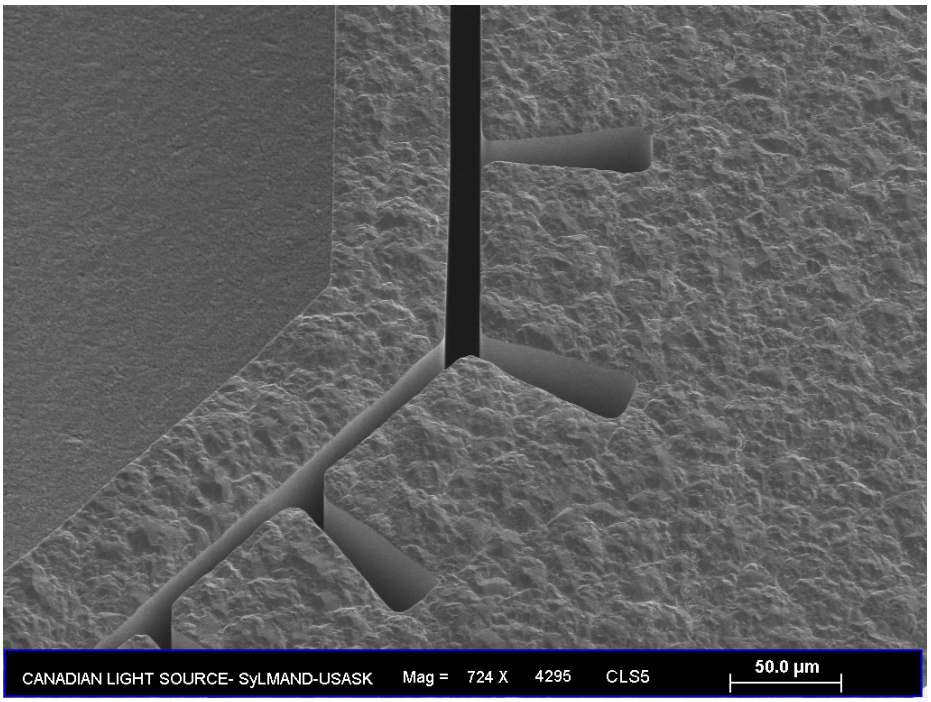

Figure 4.16: Unpolished Electroplated Structure with Uneven Height and Bumps

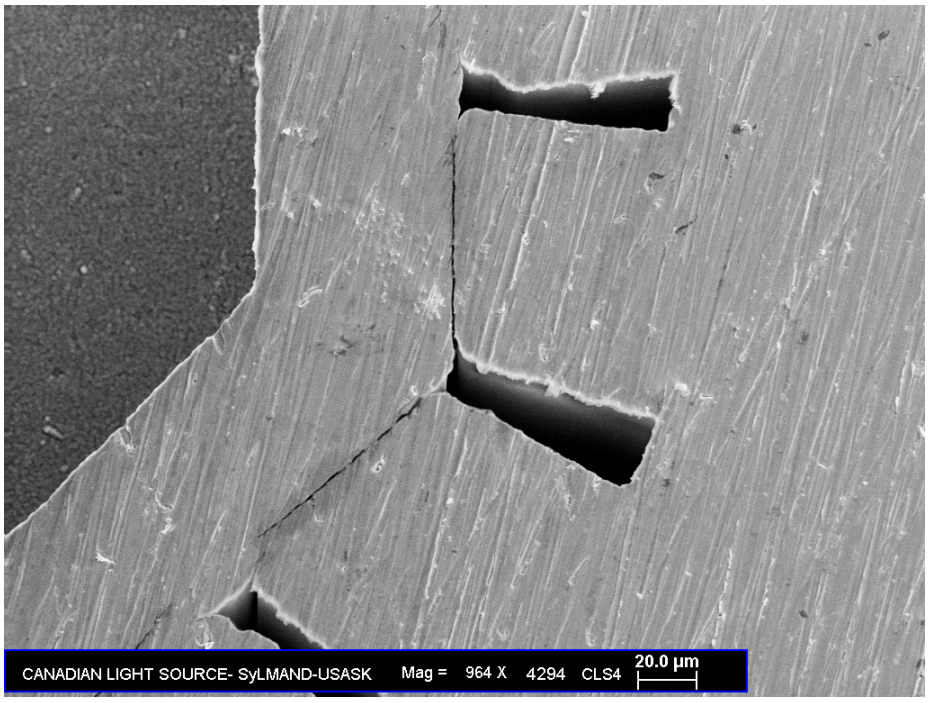

Figure 4.17: Mechanically Polished Structure which Illustrates a Thin Layer of Metal Smearing

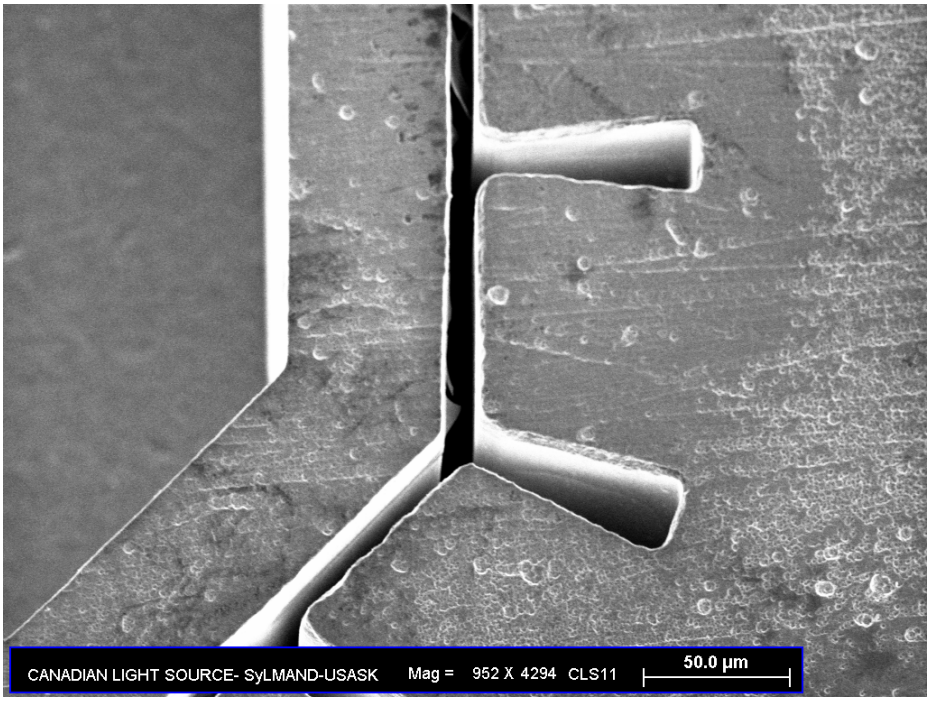

Figure 4.18: Electropolished Structure which shows a much Smoother Surface Compared to the Unpolished Structure and Reopened Capacitance Gaps after Metal Smearing

4.5 Testing Results of the Fabricated Couplers

The testing results of the fabricated coupler are presented in this section. There were five different styles of couplers tested. The differences between coupler styles were either a different layout or a different substrate. A description of each coupler is provided along with the performance results of the coupler in Sections 4.5.1 to 4.5.5. Appendix C provides the layouts of mask 1 and 2, with the location of each coupler labeled 1 through 12 for mask 1, and 1 through 17 for mask 2.

4.5.1 Coupler 1 - Compensated Capacitance Coupler on Alumina (Mask 1)

The first coupler tested was the microstructure coupler with compensated capacitance on alumina substrate (wafer 4295, location 1 of mask 1 layout). This coupler had extra capacitance to compensate for the capacitance lost from triangular shaped voids by increasing the length of the capacitors. This coupler was fabricated using Mask 1 which had the extra wide gaps. The height of the coupler was electroplated higher than the design height of 220 µm to try to add in the capacitance that was lost due to the wider gaps. The

metal height of this coupler varied between approximately 240 µm to 270 µm. An SEM image of Coupler 1 is shown in Figure 4.2 and its layout is shown in Figure 4.1 (b).

The measured performance results of Coupler 1 are shown in Figure 4.19 to Figure 4.21. Since the fabricated structure had larger capacitance gaps, and higher height than the original design shown in Chapter 3, a new HFSS simulation was performed to more closely match the fabricated structure using measured average heights and gap widths. The HFSS simulated structure had a height of 265 µm, capacitance gap width of 11.5 µm and a substrate with ε_r = 9.8 instead of 9.4, since for the alumina ceramic substrate that was used for fabrication 9.8 is a more accurate value. The HFSS simulation results are shown in Figure 4.19 to Figure 4.21 for comparison with the measured results.

The measured and simulated results of return loss ($|S_{11}|$) and through output ($|S_{21}|$) are shown in Figure 4.19. Figure 4.20 shows the measured and simulated isolation ($|S_{41}|$) and coupled output ($|S_{31}|$). The measured and simulated phase difference between the output ports of the coupler is shown in Figure 4.21.

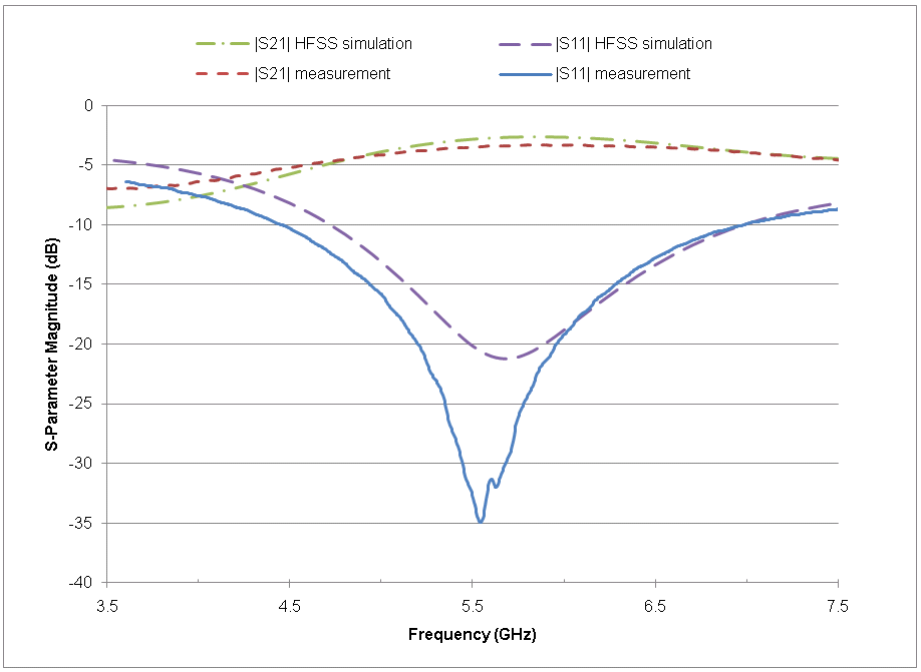

Figure 4.19: Measured $|S_{11}|$ and $|S_{21}|$ of Coupler 1

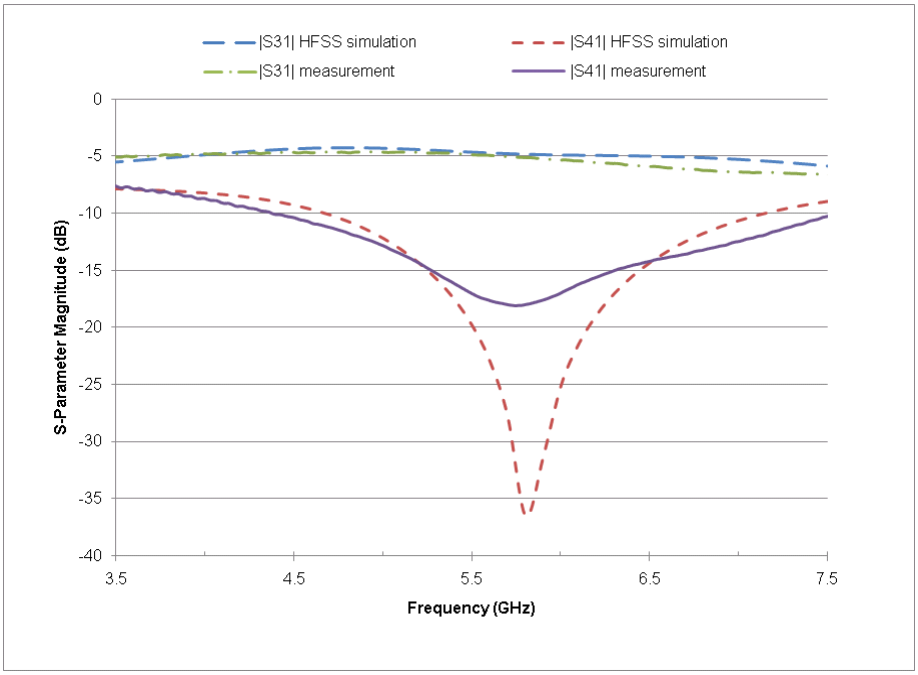

Figure 4.20: Measured $|S_{31}|$ and $|S_{41}|$ of Coupler 1

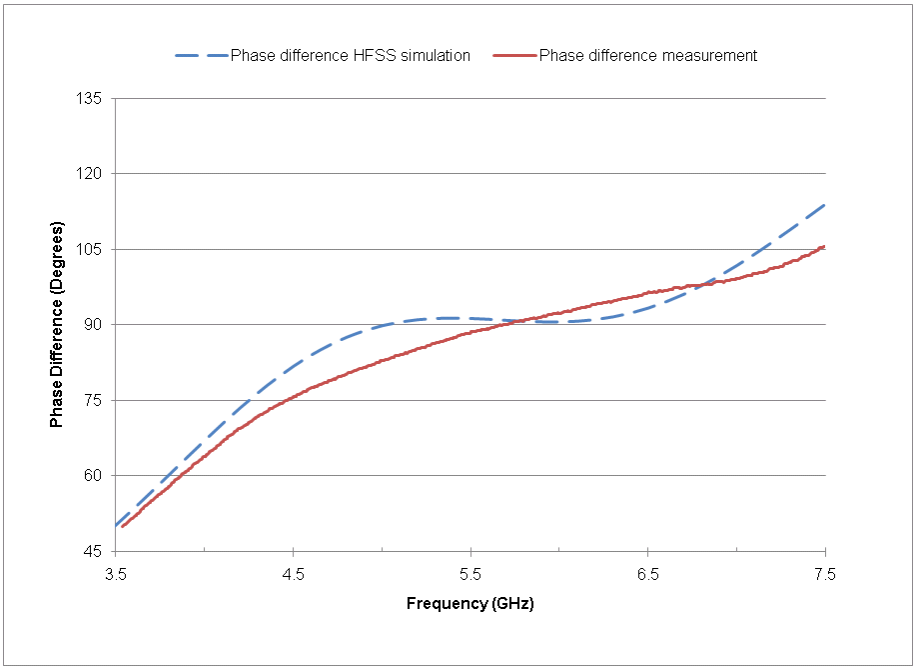

Figure 4.21: Measured Phase Difference Between the Output Ports of Coupler 1

4.5.2 Coupler 2 - Non-Compensated Capacitance Coupler on Alumina (Mask 2)

The layout for the non-compensated capacitance microstructure coupler is provided in Figure 4.1 (a) and the SEM image of this coupler design is shown in Figure 4.22.

Coupler 2 was fabricated on alumina substrate (wafer 4393, location 2 of mask 2 layout) and had approximately 5.9 µm gaps and an average height of 219 µm. The measured and HFSS simulation results of the coupler with a height of 220 µm with gap sizes of 6 µm is shown in Figure 4.23 to Figure 4.25 for comparison.

The measured and simulated results of return loss ($|S_{11}|$) and through output ($|S_{21}|$) are shown in Figure 4.23. Figure 4.24 shows the measured and simulated isolation ($|S_{41}|$) and coupled output ($|S_{31}|$). The measured and simulated phase difference between the output ports of the coupler is shown in Figure 4.25.

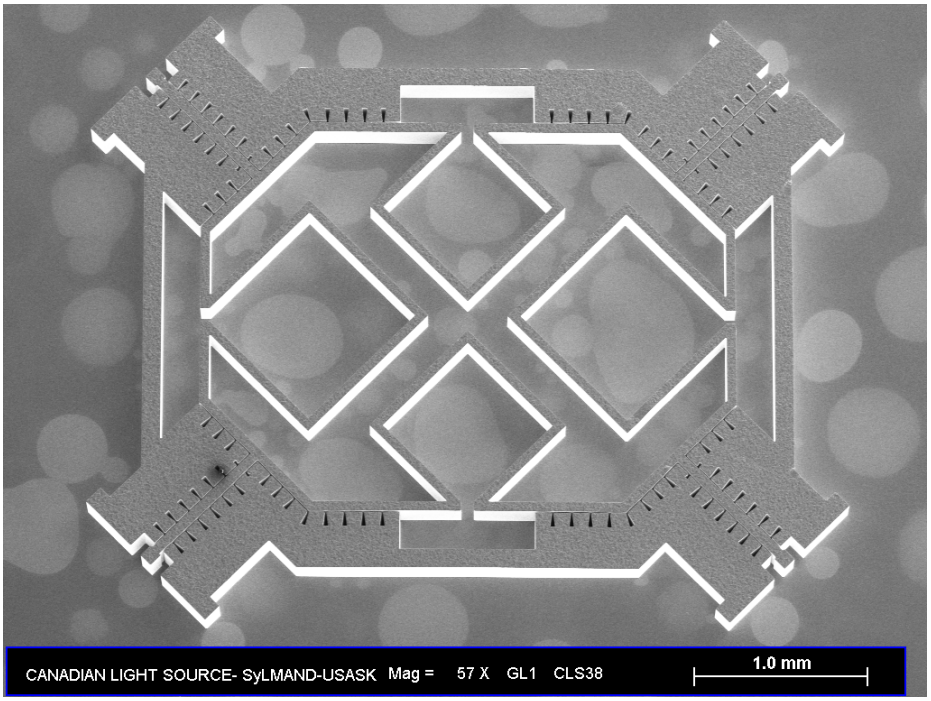

Figure 4.22: SEM Image of a Non-Compensated Microstructure Coupler

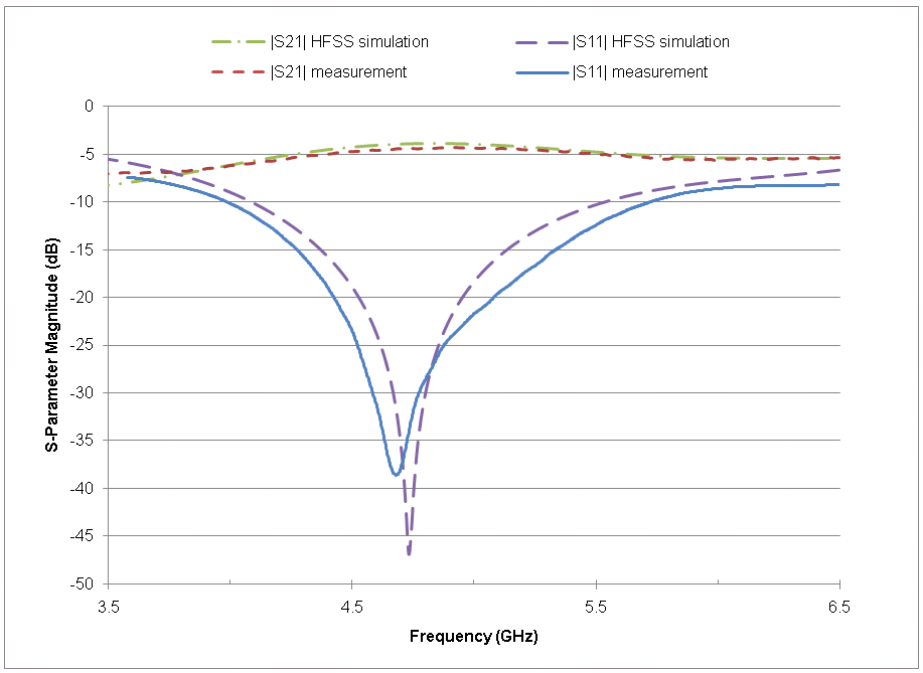

Figure 4.23: Measured $|S_{11}|$ and $|S_{21}|$ of Coupler 2

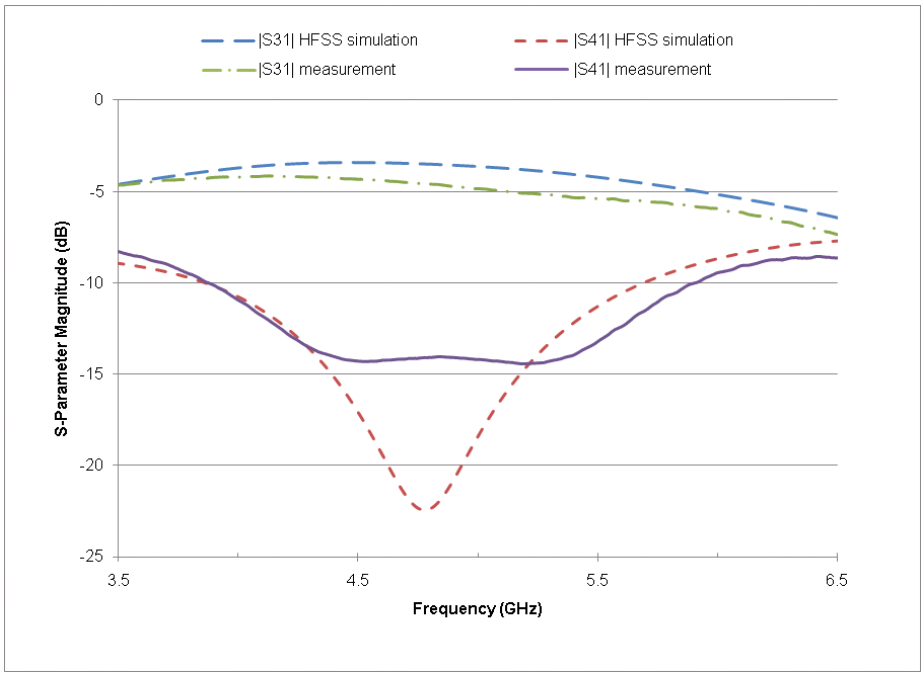

Figure 4.24: Measured $|S_{31}|$ and $|S_{41}|$ of Coupler 2

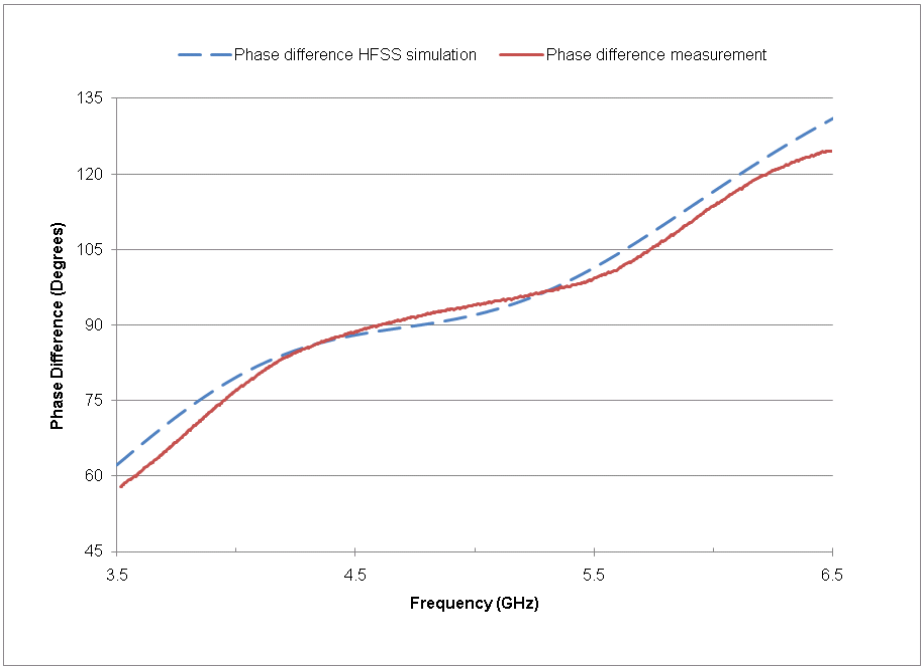

Figure 4.25: Measured Phase Difference Between the Output Ports of Coupler 2

4.5.3 Coupler 3 - Area Reduced Coupler on Alumina (Mask 2)

The layout of Coupler 3 is shown in Figure 4.1 (c). It is very similar to the layout shown in Figure 4.1 (a). The only difference between the two coupler layouts is that the spaces between the inductors have been reduced allowing for the layout of the Coupler 3 to be more compact. An image of Coupler 3 under test is shown in Figure 4.14.

Coupler 3 was fabricated with approximately 6.3 µm gaps and an average height of 276 µm on alumina substrate (wafer 4393, location 15 of mask 2 layout). The measured and HFSS simulation results of the area reduced coupler with a height of 275 µm with gap sizes of 6 µm is shown in Figure 4.26 to Figure 4.28 for comparison with the measured results.

The measured and simulated results of return loss ($|S_{11}|$) and through output ($|S_{21}|$) are shown in Figure 4.26. Figure 4.27 shows the measured and simulated isolation ($|S_{41}|$) and coupled output ($|S_{31}|$). The measured and simulated phase difference between the output ports of the coupler is shown in Figure 4.28.

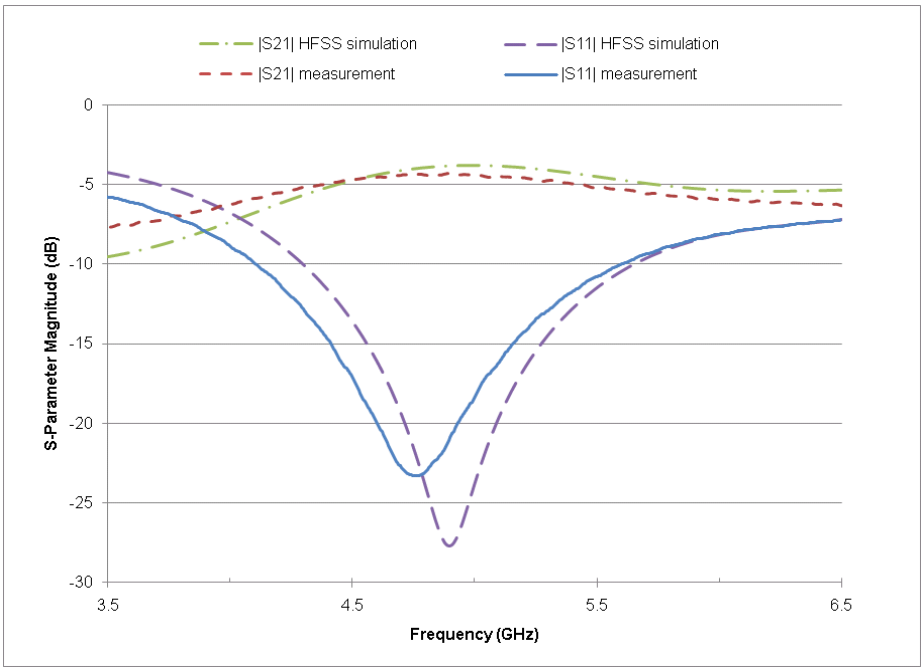

Figure 4.26: Measured $|S_{11}|$ and $|S_{21}|$ of Coupler 3

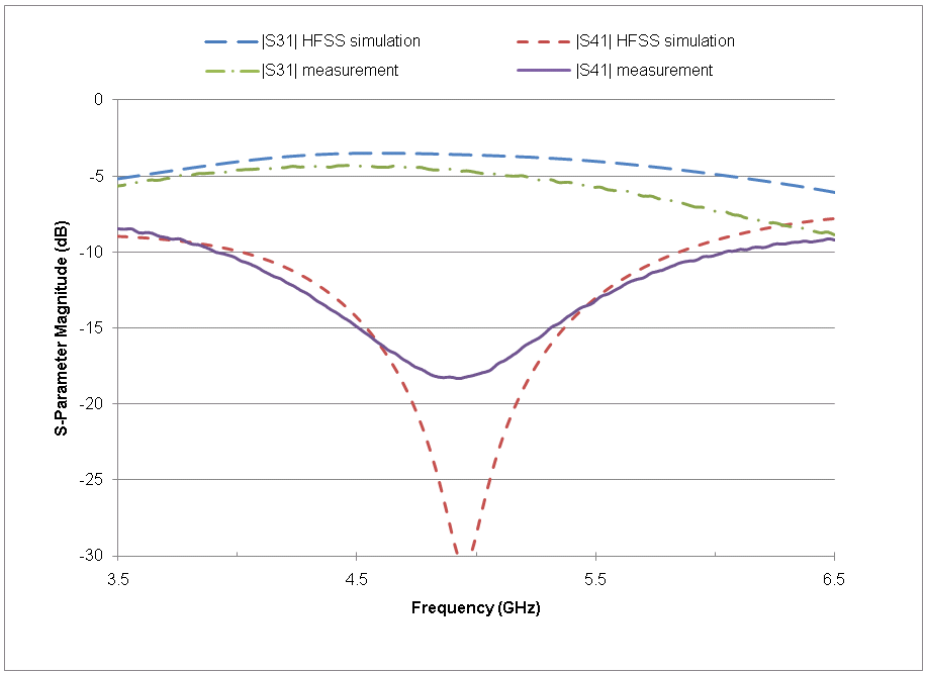

Figure 4.27: Measured $|S_{31}|$ and $|S_{41}|$ of Coupler 3

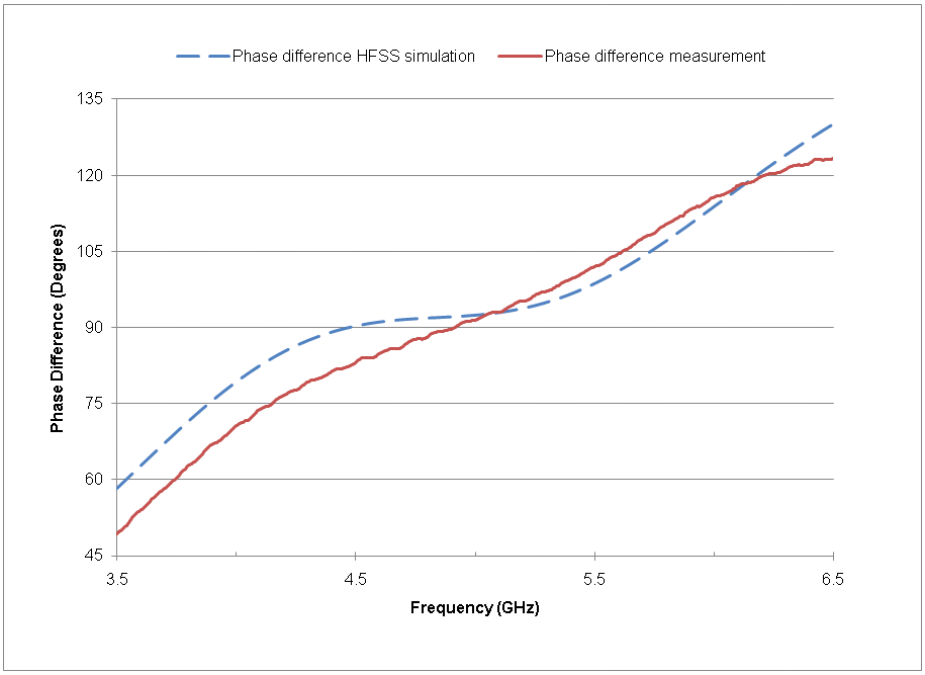

Figure 4.28: Measured Phase Difference Between the Output Ports of Coupler 3

4.5.4 Coupler 4 - Non-Compensated Capacitance Coupler on Quartz Glass (Mask 2)

The layout of Coupler 4 is provided in Figure 4.1 (a) and a SEM of this design of coupler is shown in Figure 4.22. The only difference between Coupler 4 and Coupler 2 is that Coupler 4 has a quartz glass substrate, instead of alumina. Coupler 4 was fabricated on wafer GL2. In reference to the layout of mask 2, this coupler was in location 4.

The structure of Coupler 4 had approximately 6.1 µm gaps and an average height of 250.4 µm. The measured and HFSS simulation results of this style of coupler with a height of 250 µm with gap sizes of 6 µm is shown in Figure 4.29 to Figure 4.31 for comparison.

The measured and simulated results of return loss ($|S_{11}|$) and through output ($|S_{21}|$) are shown in Figure 4.29. Figure 4.30 shows the measured and simulated isolation ($|S_{41}|$) and coupled output ($|S_{31}|$). The measured and simulated phase difference between the output ports of the coupler is shown in Figure 4.31.

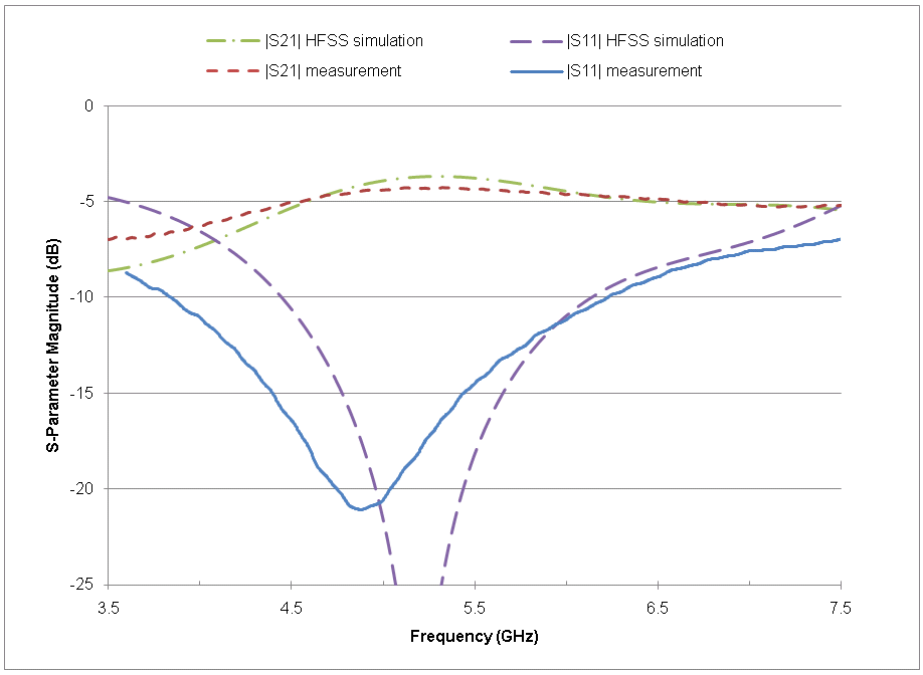

Figure 4.29: Measured $|S_{11}|$ and $|S_{21}|$ of Coupler 4

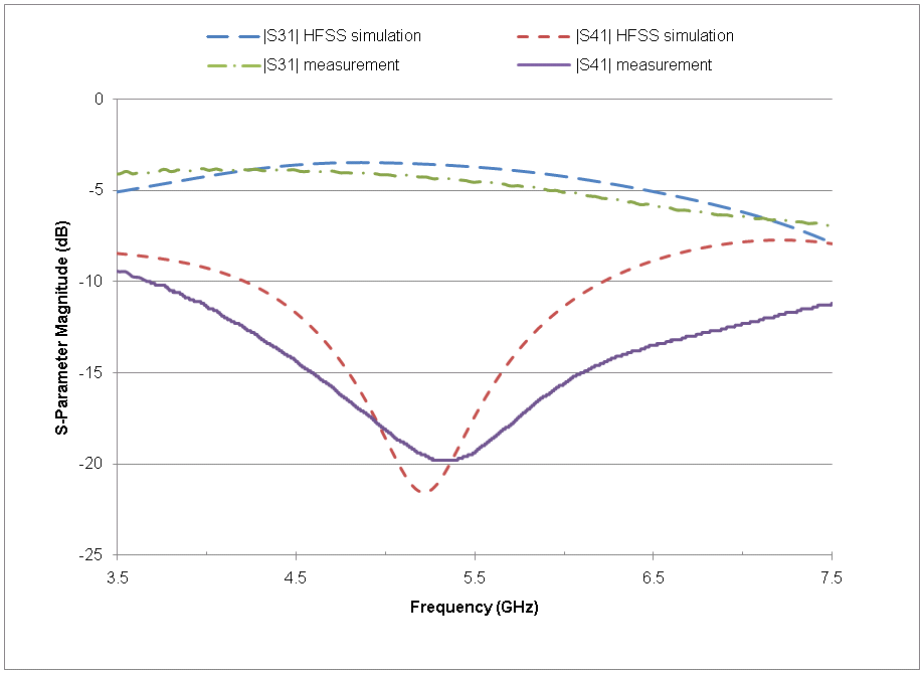

Figure 4.30: Measured $|S_{31}|$ and $|S_{41}|$ of Coupler 4

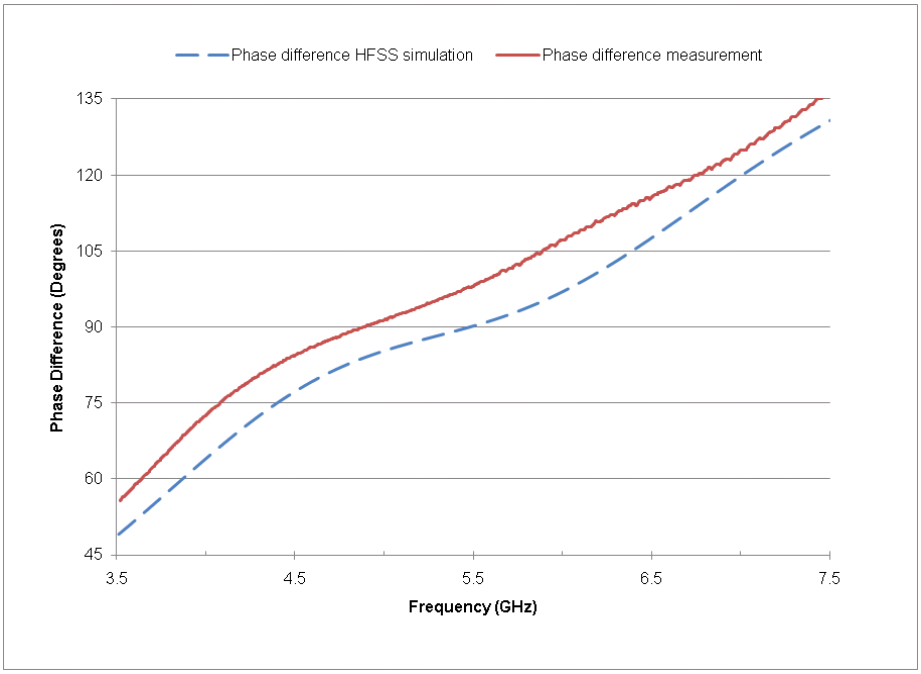

Figure 4.31: Measured Phase Difference Between the Output Ports of Coupler 4

4.5.5 Coupler 5 - Ring Coupler on Quartz Glass (Mask 2)

Coupler 5 is a microstructure ring coupler (wafer GL2, location 11 of mask 2 layout). The layout for this coupler is shown in Figure 4.1 (d) and a SEM image of a microstructure ring coupler is shown in Figure 4.32. Coupler 5 was fabricated on quartz glass substrate and had approximately 6.0 µm gaps and an average height of 300.1 µm. The measured and HFSS simulation results of the ring coupler design with a height of 300 µm with gap sizes of 6 µm is shown in Figure 4.33 to Figure 4.36 for comparison.

The measured and simulated results of return loss ($|S_{11}|$) and through output ($|S_{21}|$) are shown in Figure 4.33. Figure 4.34 shows the measured and simulated isolation ($|S_{41}|$) and coupled output ($|S_{31}|$). The measured and simulated phase difference between the output ports of the coupler is shown in Figure 4.35, and Figure 4.36.

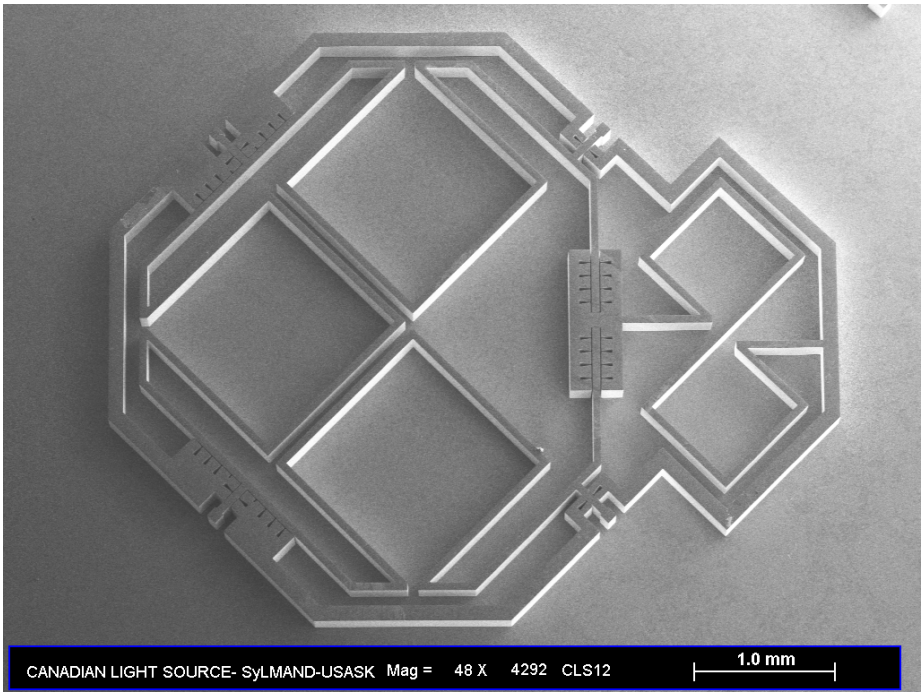

Figure 4.32: SEM image of a Microstructure Ring Coupler

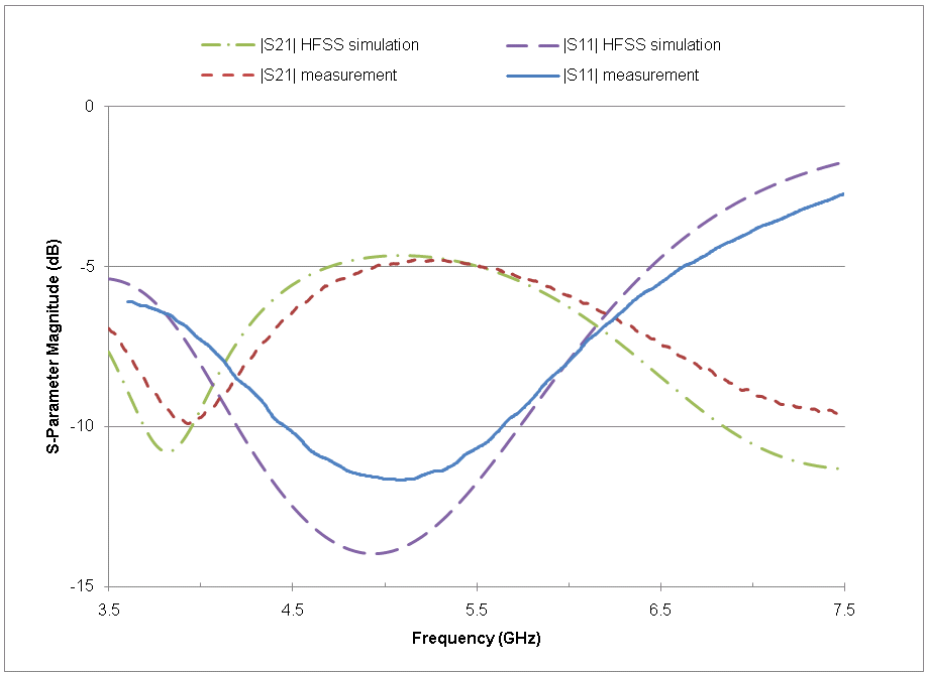

Figure 4.33: Measured $|S_{11}|$ and $|S_{21}|$ of Coupler 5

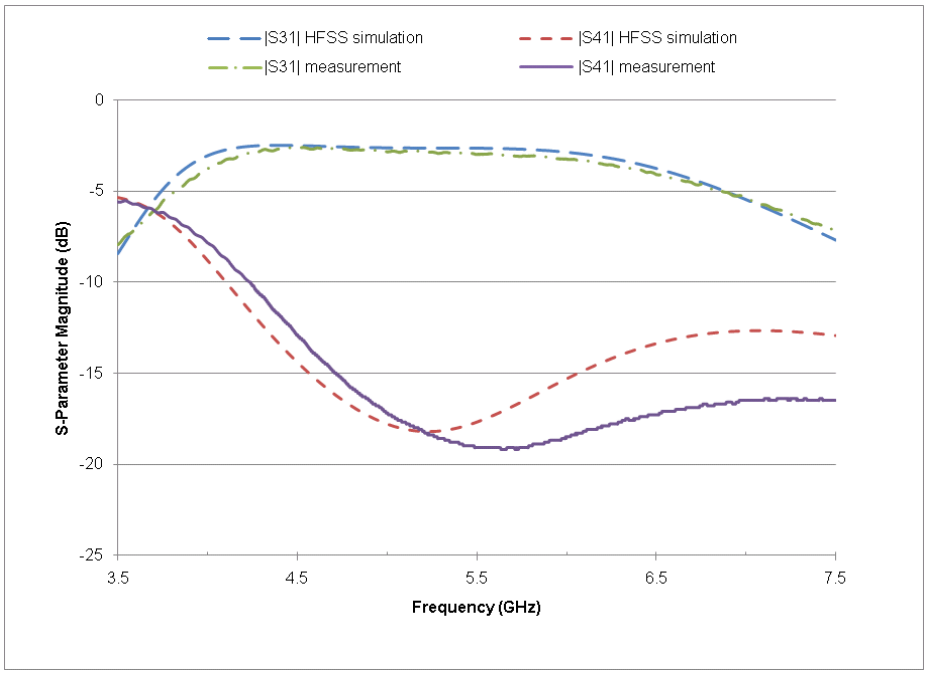

Figure 4.34: Measured $|S_{31}|$ and $|S_{41}|$ of Coupler 5

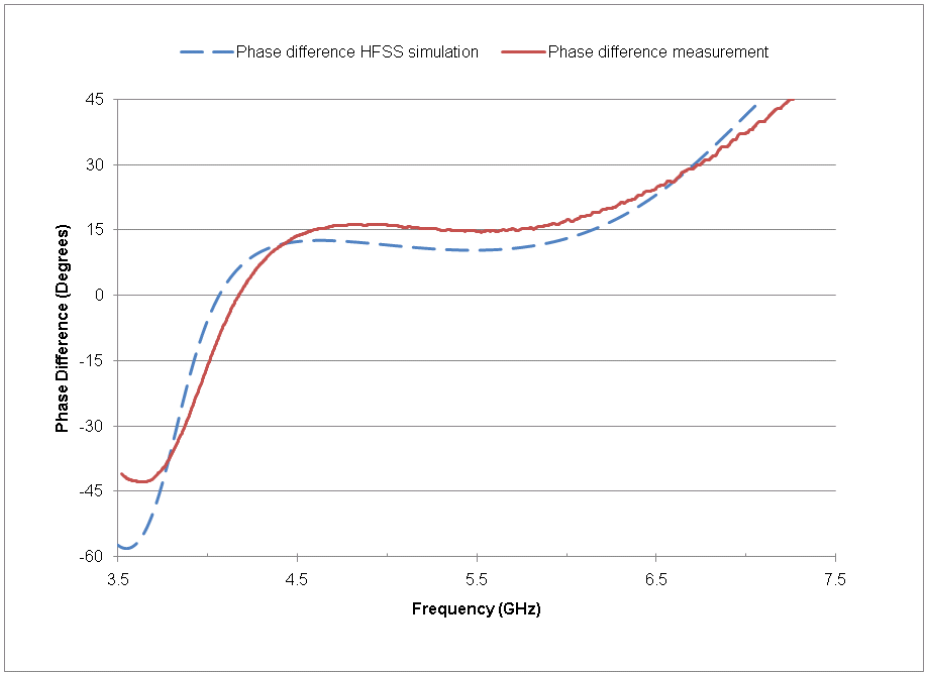

Figure 4.35: Measured 0° Phase Difference Between the Output Ports of Coupler 5 when Port 1 is the Input Port

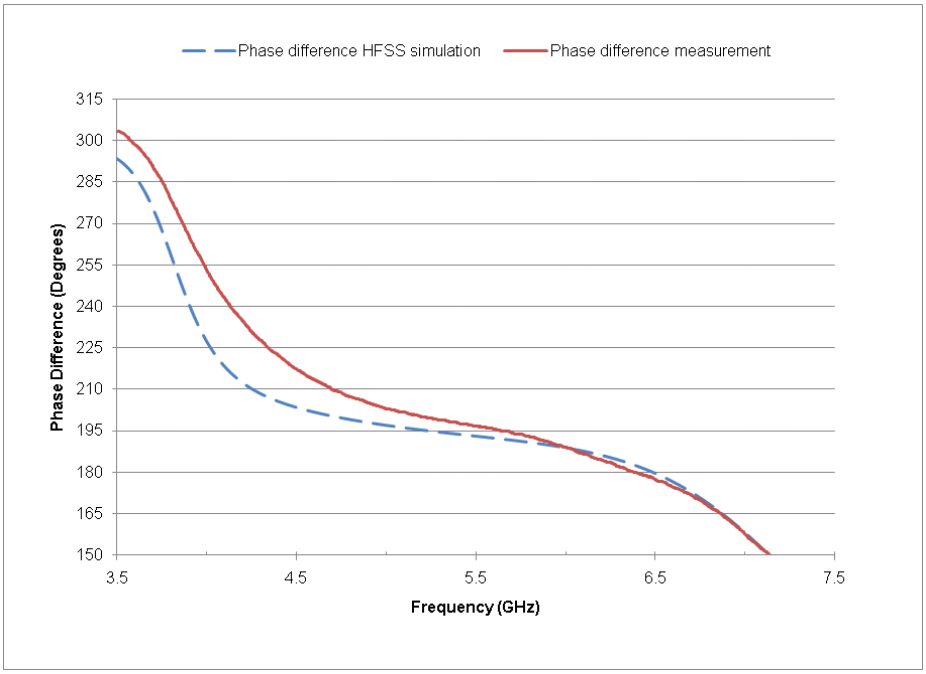

Figure 4.36: Measured 180° Phase Difference Between the Output Ports of Coupler 5 when Port 4 is the Input Port

4.6 Discussion of the Testing Results

A discussion of the testing results of Coupler 1 through 5 in comparison to simulation results is provided in this section. A description of each of the coupler structures was provided in the previous section.

4.6.1 Coupler 1 – Compensated Capacitance Coupler on Alumina

The measured performance results of the compensated capacitance microstructure branch-line coupler were comparable to the simulation results. Table 4.1 provides a summary of the measured performance results of Coupler 1. The simulation results of the 265 µm tall nickel structure of the same layout with a capacitance gap width of 11.5 µm and a substrate with a relative permittivity of 9.8 are also provided for comparison.

The measured operating frequency of Coupler 1 was 5.6 GHz and the simulated operating frequency was 5.7 GHz. The microstructure coupler had $|S_{21}|$ equal to -3.35 dB and $|S_{31}|$ equal to -4.88 dB at the operating frequency. The loss experienced in $|S_{31}|$ is most likely due to the structure having too much capacitance, since the extended metal over compensated for the capacitance lost from the triangular shaped voids, and contact issues with the microprobes on port 3 of the coupler, since this port had the largest height difference of 9 µm

between the ground planes and the signal line. At 5.7 GHz the simulated structure had $|S_{21}|$ equal to -2.70 dB and $|S_{31}|$ equal to -4.88 dB, which also shows that the output of port 3 has more loss than the output of port 2, so it is likely that the over-compensation of capacitance in the structural design is causing the loss.

The 3-dB bandwidth of the microstructure coupler was measured to be 85.2%. The 3-dB bandwidth was determined by finding the minimum span of frequency where $|S_{21}|$ and $|S_{31}|$ were within 3 dB of their value at the 5.6 GHz, the operating frequency. Since $|S_{21}|$ and $|S_{31}|$ do not overlap over a large frequency span, the lower frequency limit of the bandwidth calculation was from when $|S_{21}|$ reached -6.35 dB, which is 3 dB below the value of $|S_{21}|$ at the operating frequency, and the upper frequency limit was from when $|S_{31}|$ reached -7.88 dB, which is 3 dB below the value of $|S_{31}|$ at the operating frequency. The 3-dB bandwidth of the simulated structure was calculated using the same criteria and was found to be 68.4%.

The measured isolation and phase bandwidths of the microstructure coupler were smaller than the bandwidths found from simulation results. The decrease in these two bandwidths is a trade off for having an increased 3-dB bandwidth. The measured result of the isolation bandwidth was 18.3% is only slightly smaller than the simulated isolation bandwidth which was 21.1%. The measured ±5° phase bandwidth was 19.2% and the simulated result was 35.1%. The measured phase difference between port 2 and port 3 of the microstructure coupler at the operating frequency was found to be 89.0°, which is very close to the designed phase difference of 90.0°.

Overall, the measured results of the capacitance compensated microstructure branch-line coupler prove that the structure is functioning as a coupler. There is just more loss found in the measured results, which is most likely due to poor contact of the micro-probes on the rough, uneven metal height of the coupler structures ports.

Table 4.1: Summary of Performance for Coupler 1

Coupler 1 Performance Comparison							
Type	Op. Freq (GHz)	3-dB BW (%)	S_{21} at Op. Freq. (dB)	S_{31} at Op. Freq. (dB)	Phase difference between S_{21} and S_{31} at Op. Freq.	Isolation BW (%)	Phase BW (%)
HFSS Microstructure with Capacitance Compensation	5.7	68.4	-2.70	-4.78	90.9°	21.1	35.1
Measured Microstructure with Capacitance Compensation	5.6	85.1	-3.35	-4.88	89.0°	18.3	19.2

4.6.2 Coupler 2 – Non-Compensated Capacitance Coupler on Alumina

The measured performance results of Coupler 2 were compared to the simulation results of the 220 μm tall nickel structure of the same layout as Coupler 2 (without the triangular shaped voids), with a capacitance gap width of 6 μm and a substrate with a relative permittivity of 9.8. Table 4.2 provides a summary of the measured performance results of Coupler 2 and the structural simulation results.

The operating frequency of Coupler 2 was measured to be 4.75 GHz which is very comparable to the operating frequency of 4.76 GHz found from the HFSS structural simulation. The power division between the output ports at the operating frequency was almost even, but showed that the output signals were experiencing loss compared to simulation results. The $|S_{21}|$ was measured to be -4.44 dB and $|S_{31}|$ equal to -4.57 dB. The simulated values of $|S_{21}|$ and $|S_{31}|$ were -3.89 dB and -3.47 dB at the operating frequency. The loss of signal is most likely due to a poor connection between a port and probe which is caused from the structures signal and ground planes being uneven heights.

The 3-dB bandwidth of Coupler 2 was slightly larger than the simulated 3-dB bandwidth of 68.9%, with a value of 75.9%. The measured return loss bandwidth of Coupler 2 was 38.8% and was slightly larger than its simulated value of 32.4%. Unfortunately, the measured values of isolation ($|S_{41}|$) only reached below -14 dB, and not below the -15 dB isolation bandwidth criteria over the tested frequency span, so no valid isolation bandwidth was calculated for Coupler 2. The ±5° phase bandwidth and the phase difference between the coupler's output ports were very comparable to simulation. The ±5° phase bandwidth

was simulated to be 20.2% and measured to be 19.4%, and the phase difference between the coupler's outputs was simulated to be 90.0° measured to be 91.9°.

Overall, with the exception of the isolation bandwidth results, Coupler 2 had comparable performance to simulation results. The poor isolation results are likely due to the signal line of port 4 becoming detached from the substrate and sliding into the ground plane when making contact with the probe. This began occurring during the isolation measurement (which was the last coupler measurement), and continued to occur during repeat isolation measurement attempts.

Table 4.2: Summary of Performance for Coupler 2

Coupler 2 Performance Comparison							
Type	Op. Freq (GHz)	3-dB BW (%)	S_{21} at Op. Freq. (dB)	S_{31} at Op. Freq. (dB)	Phase difference between S_{21} and S_{31} at Op. Freq.	Isolation BW (%)	Phase BW (%)
HFSS Coupler 2 Structure	4.76	68.9	-3.89	-3.47	90.0°	16.6	20.2
Measured Coupler 2 Results	4.75	75.9	-4.44	-4.57	91.9°	N/A	19.4

4.6.3 Coupler 3 – Area Reduced Coupler on Alumina

The measured performance results of Coupler 3 were compared to the simulation results of a 275 μm tall nickel structure of the same layout as Coupler 3 (without the triangular shaped voids), with a capacitance gap width of 6 μm and a substrate with a relative permittivity of 9.8. Table 4.3 provides a summary of the measured performance results of Coupler 3 along with the structural simulation results for comparison.

The operating frequency of Coupler 3 was measured to be 4.89 GHz which is only 60 MHz lower than the operating frequency of 4.95 GHz found from the structural simulation.

At the operating frequency, the power division between the output ports of Coupler 3 was quite even, but showed that the output signals were experiencing loss compared to simulation results. The $|S_{21}|$ was measured to be -4.32 dB and $|S_{31}|$ equal to -4.56 dB. The simulated values of $|S_{21}|$ and $|S_{31}|$ were -3.75 dB and -3.58 dB at the operating frequency. The loss of signal is most likely attributed to a poor connection between a port and probe which is caused from the signal and ground planes of the structure being slightly uneven heights or from interference between the magnetic fields of the closely placed inductors in this design.

The 3-dB bandwidth of Coupler 3 was slightly smaller than the simulated 3-dB bandwidth of 51.9%, with a value of 48.8%. The measured return loss bandwidth of Coupler 3 is slightly larger than the simulated return loss bandwidth of 29.3% with a value of 33.8%. The measured and simulated isolation bandwidths were considered to be equal in value with a measured result of 16.5% and a simulated result of 16.4%. The phase difference between the coupler's output ports at the operating frequency was slightly lower than simulation with a measured value of 89.5° and a simulated value of 92.2°. The ±5° phase bandwidth was lower than the simulation results. The measured ±5° phase bandwidth was 11.7% and the simulated ±5° phase bandwidth was 23.0%.

Overall, the performance of Coupler 3 illustrated that the reduced area microstructure coupler design also behaves as a coupler with the main differences from simulation being a slightly smaller 3-dB bandwidth and smaller phase bandwidth. Again the differences between measured and simulation results are likely due to poor contact between the structure and the microprobes, and also from the inductors' magnetic field's interfering which each other (due to the inductors being placed so close together to minimize the overall coupler size).

Table 4.3: Summary of Performance for Coupler 3

Coupler 3 Performance Comparison							
Type	Op. Freq (GHz)	3-dB BW (%)	S_{21} at Op. Freq. (dB)	S_{31} at Op. Freq. (dB)	Phase difference between S_{21} and S_{31} at Op. Freq.	Isolation BW (%)	Phase BW (%)
HFSS Coupler 3 Structure	4.95	51.9	-3.75	-3.58	92.2°	16.4	23.0
Measured Coupler 3 Results	4.89	48.8	-4.32	-4.56	89.5°	16.5	11.7

4.6.4 Coupler 4 – Non-Compensated Capacitance Coupler on Quartz Glass

The measured performance results of Coupler 4 were compared to the simulation results of the 250 μm tall nickel structure of the same layout as Coupler 4 (without the triangular shaped voids), with a capacitance gap width of 6 μm and a substrate with a relative permittivity of 3.78. Table 4.4 provides a summary of the measured and simulated performance results.

The operating frequency of Coupler 4 is slightly higher than the simulated operating frequency of 5.21 GHz and was measured to be 5.30 GHz. Coupler 4 shows an increase in operating frequency of approximately 590 MHz in comparison to Coupler 2, which is the same design as Coupler 4 but on alumina substrate. This frequency shift shows that although the microstructure couplers were designed as lumped element couplers, the structures still have distributed effects due to being a finite size. The increase in operating frequency between Coupler 4 and Coupler 2 is due to the relative permittivity of quartz glass being lower than the relative permittivity of alumina, and as shown in Equation 2.10, the operating frequency of a distributed element is inversely proportional to the square root of relative permittivity.

The power division between the output ports of Coupler 4 at the operating frequency is considered to be equal. The measured values of $|S_{21}|$ and $|S_{31}|$ were measured to be -4.32 dB and -4.34 dB. The simulated values of $|S_{21}|$ and $|S_{31}|$ were -3.73 dB and -3.54 dB at the operating frequency. The loss shown between the measured and simulated results is most likely attributed to a poor connection between a port and probe which is caused from the signal and ground planes of the structure being slightly uneven heights.

The 3-dB bandwidth of Coupler 4 was much larger than the simulated 3-dB bandwidth of 56.8%. The 3-dB bandwidth of Coupler 4 was measured to be better than 75.5%. The full 3-dB bandwidth of 95.7% was obtained by extrapolating the measured data since the calibrated frequency band used during the measurements of this coupler was too narrow. Repeat measurements of the 3-dB bandwidth were attempted with a wider frequency band. Unfortunately no useful data could be measured because the ends of the signal lines of port 2 and port 4 of the coupler both became detached from the substrate, and were causing shorting with the ground planes when the probes were placed on the port surface.

The measured isolation bandwidth was also larger than the isolation bandwidth found from simulation results. The isolation bandwidth was measured to be 28.8% and the simulated isolation bandwidth was 16.3%. The measured ±5° phase bandwidth of Coupler 4 was smaller than the simulated ±5° phase bandwidth. The ±5° phase bandwidth was simulated to be 19.8% and was measured to be 12.7%. The phase difference between the coupler's output ports at the operating frequency was also different from its simulation results, with a measured value of 95.8° and a simulated value of 90.0°. The differences

between simulated and measured results of the ±5° phase bandwidth and the value of the phase difference between the coupler's output ports are considered to be trade offs for having increased 3-dB and isolation bandwidths.

The return loss bandwidth of Coupler 4 was not calculated due to the minimum of $|S_{11}|$ being frequency shifted lower than the operating frequency and the measured data being very noisy. The noise was most likely due to the calibration effectiveness on the test set up decreasing, as the cables attached to the network analyzer and microprobes were repositioned so the probes could make contact with the coupler structure. The frequency shift shown in $|S_{11}|$ could be due to one of the loads on a port not making sufficient enough contact with the structure, causing impedance mismatch between the structure and the probe (a small amount of signal becomes reflected back into the port).

Overall, Coupler 4 had the best performance out of the tested branch-line microstructure couplers since the output signals experienced the least amount of loss and were basically equal, and this coupler also had largest 3-dB and isolation bandwidths. The results of Coupler 4 and Coupler 2 also demonstrated how the operating frequency of the microstructure coupler designs is affected by its substrate.

Table 4.4: Summary of Performance for Coupler 4

Coupler 4 Performance Comparison							
Type	Op. Freq (GHz)	3-dB BW (%)	S_{21} at Op. Freq. (dB)	S_{31} at Op. Freq. (dB)	Phase difference between S_{21} and S_{31} at Op. Freq.	Isolation BW (%)	Phase BW (%)
HFSS Coupler 4 Structure	5.21	56.8	-3.73	-3.54	90.0°	16.3	19.8
Measured Coupler 4 Results	5.30	> 75.5, extrapolated to be 95.7	-4.32	-4.34	95.8°	28.8	12.7

4.6.5 Coupler 5 – Ring Coupler on Quartz Glass

The measured performance results of Coupler 5 were compared to the simulation results of the 300 μm tall nickel structure of the same layout as Coupler 5 (without the triangular shaped voids), with a capacitance gap width of 6 μm and a substrate with a relative permittivity of 3.78. Table 4.5 provides a summary of the measured and simulated performance results.

The operating frequency of Coupler 5 is 5.23 GHz and is slightly higher than the operating frequency of 5.09 GHz found by simulation. The power division between the output ports of Coupler 5 is uneven but still comparable to the simulation results. The measured values of $|S_{21}|$ and $|S_{31}|$ were -4.84 dB and -2.89 dB. The simulated values of $|S_{21}|$ and $|S_{31}|$ were -4.67 dB and -2.63 dB at the operating frequency.

The measured 3-dB bandwidth of Coupler 5 is 44.9% and is slightly higher than the simulated value of 42.4%. As is the case for most lumped element ring couplers, the isolation bandwidth of Coupler 5 was not able to be calculated because the $|S_{41}|$ stayed below -15 dB at all frequencies above the operating frequency in the tested frequency span. The measured ±5° phase bandwidth of Coupler 5 was larger than the simulated ±5° phase bandwidth for the 0° case and smaller than the simulated ±5° phase bandwidth for 180° cases. For the 0° case the ±5° phase bandwidth was measured to be 36.7% and simulated to be 29.5%. For the 180° case the ±5° phase bandwidth was measured to be 14.1% and simulated to be 21.8%. The phase difference between the coupler's output ports at the operating frequency was higher than the simulation results for both cases. For the ideal 0° phase difference case, the measured phase difference was 15.3° and the simulated phase difference was 11.3°. For the ideal 180° phase difference case, the measured phase difference was 199.6° and the simulated phase difference was 196.3°. The return loss bandwidth of Coupler 4 was not calculated due to the measured data being very noisy.

The noise in the S_{11} signal, and the differences between simulated and measured results of the ±5° phase bandwidth and the value of the phase difference between the coupler's output ports, could be due to load mismatching caused by poor contact between one of the ports and a microprobe or due to the inductors being placed close together and their magnetic fields interfering with one another. Another explanation for the noise is due to the calibration effectiveness on the test set up decreasing, as the cables attached to the network analyzer and microprobes were repositioned so the probes could make contact with the appropriate ports of the coupler structure.

Overall, Coupler 5 had reasonably close performance to simulation with comparable operating frequency, 3-dB bandwidth, and $|S_{21}|$ and $|S_{31}|$ behavior. This coupler also successfully demonstrated that different phase differences between output ports were possible when the input port of the coupler was changed from port 1 to port 4.

Table 4.5: Summary of Performance for Coupler 5

Coupler 5 Performance Comparison							
Type	Op. Freq (GHz)	3-dB BW (%)	S_{21} at Op. Freq. (dB)	S_{31} at Op. Freq. (dB)	Phase difference between S_{21} and S_{31} at Op. Freq.	Isolation BW (%)	Phase BW (%)
HFSS Coupler 5 Structure	5.09	42.4	-4.67	-2.63	11.3°, 196.3°	29.3	29.5, 21.8
Measured Coupler 5 Results	5.23	44.9	-4.84	-2.89	15.3°, 199.6°	N/A	36.6, 14.1

CHAPTER 5
SUMMARY AND CONCLUSIONS

5.1 Summary

The purpose of this research was to design, fabricate, and test a high aspect ratio 3-dB microstructure coupler. D-XRL was to be used as the fabrication method and the coupler's area should be reduced compared to existing 3-dB distributed couplers. In Chapter 1, the main objectives of this research were outlined to be:

1) Review existing 3-dB coupler designs with a focus on distributed and lumped element designs. Compare the performance between the distributed and lumped element couplers and determine the values for a lumped element 3-dB coupler that will maximize the 3-dB bandwidth and still have acceptable return loss and isolation between the input and unused port at the centre frequency of the coupler.
2) Review the theory and design of high aspect ratio lumped element microstructures fabricated by D-XRL and the limitations of this fabrication process.
3) Design 3-dB microstructure couplers based on the lumped element designs (that achieve the greatest 3-dB bandwidth) and the high aspect ratio lumped element microstructures.
4) Fabricate sample microstructure couplers with D-XRL.
5) Test the microstructure couplers and compare their performance with simulation results.

Throughout this work, all of the research objectives were achieved. The first objective was realized by performing a literature review on existing 3-dB coupler designs. A method found to reduce the area of a distributed coupler was to replace single or multiple transmission lines of the coupler with lumped element equivalent circuits. High aspect ratio microstructure lumped elements were chosen as the lumped element style since they have a high Q factor at the coupler's design frequency of 5.4 GHz. The coupler designs that were

further investigated were the 3-dB branch-line coupler and the 3-dB rat-race coupler. Although the Lange and interdigitated coupler designs also provide equal coupling, they were not further pursued because of the requirement for jumper wires in their design. Connecting jumper wires to a high aspect ratio microstructure would have created additional challenges for fabrication and testing. The jumper wires would have also introduced unwanted inductance and losses into the circuit.

To compare the performance of lumped element and distributed couplers the ideal S-parameter equations of both coupler styles were derived and plotted, as well as compared by simulations. Since the performance of the two coupler styles were considered to be equivalent at the centre frequency, the capacitor and inductor values of the lumped element coupler were varied through optimization simulations to determine the values that would increase the 3-dB bandwidth.

Next the existing microstructure lumped elements were reviewed. Based on the existing lumped element microstructure designs and the lumped element values that provided the largest 3-dB bandwidth for the branch-line and ring couplers, the branch-line and rat-race microstructure couplers were designed and simulated using HFSS. The simulations verified that the microstructure couplers had comparable performance to their lumped element equivalents.

To fabricate the microstructure couplers a mask layout was designed to include four different coupler styles. Fabrication of the couplers using D-XRL was performed at IMT/KIT in Germany. Five different couplers, which had various designs and substrates were successfully tested. All couplers showed similar results to simulation. The coupler that had the overall best performance was Coupler 4. Coupler 4 was designed to be an equivalent to a 3-dB branch-line coupler and was fabricated on quartz glass substrate. Coupler 4 was 85% smaller than its distributed equivalent coupler on quartz glass substrate. At the centre frequency of 5.3 GHz the through and coupled values of this coupler's outputs were measured to be -4.32 dB and -4.44 dB. The 3-dB bandwidth of the coupler was measured to be better than 75.5% and extrapolated to be approximately 95%. The isolation bandwidth of the coupler was measured to be 28.8%. The phase difference between the output ports of Coupler 4 was designed to be 90.0° and was measured to be 95.8°. The ±5° phase bandwidth was measured to be 12.7%. The differences between the measured and simulated results can

be attributed to mismatch occurring between one of the couplers ports and a probe, either caused from non-ideal contact between the probe and the port, or non-ideal loads. The differences could also be due to the fabricated coupler being non-uniform in height, which would slightly change the values of the capacitors.

5.2 Conclusions

The results of this research prove that 3-dB microstructure couplers can be implemented with high aspect ratio lumped elements, fabricated on a single metal layer with a single D-XRL exposure. The advantage of implementing the microstructure couplers with high aspect ratio lumped elements is that a significant reduction in area was achieved when compared with the area of distributed couplers. The area reduction of the microstructure branch-line and rat race couplers was 85% and 90% respectively, when compared with their equivalent distributed models on quartz glass substrate. The measured performance results of the microstructure coupler designs were comparable to structural simulations.

5.3 Future and Continuous Work

Recommended future work involved in the microstructure coupler project includes:

1) The fabrication of a polished microstructure coupler on quartz glass to facilitate easier testing and improve performance over devices fabricated on alumina since the microstructure will be electrically smaller on quartz glass substrate. Currently the fabrication procedure is experiencing adhesion problems between the titanium seed layer and the quartz glass substrate, making it to risky to attempt mechanical polishing. Also, the quartz glass substrate is very fragile compared to the alumina substrate and may not be able to handle the stress of mechanical polishing without cracking.
2) Determining a procedure to remove the metal flakes that often become lodged in the capacitance gaps of the coupler designs during polishing.
3) Designing microstructure couplers with different coupling coefficients and different phase outputs since RF applications require more than just 180° and quadrature 3-dB couplers.

4) Improving the performance of the microstructure ring coupler by modifying the structural design, so that the magnetic fields of the inductors do not interfere with one another.
5) Modifying the layout of the branch-line and rat-race microstructure couplers to improve the anchoring of the structure to the substrate, so that during the extended etching time required to remove the titanium layer from the structures small capacitance gaps the inductors and sections of the signal lines do not become over etched and detached from the substrate. Possible ways to improve the structures for etching are to increase the widths of the capacitance gaps, increase the widths of the signal lines, or to add large wide sections to act as anchors in areas of the signal line.
6) Develop a method to increase the roughness of the quartz glass substrate so that the titanium seed layer has a stronger adhesion to the glass surface and the electroplated coupler will be able to remain anchored to the substrate during polishing and testing.
7) Extending the microstructure coupler into a larger structure such as a Butler matrix, by connecting multiple microstructure couplers in cascade.
8) Designing a transmission line structure that is capable of connecting the microstructure couplers to planar circuitry, so that the microstructure couplers are essentially a black box that can be integrated with circuitry fabricated with more common techniques such as photolithography.

.

LIST OF REFERENCES

[1] I. Sakagami, K. Sakaguti, M. Fujii, M. Tahara, Y. Hao, "On a lumped element three-branch 3-dB coupler with Butterworth and Chebychev characteristics," *The 2004 47th Midwest Symposium on Circuits and Systems,* vol. 3, pp. 21-24, July 2004.

[2] R. Gomez-Garcia, J. I. Alonso, & D. Amor-Martin, "Using the branch-line directional coupler in the design of microwave bandpass filters," *IEEE Trans Microw. Theory Tech.*, vol. 53, no. 10, pp. 3221–3229, Oct. 2005.

[3] F. Ferrero and G. Jacquemod, "A tunable quasi-lumped microstrip coupler and RF applications," *Microwave Symposium, 2007., IEEE/MTT-S International,* pp. 1197-1200, Jun. 2007.

[4] M. Bona, L. Manholm, J. P. Satarski, B. Svensson, "Low-loss compact butler matrix for a microstrip antenna," *IEEE Trans. Microw.Theory Tech.*, vol. 50, no. 9, pp. 2069–2075, Sept. 2002.

[5] M. Nedil, T. A. Denidni, L. Talbi, "Novel butler matrix using CPW multilayer technology," *IEEE Trans. Microw. Theory Tech.,* vol. 54, no. 1, pp. 499-507, Jan. 2006.

[6] C.Y. Ho, "Design of lumped quadrature couplers," *Microwave Journal*, vol. 22, no. 9, pp. 67-70, Sept. 1979.

[7] D.T. Haluzan, D.M. Klymyshyn, "High-Q LIGA MEMS vertical capacitors for upper microwave frequencies", *Microwave & Optical Technology Letters,* vol. 42, no. 6, pp. 507-511, Sept. 2004.

[8] D.M. Klymyshyn, D.T. Haluzan, M. Börner, S. Achenbach, J. Mohr, T. Mappes, "High aspect ratio vertical cantilever RF-MEMS variable capacitor," *IEEE Microwave and Wireless Components Letters,* vol. 17, no. 2, pp. 127-129, Feb. 2007.

[9] E. Gono-Santosa, D.M. Klymyshyn, D. Haluzan, M. Börner, S. Achenbach, and J. Mohr, "RF MEMS inductors fabricated using deep x-ray lithography," *HARMST 2009,* Saskatoon, Canada, Jun. 2009.

[10] X. Yu, D. M. Klymyshyn, "Modeling and analysis of LIGA structural micromachinined inductors on CMOS/BiCMOS substrate," *Canadian Conference on Electrical and Computer Engineering, 2005.*, pp. 421 -424, May 2005.

[11] D.M. Pozar, *Microwave Engineering*. John Wiley and Sons, Inc., third ed., 2005.

[12] R.K. Mongia, I.J. Bahl, P. Bhartia, J. Hong, *RF and Microwave Coupled-Line Circuits.* Norwood, MA: Artech House, Inc., second ed., 2007.

[13] A. Kachayev, "LIGA-Micromachined Tight Microwave Couplers," M.Sc., University of Saskatchewan, Saskatoon, Saskatchewan, Fall 2003.

[14] S. Achenbach, "Optimization of the Process Conditions for the Fabrication of Microstructures by Ultra Deep X-ray Lithography (ULDXRL)," Ph.D., Wissenschaftliche Berichte, Forschungszentrum Karlsruhe, 2000.

[15] C.K. Malak, V. Saile, "Applications of LIGA technology to precision manufacturing of high-aspect-ratio micro-components and –systems: a review," *Microelectronics Journal*, vol. 35, no. 2, pp 131-143, Feb. 2004.

[16] J. Kouba, R. Engelke, M. Bednarzik, G. Ahrens, Heinz-Ulrich Scheunemann, G. Gruetzner, B. Loechel, H. Miller, D. Haase, "SU-8: promising resist for advanced direct LIGA applications for high aspect ratio mechanical microparts," *Microsystem Technologies,* vol. 13, no. 3, pp. 311-317, Feb. 2007.

[17] W. Menz, J. Mohr, and O. Paul, *Microsystem Technology*. Verlag GmbH: Wiley-vch, 2001.

[18] Samuel J. Parisi, "180° Lumped Element Hybrid," *Microwave Symposium Digest, 1989., IEEE MTT-S International*, vol. 3, pp.1243-1246, 13-15 Jun. 1989.

[19] Advanced Design System (ADS), Agilent Technologies, Palo Alto, CA, USA, Version 2006A and Version 2009.

[20] Agilent Technologies, ADS Overview website: http://www.home.agilent.com/agilent/product.jspx?nid=-34346.0.00&cc=US&lc=eng

[21] ADS 2009, Summary of Optimizations website: http://edocs.soco.agilent.com/display/ads2009/Summary+of+Optimizers

[22] D.T. Haluzan, "Microwave LIGA MEMS Variable Capacitors," M.Sc., University of Saskatchewan, Saskatoon, Saskatchewan, Fall 2004.

[23] S. Achenbach, D. Klymyshyn, D. Haluzan, T. Mappes, G. Wells, J. Mohr, "Fabrication of RF MEMS variable capacitors by deep X-ray lithography and electroplating," *Microsystem Technologies,* vol. 13, no. 3, pp. 343-347, Feb. 2007.

[24] X. Yu, "Modeling And Analysis Of Thick Suspended Deep X-ray LIGA Inductors On CMOS/BiCMOS Substrate," M.Sc., University of Saskatchewan, Saskatoon, Saskatchewan, Spring 2006.

[25] E. Gono-Santosa, D.M. Klymyshyn, M. Börner, D.T Haluzan, S. Achenbach, J. Mohr, "High-aspect-ratio RF low-pass filter fabricated using deep x-ray lithography," *HARMST 2009*, Saskatoon, Canada, Jun. 2009.

[26] D.M. Klymyshyn, M. Börner, D.T. Haluzan, E.G. Santosa, M. Schaffer, S. Achenbach, J. Mohr, "Vertical High-*Q* RF-MEMS Devices for Reactive Lumped Element Circuits," *IEEE Trans. Microw. Theory Tech.,* vol. 58, no. 11, pp. 2976-2986, Nov. 2010.

[27] Ansoft High Frequency Structure Simulator (HFSS™), Ansoft Corporation, Pittsburgh, PA, USA, Version 10.1.3.

[28] Ansoft High Frequency Structure Simulator v10 User's Guide, Ansoft Corperation, Pittsburgh, PA, USA, Jun. 2005.

[29] S. Lucyszyn, "Microwave characterization of nickel," *PIERS Online Journal,* vol. 4, no. 6, pp. 686-690, Jun. 2008.

[30] S. Graham, J. Kelley, N. Yang, T. Borca-Tasciuc, "The role of microstructure in the electrical and thermal conductivity of Ni-alloys for LIGA microsystems," *Microsystems Technologies*, vol. 10, no. 6, pp. 510-516, Oct. 2004.

[31] H. M. Greenhouse, "Design of planar rectangular microelectronic inductors," *Parts, Hybrids, and Packaging, IEEE Transactions on,* vol. 10, no. 2, pp. 101-109, Jun. 1974.

[32] A. Ruzzu, B. Matthis, "Swelling of PMMA-structures in aqueous solutions and room temperature Ni-electroforming," *Microsystem Technologies*, vol. 8, no. 2, pp.116-119, May 2002.

[33] S. Kissling, K. Bade, M. Börner, D.M. Klymyshyn, "Electropolishing as a method for deburring high aspect ratio nickel RF MEMS," *Microsystem Technologies*, vol. 16, no. 8, pp. 1361-1367, Aug. 2010.

APPENDIX A
S-PARAMETER EQUATIONS FOR DISTRIBUTED COUPLERS

A.1 S-Parameter Equations for the Distributed Branch-line Coupler

The even and odd mode analysis and the S-Parameter equations for the Branch-line Coupler are provided in this section. Maple V Release 5 was used for simplification of the analysis and equations. The definitions of the symbols used in the equations are provided below.

$A = \frac{\pi f}{2 f_0}$, where f is the frequency, and f_0 is the couplers centre frequency

I imaginary number, commonly known as j or i

ABCDocs: ABCD parameters of a $\frac{\lambda}{8}$ open circuit shunt stub at the centre frequency, f_0.

ABCDscs: ABCD parameter of a $\frac{\lambda}{8}$ short circuit shunt stub at f_0

ABCDtl: ABCD parameters of a $\frac{\lambda}{4}$ transmission line at f_0

Gamma(even /odd): even/odd reflection coefficient

T(even/odd): even/odd transmission coefficient

```
> ABCDocs := matrix([ [1, 0], [I*tan(A/2)/Zo, 1] ]);
```

$$ABCDocs := \begin{bmatrix} 1 & 0 \\ \frac{I \tan(\frac{1}{2} A)}{Zo} & 1 \end{bmatrix}$$

```
> ABCDscs := matrix([ [1, 0], [1/(I*Zo*tan(A/2)), 1] ]);
```

$$ABCDscs := \begin{bmatrix} 1 & 0 \\ -\frac{I}{Zo \tan(\frac{1}{2} A)} & 1 \end{bmatrix}$$

```
> ABCDtl := matrix([ [cos(A), I*Zo/sqrt(2)*sin(A)], [sqrt(2)*I*sin(A)/Zo,
cos(A)] ]);
```

$$ABCDtl := \begin{bmatrix} \cos(A) & \frac{1}{2} I\, Zo \sqrt{2} \sin(A) \\ \frac{I \sqrt{2} \sin(A)}{Zo} & \cos(A) \end{bmatrix}$$

```
> ABCD_even := evalm(&*(ABCDocs,ABCDtl,ABCDocs));
```

$$ABCD\_even := \begin{bmatrix} \%1 & \frac{1}{2} I\, Zo \sqrt{2} \sin(A) \\ \frac{I \tan(\frac{1}{2}A)\cos(A)}{Zo} + \frac{I\sqrt{2}\sin(A)}{Zo} + \frac{I\,\%1 \tan(\frac{1}{2}A)}{Zo} & \%1 \end{bmatrix}$$

$$\%1 := -\frac{1}{2}\tan(\frac{1}{2}A)\sqrt{2}\sin(A) + \cos(A)$$

```
> ABCD_odd := evalm(&*(ABCDscs,ABCDtl,ABCDscs));
```

$$ABCD\_odd := \begin{bmatrix} \frac{1}{2}\frac{\sqrt{2}\sin(A)}{\tan(\frac{1}{2}A)} + \cos(A) & \frac{1}{2} I\, Zo \sqrt{2}\sin(A) \\ -\frac{I\cos(A)}{Zo\tan(\frac{1}{2}A)} + \frac{I\sqrt{2}\sin(A)}{Zo} - \frac{I\left(\frac{1}{2}\frac{\sqrt{2}\sin(A)}{\tan(\frac{1}{2}A)} + \cos(A)\right)}{Zo\tan(\frac{1}{2}A)} & \frac{1}{2}\frac{\sqrt{2}\sin(A)}{\tan(\frac{1}{2}A)} + \cos(A) \end{bmatrix}$$

```
> Gamma_Even := ( (ABCD_even[1,1] - ABCD_even[2,2]) + (ABCD_even[1,2]*1/Zo
- ABCD_even[2,1]*Zo) ) / ( (ABCD_even[1,1] + ABCD_even[2,2]) + (ABCD_even[1,2]*1/Zo
+ ABCD_even[2,1]*Zo) );
```

$$Gamma\_Even := \left(\frac{1}{2} I\sqrt{2}\sin(A) - \left(\frac{I\tan(\frac{1}{2}A)\cos(A)}{Zo} + \frac{I\sqrt{2}\sin(A)}{Zo} + \frac{I\left(-\frac{1}{2}\tan(\frac{1}{2}A)\sqrt{2}\sin(A) + \cos(A)\right)\tan(\frac{1}{2}A)}{Zo}\right) Zo\right)$$

$$\Big/ \left(-\tan(\frac{1}{2}A)\sqrt{2}\sin(A) + 2\cos(A) + \frac{1}{2} I\sqrt{2}\sin(A) + \left(\frac{I\tan(\frac{1}{2}A)\cos(A)}{Zo} + \frac{I\sqrt{2}\sin(A)}{Zo} + \frac{I\left(-\frac{1}{2}\tan(\frac{1}{2}A)\sqrt{2}\sin(A) + \cos(A)\right)\tan(\frac{1}{2}A)}{Zo}\right) Zo\right)$$

```
> Gamma_Odd := ( (ABCD_odd[1,1] - ABCD_odd[2,2]) + (ABCD_odd[1,2]/Zo
- ABCD_odd[2,1]*Zo) ) / ( (ABCD_odd[1,1] + ABCD_odd[2,2]) + (ABCD_odd[1,2]/Zo
+ ABCD_odd[2,1]*Zo) );
```

$$Gamma\_Odd := \left(\frac{1}{2} I \sqrt{2} \sin(A) - \left(-\frac{I \cos(A)}{Zo \tan(\frac{1}{2} A)} + \frac{I \sqrt{2} \sin(A)}{Zo} - \frac{I \left(\frac{1}{2} \frac{\sqrt{2} \sin(A)}{\tan(\frac{1}{2} A)} + \cos(A) \right)}{Zo \tan(\frac{1}{2} A)} \right) Z \right.$$

$$\left. \Big/ \left(\frac{\sqrt{2} \sin(A)}{\tan(\frac{1}{2} A)} + 2 \cos(A) + \frac{1}{2} I \sqrt{2} \sin(A) \right. \right.$$

$$\left. \left. + \left(-\frac{I \cos(A)}{Zo \tan(\frac{1}{2} A)} + \frac{I \sqrt{2} \sin(A)}{Zo} - \frac{I \left(\frac{1}{2} \frac{\sqrt{2} \sin(A)}{\tan(\frac{1}{2} A)} + \cos(A) \right)}{Zo \tan(\frac{1}{2} A)} \right) Zo \right) \right)$$

```
> T_Even := ( 2/((ABCD_even[1,1] + ABCD_even[2,2]) + (ABCD_even[1,2]/Zo
+ ABCD_even[2,1]*Zo) ) );
```

$$T\_Even := 21 / \left(-\tan(\frac{1}{2} A) \sqrt{2} \sin(A) + 2 \cos(A) + \frac{1}{2} I \sqrt{2} \sin(A) + \right.$$

$$\left. \left(\frac{I \tan(\frac{1}{2} A) \cos(A)}{Zo} + \frac{I \sqrt{2} \sin(A)}{Zo} + \frac{I \left(-\frac{1}{2} \tan(\frac{1}{2} A) \sqrt{2} \sin(A) + \cos(A) \right) \tan(\frac{1}{2} A)}{Zo} \right) Zo \right)$$

```
> T_Odd := ( 2/((ABCD_odd[1,1] + ABCD_odd[2,2]) + (ABCD_odd[1,2]/Zo
+ ABCD_odd[2,1]*Zo) ) );
```

$$T\_Odd := 21 / \left(\frac{\sqrt{2} \sin(A)}{\tan(\frac{1}{2} A)} + 2 \cos(A) + \frac{1}{2} I \sqrt{2} \sin(A) \right.$$

$$\left. + \left(-\frac{I \cos(A)}{Zo \tan(\frac{1}{2} A)} + \frac{I \sqrt{2} \sin(A)}{Zo} - \frac{I \left(\frac{1}{2} \frac{\sqrt{2} \sin(A)}{\tan(\frac{1}{2} A)} + \cos(A) \right)}{Zo \tan(\frac{1}{2} A)} \right) Zo \right)$$

```
> S11 := (Gamma_Even + Gamma_Odd)/2;
```

$$S11 := \frac{1}{2}\left(\frac{1}{2} I\sqrt{2}\sin(A) - \left(\frac{I\tan(\frac{1}{2}A)\cos(A)}{Zo} + \frac{I\sqrt{2}\sin(A)}{Zo} + \frac{I\left(-\frac{1}{2}\tan(\frac{1}{2}A)\sqrt{2}\sin(A)+\cos(A)\right)\tan(\frac{1}{2}A)}{Zo}\right) Zo\right) \Big/ \left(-\tan(\frac{1}{2}A)\sqrt{2}\sin(A) + 2\cos(A) + \frac{1}{2} I\sqrt{2}\sin(A) + \left(\frac{I\tan(\frac{1}{2}A)\cos(A)}{Zo} + \frac{I\sqrt{2}\sin(A)}{Zo} + \frac{I\left(-\frac{1}{2}\tan(\frac{1}{2}A)\sqrt{2}\sin(A)+\cos(A)\right)\tan(\frac{1}{2}A)}{Zo}\right) Zo\right) + \frac{1}{2}\left(\frac{1}{2} I\sqrt{2}\sin(A) - \left(-\frac{I\cos(A)}{Zo\tan(\frac{1}{2}A)} + \frac{I\sqrt{2}\sin(A)}{Zo} - \frac{I\left(\frac{1}{2}\frac{\sqrt{2}\sin(A)}{\tan(\frac{1}{2}A)} + \cos(A)\right)}{Zo\tan(\frac{1}{2}A)}\right) Zo\right) \Big/ \left(\frac{\sqrt{2}\sin(A)}{\tan(\frac{1}{2}A)} + 2\cos(A) + \frac{1}{2} I\sqrt{2}\sin(A) + \left(-\frac{I\cos(A)}{Zo\tan(\frac{1}{2}A)} + \frac{I\sqrt{2}\sin(A)}{Zo} - \frac{I\left(\frac{1}{2}\frac{\sqrt{2}\sin(A)}{\tan(\frac{1}{2}A)} + \cos(A)\right)}{Zo\tan(\frac{1}{2}A)}\right) Zo\right)$$

```
> S12 := (T_Even + T_Odd)/2;
```

$$S12 := 1/\left(-\tan(\frac{1}{2}A)\sqrt{2}\sin(A) + 2\cos(A) + \frac{1}{2} I\sqrt{2}\sin(A) + \left(\frac{I\tan(\frac{1}{2}A)\cos(A)}{Zo} + \frac{I\sqrt{2}\sin(A)}{Zo} + \frac{I\left(-\frac{1}{2}\tan(\frac{1}{2}A)\sqrt{2}\sin(A)+\cos(A)\right)\tan(\frac{1}{2}A)}{Zo}\right) Zo\right) + 1/\left(\frac{\sqrt{2}\sin(A)}{\tan(\frac{1}{2}A)} + 2\cos(A) + \frac{1}{2} I\sqrt{2}\sin(A) + \left(-\frac{I\cos(A)}{Zo\tan(\frac{1}{2}A)} + \frac{I\sqrt{2}\sin(A)}{Zo} - \frac{I\left(\frac{1}{2}\frac{\sqrt{2}\sin(A)}{\tan(\frac{1}{2}A)} + \cos(A)\right)}{Zo\tan(\frac{1}{2}A)}\right) Zo\right)$$

```
> S13 := (T_Even - T_Odd)/2;
```

$$S13 := 1/\left(-\tan\left(\frac{1}{2}A\right)\sqrt{2}\sin(A) + 2\cos(A) + \frac{1}{2}I\sqrt{2}\sin(A) + \left(\frac{I\tan\left(\frac{1}{2}A\right)\cos(A)}{Zo} + \frac{I\sqrt{2}\sin(A)}{Zo} + \frac{I\left(-\frac{1}{2}\tan\left(\frac{1}{2}A\right)\sqrt{2}\sin(A) + \cos(A)\right)\tan\left(\frac{1}{2}A\right)}{Zo}\right) Zo\right)$$

$$- 1/\left(\frac{\sqrt{2}\sin(A)}{\tan\left(\frac{1}{2}A\right)} + 2\cos(A) + \frac{1}{2}I\sqrt{2}\sin(A) + \left(-\frac{I\cos(A)}{Zo\tan\left(\frac{1}{2}A\right)} + \frac{I\sqrt{2}\sin(A)}{Zo} - \frac{I\left(\frac{1}{2}\frac{\sqrt{2}\sin(A)}{\tan\left(\frac{1}{2}A\right)} + \cos(A)\right)}{Zo\tan\left(\frac{1}{2}A\right)}\right) Zo\right)$$

```
> S14 := (Gamma_Even - Gamma_Odd)/2;
```

$$S14 := \frac{1}{2}\left(\frac{1}{2}I\sqrt{2}\sin(A) - \left(\frac{I\tan\left(\frac{1}{2}A\right)\cos(A)}{Zo} + \frac{I\sqrt{2}\sin(A)}{Zo} + \frac{I\left(-\frac{1}{2}\tan\left(\frac{1}{2}A\right)\sqrt{2}\sin(A) + \cos(A)\right)\tan\left(\frac{1}{2}A\right)}{Zo}\right) Zo\right)$$

$$\Big/\left(-\tan\left(\frac{1}{2}A\right)\sqrt{2}\sin(A) + 2\cos(A) + \frac{1}{2}I\sqrt{2}\sin(A) + \left(\frac{I\tan\left(\frac{1}{2}A\right)\cos(A)}{Zo} + \frac{I\sqrt{2}\sin(A)}{Zo} + \frac{I\left(-\frac{1}{2}\tan\left(\frac{1}{2}A\right)\sqrt{2}\sin(A) + \cos(A)\right)\tan\left(\frac{1}{2}A\right)}{Zo}\right) Zo\right)$$

$$- \frac{1}{2}\left(\frac{1}{2}I\sqrt{2}\sin(A) - \left(-\frac{I\cos(A)}{Zo\tan\left(\frac{1}{2}A\right)} + \frac{I\sqrt{2}\sin(A)}{Zo} - \frac{I\left(\frac{1}{2}\frac{\sqrt{2}\sin(A)}{\tan\left(\frac{1}{2}A\right)} + \cos(A)\right)}{Zo\tan\left(\frac{1}{2}A\right)}\right) Zo\right)$$

$$\Big/\left(\frac{\sqrt{2}\sin(A)}{\tan\left(\frac{1}{2}A\right)} + 2\cos(A) + \frac{1}{2}I\sqrt{2}\sin(A) + \left(-\frac{I\cos(A)}{Zo\tan\left(\frac{1}{2}A\right)} + \frac{I\sqrt{2}\sin(A)}{Zo} - \frac{I\left(\frac{1}{2}\frac{\sqrt{2}\sin(A)}{\tan\left(\frac{1}{2}A\right)} + \cos(A)\right)}{Zo\tan\left(\frac{1}{2}A\right)}\right) Zo\right)$$

Since the branch-line coupler circuit is symmetrical, $S_{12} = S_{21}$, $S_{13} = S_{31}$, and $S_{14} = S_{41}$.

A.2 S-Parameter Equations for the Distributed Rat-Race Coupler

The even and odd mode analysis and the S-Parameter equations for the rat-race Coupler are provided in this section. Maple V Release 5 was used for simplification of the analysis and equations. The definitions of the symbols used in the equations are provided. For the coupler with a zero degree phase difference between output ports 2 and 3 the coupler ports were labeled as shown in Figure A.1.

$A = \frac{\pi f}{2 f_0}$, where f is the frequency, and f_0 is the couplers centre frequency

ABCD_l8_oc: ABCD parameters of a $\frac{\lambda}{8}$ open circuit shunt stub at, f_0.

ABCD_l4_TL: ABCD parameters of a $\frac{\lambda}{4}$ transmission line at f_0

ABCD_3l8_oc: ABCD parameters of a $\frac{3\lambda}{8}$ open circuit shunt stub at, f_0.

ABCD_l8_sc: ABCD parameter of a $\frac{\lambda}{8}$ short circuit shunt stub at f_0

ABCD_3l8_sc: ABCD parameter of a $\frac{3\lambda}{8}$ short circuit shunt stub at f_0

Gamma(even /odd): even/odd reflection coefficient

T(even/odd): even/odd transmission coefficient

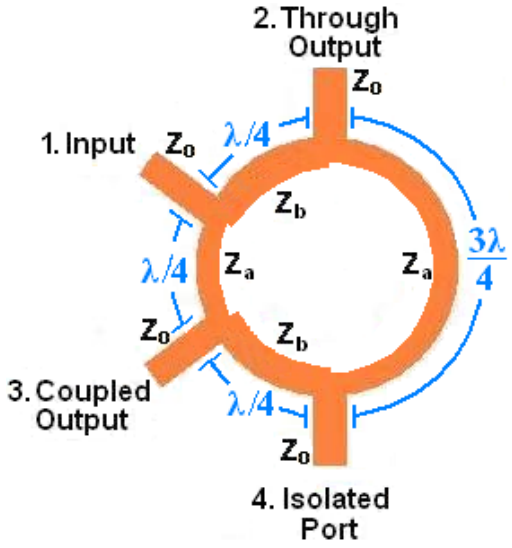

Figure A.1: Distributed Rat-Race Coupler with Zero Degree Phase Shift between Output Ports 2 and 3

```
> ABCD_l8_oc := matrix( [ [1, 0], [I*tan(A/2)/(sqrt(2)*Zo), 1]
]);
```

$$ABCD\_l8\_oc := \begin{bmatrix} 1 & 0 \\ \frac{1}{2}\,\frac{I\tan(\frac{1}{2}A)\sqrt{2}}{Zo} & 1 \end{bmatrix}$$

```
> ABCD_l4_TL := matrix( [ [cos(A), sqrt(2)*Zo*I*sin(A)], [I*sin(A)/(sqrt(2)*Zo)
cos(A)] ]);
```

$$ABCD\_l4\_TL := \begin{bmatrix} \cos(A) & I\sqrt{2}\,Zo\sin(A) \\ \frac{1}{2}\,\frac{I\sin(A)\sqrt{2}}{Zo} & \cos(A) \end{bmatrix}$$

```
> ABCD_3l8_oc := matrix( [ [1, 0], [I*tan(3*A/2)/(sqrt(2)*Zo),
1] ]);
```

$$ABCD\_3l8\_oc := \begin{bmatrix} 1 & 0 \\ \frac{1}{2}\,\frac{I\tan(\frac{3}{2}A)\sqrt{2}}{Zo} & 1 \end{bmatrix}$$

```
> ABCD_even := evalm(&*(ABCD_l8_oc,ABCD_l4_TL,ABCD_3l8_oc));
```

$$ABCD\_even := \left[-\tan(\frac{3}{2}A)\sin(A)+\cos(A)\,,\ I\sqrt{2}\,Zo\sin(A)\right]$$

$$\left[\frac{1}{2}\,\frac{I\tan(\frac{1}{2}A)\sqrt{2}\cos(A)}{Zo}+\frac{1}{2}\,\frac{I\sin(A)\sqrt{2}}{Zo}\right.$$

$$\left.+\frac{1}{2}\,\frac{I\left(\cos(A)-\sin(A)\tan(\frac{1}{2}A)\right)\tan(\frac{3}{2}A)\sqrt{2}}{Zo},\ \cos(A)-\sin(A)\tan(\frac{1}{2}A)\right]$$

```
> ABCD_l8_sc := matrix( [ [1,0], [-I/(sqrt(2)*Zo*tan(A/2)), 1]
] );
```

$$ABCD\_l8\_sc := \begin{bmatrix} 1 & 0 \\ -\frac{1}{2}\,\frac{I\sqrt{2}}{Zo\tan(\frac{1}{2}A)} & 1 \end{bmatrix}$$

```
> ABCD_3l8_sc := matrix( [ [1,0], [-I/(sqrt(2)*Zo*tan(3*A/2)),
1] ] );
```

$$ABCD\_3l8\_sc := \begin{bmatrix} 1 & 0 \\ -\frac{1}{2}\,\frac{I\sqrt{2}}{Zo\tan(\frac{3}{2}A)} & 1 \end{bmatrix}$$

```
> ABCD_odd := evalm(&*(ABCD_l8_sc,ABCD_l4_TL,ABCD_3l8_sc));
```

$$ABCD\_odd := \begin{bmatrix} \dfrac{\sin(A)}{\tan(\frac{3}{2}A)}+\cos(A) & I\sqrt{2}\,Zo\sin(A) \\ -\frac{1}{2}\,\dfrac{I\sqrt{2}\cos(A)}{Zo\tan(\frac{1}{2}A)}+\frac{1}{2}\,\dfrac{I\sin(A)\sqrt{2}}{Zo}-\frac{1}{2}\,\dfrac{I\left(\cos(A)+\dfrac{\sin(A)}{\tan(\frac{1}{2}A)}\right)\sqrt{2}}{Zo\tan(\frac{3}{2}A)} & \cos(A)+\dfrac{\sin(A)}{\tan(\frac{1}{2}A)} \end{bmatrix}$$

```
> Gamma_even := ( (ABCD_even[1,1] - ABCD_even[2,2]) + (ABCD_even[1,2]/Zo
- ABCD_even[2,1]*Zo) ) / ( (ABCD_even[1,1] + ABCD_even[2,2]) + (ABCD_even[1,2]/Zo
+ ABCD_even[2,1]*Zo) );
```

$$Gamma\_even := \left(-\tan(\frac{3}{2}A)\sin(A) + \%1 + I\sqrt{2}\sin(A) - \left(\frac{1}{2}\frac{I\tan(\frac{1}{2}A)\sqrt{2}\cos(A)}{Zo} + \frac{1}{2}\frac{I\sin(A)\sqrt{2}}{Zo} + \frac{1}{2}\frac{I(\cos(A)-\%1)\tan(\frac{3}{2}A)\sqrt{2}}{Zo} \right) Zo \right) \Big/ \left(-\tan(\frac{3}{2}A)\sin(A) + 2\cos(A) - \%1 + I\sqrt{2}\sin(A) + \left(\frac{1}{2}\frac{I\tan(\frac{1}{2}A)\sqrt{2}\cos(A)}{Zo} + \frac{1}{2}\frac{I\sin(A)\sqrt{2}}{Zo} + \frac{1}{2}\frac{I(\cos(A)-\%1)\tan(\frac{3}{2}A)\sqrt{2}}{Zo} \right) Zo \right)$$

$$\%1 := \sin(A)\tan(\frac{1}{2}A)$$

```
> Gamma_odd := ( (ABCD_odd[1,1] - ABCD_odd[2,2]) + (ABCD_odd[1,2]/Zo
- ABCD_odd[2,1]*Zo) ) / ( (ABCD_odd[1,1] + ABCD_odd[2,2]) + (ABCD_odd[1,2]/Zo
+ ABCD_odd[2,1]*Zo) );
```

$$Gamma\_odd := \left(\frac{\sin(A)}{\tan(\frac{3}{2}A)} - \frac{\sin(A)}{\tan(\frac{1}{2}A)} + I\sqrt{2}\sin(A) - \left(-\frac{1}{2}\frac{I\sqrt{2}\cos(A)}{Zo\tan(\frac{1}{2}A)} + \frac{1}{2}\frac{I\sin(A)\sqrt{2}}{Zo} - \frac{1}{2}\frac{I\left(\cos(A)+\frac{\sin(A)}{\tan(\frac{1}{2}A)}\right)\sqrt{2}}{Zo\tan(\frac{3}{2}A)} \right) Zo \right) \Big/ \left(\frac{\sin(A)}{\tan(\frac{3}{2}A)} + 2\cos(A) + \frac{\sin(A)}{\tan(\frac{1}{2}A)} + I\sqrt{2}\sin(A) + \left(-\frac{1}{2}\frac{I\sqrt{2}\cos(A)}{Zo\tan(\frac{1}{2}A)} + \frac{1}{2}\frac{I\sin(A)\sqrt{2}}{Zo} - \frac{1}{2}\frac{I\left(\cos(A)+\frac{\sin(A)}{\tan(\frac{1}{2}A)}\right)\sqrt{2}}{Zo\tan(\frac{3}{2}A)} \right) Zo \right)$$

```
> T_even := 2 / ( (ABCD_even[1,1] + ABCD_even[2,2]) + (ABCD_even[1,2]/Zo
+ ABCD_even[2,1]*Zo) );
```

$$T\_even := 21/\left(-\tan(\frac{3}{2}A)\sin(A)+2\cos(A)-\sin(A)\tan(\frac{1}{2}A)+I\sqrt{2}\sin(A)+\left(\right.\right.$$

$$\frac{1}{2}\frac{I\tan(\frac{1}{2}A)\sqrt{2}\cos(A)}{Zo}+\frac{1}{2}\frac{I\sin(A)\sqrt{2}}{Zo}$$

$$\left.\left.+\frac{1}{2}\frac{I\left(\cos(A)-\sin(A)\tan(\frac{1}{2}A)\right)\tan(\frac{3}{2}A)\sqrt{2}}{Zo}\right)Zo\right)$$

```
> T_odd := 2 / ( (ABCD_odd[1,1] + ABCD_odd[2,2]) + (ABCD_odd[1,2]/Zo
+ ABCD_odd[2,1]*Zo) );
```

$$T\_odd := 21/\left(\frac{\sin(A)}{\tan(\frac{3}{2}A)}+2\cos(A)+\frac{\sin(A)}{\tan(\frac{1}{2}A)}+I\sqrt{2}\sin(A)\right.$$

$$\left.+\left(-\frac{1}{2}\frac{I\sqrt{2}\cos(A)}{Zo\tan(\frac{1}{2}A)}+\frac{1}{2}\frac{I\sin(A)\sqrt{2}}{Zo}-\frac{1}{2}\frac{I\left(\cos(A)+\frac{\sin(A)}{\tan(\frac{1}{2}A)}\right)\sqrt{2}}{Zo\tan(\frac{3}{2}A)}\right)Zo\right)$$

```
> S11 := ( Gamma_even + Gamma_odd )/2;
```

$$S11 := \frac{1}{2}\left(-\tan(\frac{3}{2}A)\sin(A)+\%1+I\sqrt{2}\sin(A)\right.$$

$$\left.-\left(\frac{1}{2}\frac{I\tan(\frac{1}{2}A)\sqrt{2}\cos(A)}{Zo}+\frac{1}{2}\frac{I\sin(A)\sqrt{2}}{Zo}+\frac{1}{2}\frac{I\left(\cos(A)-\%1\right)\tan(\frac{3}{2}A)\sqrt{2}}{Zo}\right)Zo\right)$$

$$\Big/\left(-\tan(\frac{3}{2}A)\sin(A)+2\cos(A)-\%1+I\sqrt{2}\sin(A)\right.$$

$$\left.+\left(\frac{1}{2}\frac{I\tan(\frac{1}{2}A)\sqrt{2}\cos(A)}{Zo}+\frac{1}{2}\frac{I\sin(A)\sqrt{2}}{Zo}+\frac{1}{2}\frac{I\left(\cos(A)-\%1\right)\tan(\frac{3}{2}A)\sqrt{2}}{Zo}\right)Zo\right)+\frac{1}{2}\left($$

$$\frac{\sin(A)}{\tan(\frac{3}{2}A)} - \frac{\sin(A)}{\tan(\frac{1}{2}A)} + I\sqrt{2}\sin(A)$$

$$- \left(-\frac{1}{2}\frac{I\sqrt{2}\cos(A)}{Zo\tan(\frac{1}{2}A)} + \frac{1}{2}\frac{I\sin(A)\sqrt{2}}{Zo} - \frac{1}{2}\frac{I\left(\cos(A) + \frac{\sin(A)}{\tan(\frac{1}{2}A)}\right)\sqrt{2}}{Zo\tan(\frac{3}{2}A)} \right) Zo \Bigg)$$

$$\Bigg/ \left(\frac{\sin(A)}{\tan(\frac{3}{2}A)} + 2\cos(A) + \frac{\sin(A)}{\tan(\frac{1}{2}A)} + I\sqrt{2}\sin(A) \right.$$

$$+ \left(-\frac{1}{2}\frac{I\sqrt{2}\cos(A)}{Zo\tan(\frac{1}{2}A)} + \frac{1}{2}\frac{I\sin(A)\sqrt{2}}{Zo} - \frac{1}{2}\frac{I\left(\cos(A) + \frac{\sin(A)}{\tan(\frac{1}{2}A)}\right)\sqrt{2}}{Zo\tan(\frac{3}{2}A)} \right) Zo \Bigg)$$

$$\%1 := \sin(A)\tan(\frac{1}{2}A)$$

```
> S12 := ( T_even + T_odd ) / 2;
```

$$S12 := 1/\left(-\tan(\frac{3}{2}A)\sin(A) + 2\cos(A) - \sin(A)\tan(\frac{1}{2}A) + I\sqrt{2}\sin(A) + \left(\right.\right.$$

$$\frac{1}{2}\frac{I\tan(\frac{1}{2}A)\sqrt{2}\cos(A)}{Zo} + \frac{1}{2}\frac{I\sin(A)\sqrt{2}}{Zo}$$

$$\left.\left. + \frac{1}{2}\frac{I\left(\cos(A) - \sin(A)\tan(\frac{1}{2}A)\right)\tan(\frac{3}{2}A)\sqrt{2}}{Zo} \right) Zo \right) + 1/\left(\frac{\sin(A)}{\tan(\frac{3}{2}A)} + 2\cos(A) \right.$$

$$\left. + \frac{\sin(A)}{\tan(\frac{1}{2}A)} + I\sqrt{2}\sin(A) \right.$$

$$\left. + \left(-\frac{1}{2}\frac{I\sqrt{2}\cos(A)}{Zo\tan(\frac{1}{2}A)} + \frac{1}{2}\frac{I\sin(A)\sqrt{2}}{Zo} - \frac{1}{2}\frac{I\left(\cos(A) + \frac{\sin(A)}{\tan(\frac{1}{2}A)}\right)\sqrt{2}}{Zo\tan(\frac{3}{2}A)} \right) Zo \right)$$

```
> S13 := ( Gamma_even - Gamma_odd ) / 2;
```

$$S13 := \frac{1}{2}\left(-\tan(\frac{3}{2}A)\sin(A) + \%1 + I\sqrt{2}\sin(A) - \left(\frac{1}{2}\frac{I\tan(\frac{1}{2}A)\sqrt{2}\cos(A)}{Zo} + \frac{1}{2}\frac{I\sin(A)\sqrt{2}}{Zo} + \frac{1}{2}\frac{I(\cos(A)-\%1)\tan(\frac{3}{2}A)\sqrt{2}}{Zo}\right) Zo\right)$$
$$\Big/\left(-\tan(\frac{3}{2}A)\sin(A) + 2\cos(A) - \%1 + I\sqrt{2}\sin(A) + \left(\frac{1}{2}\frac{I\tan(\frac{1}{2}A)\sqrt{2}\cos(A)}{Zo} + \frac{1}{2}\frac{I\sin(A)\sqrt{2}}{Zo} + \frac{1}{2}\frac{I(\cos(A)-\%1)\tan(\frac{3}{2}A)\sqrt{2}}{Zo}\right) Zo\right) - \frac{1}{2}\left(\frac{\sin(A)}{\tan(\frac{3}{2}A)} - \frac{\sin(A)}{\tan(\frac{1}{2}A)} + I\sqrt{2}\sin(A) - \left(-\frac{1}{2}\frac{I\sqrt{2}\cos(A)}{Zo\tan(\frac{1}{2}A)} + \frac{1}{2}\frac{I\sin(A)\sqrt{2}}{Zo} - \frac{1}{2}\frac{I\left(\cos(A)+\frac{\sin(A)}{\tan(\frac{1}{2}A)}\right)\sqrt{2}}{Zo\tan(\frac{3}{2}A)}\right) Zo\right)$$
$$\Big/\left(\frac{\sin(A)}{\tan(\frac{3}{2}A)} + 2\cos(A) + \frac{\sin(A)}{\tan(\frac{1}{2}A)} + I\sqrt{2}\sin(A) + \left(-\frac{1}{2}\frac{I\sqrt{2}\cos(A)}{Zo\tan(\frac{1}{2}A)} + \frac{1}{2}\frac{I\sin(A)\sqrt{2}}{Zo} - \frac{1}{2}\frac{I\left(\cos(A)+\frac{\sin(A)}{\tan(\frac{1}{2}A)}\right)\sqrt{2}}{Zo\tan(\frac{3}{2}A)}\right) Zo\right)$$

$$\%1 := \sin(A)\tan(\frac{1}{2}A)$$

```
> S14 := ( T_even - T_odd ) / 2;
```

$$S14 := 1/\left(-\tan\left(\frac{3}{2}A\right)\sin(A) + 2\cos(A) - \sin(A)\tan\left(\frac{1}{2}A\right) + I\sqrt{2}\sin(A) + \left(\right.\right.$$

$$\frac{1}{2}\frac{I\tan\left(\frac{1}{2}A\right)\sqrt{2}\cos(A)}{Zo} + \frac{1}{2}\frac{I\sin(A)\sqrt{2}}{Zo}$$

$$\left.\left. + \frac{1}{2}\frac{I\left(\cos(A) - \sin(A)\tan\left(\frac{1}{2}A\right)\right)\tan\left(\frac{3}{2}A\right)\sqrt{2}}{Zo}\right) Zo\right) - 1/\left(\frac{\sin(A)}{\tan\left(\frac{3}{2}A\right)} + 2\cos(A)\right.$$

$$+ \frac{\sin(A)}{\tan\left(\frac{1}{2}A\right)} + I\sqrt{2}\sin(A)$$

$$+ \left(-\frac{1}{2}\frac{I\sqrt{2}\cos(A)}{Zo\tan\left(\frac{1}{2}A\right)} + \frac{1}{2}\frac{I\sin(A)\sqrt{2}}{Zo} - \frac{1}{2}\frac{I\left(\cos(A) + \frac{\sin(A)}{\tan\left(\frac{1}{2}A\right)}\right)\sqrt{2}}{Zo\tan\left(\frac{3}{2}A\right)}\right) Zo\Bigg)$$

Since the rat-race coupler circuit is symmetrical, $S_{12} = S_{21}$, $S_{13} = S_{31}$, and $S_{14} = S_{41}$.

For the rat-race coupler with a 180 degree phase difference between output ports 2 and 3 the coupler ports and lumped elements were labeled as shown in Figure A.2. The definitions of the symbols are the same as the rat-race coupler with zero degree phase difference between output ports 2 and 3.

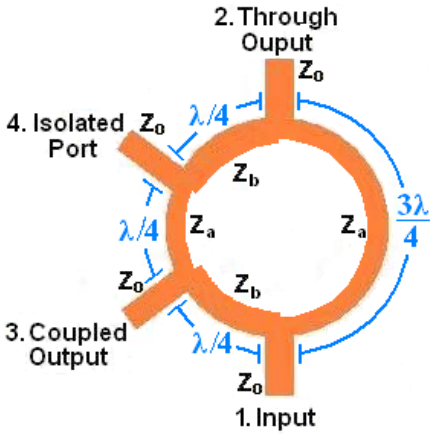

Figure A.2: Distributed Rat-Race Coupler with 180 Degree Phase Shift between Output Ports 2 and 3

```
> ABCD_l8_oc := matrix( [ [1, 0], [I*tan(A/2)/(sqrt(2)*Zo), 1]
]);
```

$$ABCD\_l8\_oc := \begin{bmatrix} 1 & 0 \\ \frac{1}{2}\,\frac{I\tan(\frac{1}{2}A)\sqrt{2}}{Zo} & 1 \end{bmatrix}$$

```
> ABCD_l4_TL := matrix( [ [cos(A), sqrt(2)*Zo*I*sin(A)], [I*sin(A)/(sqrt(2)*Zo
cos(A)] ]);
```

$$ABCD\_l4\_TL := \begin{bmatrix} \cos(A) & I\sqrt{2}\,Zo\sin(A) \\ \frac{1}{2}\,\frac{I\sin(A)\sqrt{2}}{Zo} & \cos(A) \end{bmatrix}$$

```
> ABCD_3l8_oc := matrix( [ [1, 0], [I*tan(3*A/2)/(sqrt(2)*Zo),
1] ]);
```

$$ABCD\_3l8\_oc := \begin{bmatrix} 1 & 0 \\ \frac{1}{2}\,\frac{I\tan(\frac{3}{2}A)\sqrt{2}}{Zo} & 1 \end{bmatrix}$$

```
> ABCD_even := evalm(&*(ABCD_3l8_oc,ABCD_l4_TL,ABCD_l8_oc));
```

$$ABCD\_even := \left[\cos(A) - \sin(A)\tan(\tfrac{1}{2}A)\,,\ I\sqrt{2}\,Zo\sin(A)\right]$$

$$\left[\frac{1}{2}\,\frac{I\tan(\frac{3}{2}A)\sqrt{2}\cos(A)}{Zo} + \frac{1}{2}\,\frac{I\sin(A)\sqrt{2}}{Zo}\right.$$

$$\left. + \frac{1}{2}\,\frac{I\,(-\tan(\frac{3}{2}A)\sin(A) + \cos(A))\tan(\frac{1}{2}A)\sqrt{2}}{Zo},\ -\tan(\tfrac{3}{2}A)\sin(A) + \cos(A)\right]$$

```
> ABCD_l8_sc := matrix( [ [1,0], [-I/(sqrt(2)*Zo*tan(A/2)), 1]
] );
```

$$ABCD\_l8\_sc := \begin{bmatrix} 1 & 0 \\ -\frac{1}{2}\,\frac{I\sqrt{2}}{Zo\tan(\frac{1}{2}A)} & 1 \end{bmatrix}$$

```
> ABCD_3l8_sc := matrix( [ [1,0], [-I/(sqrt(2)*Zo*tan(3*A/2)),
1] ] );
```

$$ABCD\_3l8\_sc := \begin{bmatrix} 1 & 0 \\ -\frac{1}{2}\,\frac{I\sqrt{2}}{Zo\tan(\frac{3}{2}A)} & 1 \end{bmatrix}$$

```
> ABCD_odd := evalm(&*(ABCD_3l8_sc,ABCD_l4_TL,ABCD_l8_sc));
```

$$ABCD\_odd :=$$

$$\begin{bmatrix} \cos(A) + \dfrac{\sin(A)}{\tan(\frac{1}{2}A)} & I\sqrt{2}\,Zo\sin(A) \\ -\dfrac{1}{2}\dfrac{I\sqrt{2}\cos(A)}{Zo\tan(\frac{3}{2}A)} + \dfrac{1}{2}\dfrac{I\sin(A)\sqrt{2}}{Zo} - \dfrac{1}{2}\dfrac{I\left(\dfrac{\sin(A)}{\tan(\frac{3}{2}A)} + \cos(A)\right)\sqrt{2}}{Zo\tan(\frac{1}{2}A)} & \dfrac{\sin(A)}{\tan(\frac{3}{2}A)} + \cos(A) \end{bmatrix}$$

```
> Gamma_even := ( (ABCD_even[1,1] - ABCD_even[2,2]) + (ABCD_even[1,2]/Zo
- ABCD_even[2,1]*Zo) ) / ( (ABCD_even[1,1] + ABCD_even[2,2]) + (ABCD_even[1,2]/Z
+ ABCD_even[2,1]*Zo) );
```

$$Gamma\_even := \left(-\sin(A)\tan(\frac{1}{2}A) + \%1 + I\sqrt{2}\sin(A) - \left(\frac{1}{2}\frac{I\tan(\frac{3}{2}A)\sqrt{2}\cos(A)}{Zo} + \frac{1}{2}\frac{I\sin(A)\sqrt{2}}{Zo} + \frac{1}{2}\frac{I(-\%1+\cos(A))\tan(\frac{1}{2}A)\sqrt{2}}{Zo}\right) Zo\right) \Big/ \left(2\cos(A) - \sin(A)\tan(\frac{1}{2}A) - \%1 + I\sqrt{2}\sin(A) + \left(\frac{1}{2}\frac{I\tan(\frac{3}{2}A)\sqrt{2}\cos(A)}{Zo} + \frac{1}{2}\frac{I\sin(A)\sqrt{2}}{Zo} + \frac{1}{2}\frac{I(-\%1+\cos(A))\tan(\frac{1}{2}A)\sqrt{2}}{Zo}\right) Zo\right)$$

$$\%1 := \tan(\frac{3}{2}A)\sin(A)$$

```
> Gamma_odd := ( (ABCD_odd[1,1] - ABCD_odd[2,2]) + (ABCD_odd[1,2]/Zo
- ABCD_odd[2,1]*Zo) ) / ( (ABCD_odd[1,1] + ABCD_odd[2,2]) + (ABCD_odd[1,2]/Zo
+ ABCD_odd[2,1]*Zo) );
```

$$Gamma\_odd := \left(\frac{\sin(A)}{\tan(\frac{1}{2}A)} - \frac{\sin(A)}{\tan(\frac{3}{2}A)} + I\sqrt{2}\sin(A) - \left(-\frac{1}{2}\frac{I\sqrt{2}\cos(A)}{Zo\tan(\frac{3}{2}A)} + \frac{1}{2}\frac{I\sin(A)\sqrt{2}}{Zo} - \frac{1}{2}\frac{I\left(\dfrac{\sin(A)}{\tan(\frac{3}{2}A)} + \cos(A)\right)\sqrt{2}}{Zo\tan(\frac{1}{2}A)}\right) Zo\right)$$

$$/\left(2\cos(A)+\frac{\sin(A)}{\tan(\frac{1}{2}A)}+\frac{\sin(A)}{\tan(\frac{3}{2}A)}+I\sqrt{2}\sin(A)\right.$$
$$\left.+\left(-\frac{1}{2}\frac{I\sqrt{2}\cos(A)}{Zo\tan(\frac{3}{2}A)}+\frac{1}{2}\frac{I\sin(A)\sqrt{2}}{Zo}-\frac{1}{2}\frac{I\left(\frac{\sin(A)}{\tan(\frac{3}{2}A)}+\cos(A)\right)\sqrt{2}}{Zo\tan(\frac{1}{2}A)}\right)Zo\right)$$

```
> T_even := 2 / ( (ABCD_even[1,1] + ABCD_even[2,2]) + (ABCD_even[1,2]/Zo
+ ABCD_even[2,1]*Zo) );
```

$$T\_even := 21/\left(2\cos(A)-\sin(A)\tan(\frac{1}{2}A)-\tan(\frac{3}{2}A)\sin(A)+I\sqrt{2}\sin(A)+\left(\right.\right.$$
$$\frac{1}{2}\frac{I\tan(\frac{3}{2}A)\sqrt{2}\cos(A)}{Zo}+\frac{1}{2}\frac{I\sin(A)\sqrt{2}}{Zo}$$
$$\left.\left.+\frac{1}{2}\frac{I\left(-\tan(\frac{3}{2}A)\sin(A)+\cos(A)\right)\tan(\frac{1}{2}A)\sqrt{2}}{Zo}\right)Zo\right)$$

```
> T_odd := 2 / ( (ABCD_odd[1,1] + ABCD_odd[2,2]) + (ABCD_odd[1,2]/Zo
+ ABCD_odd[2,1]*Zo) );
```

$$T\_odd := 21/\left(2\cos(A)+\frac{\sin(A)}{\tan(\frac{1}{2}A)}+\frac{\sin(A)}{\tan(\frac{3}{2}A)}+I\sqrt{2}\sin(A)\right.$$
$$\left.+\left(-\frac{1}{2}\frac{I\sqrt{2}\cos(A)}{Zo\tan(\frac{3}{2}A)}+\frac{1}{2}\frac{I\sin(A)\sqrt{2}}{Zo}-\frac{1}{2}\frac{I\left(\frac{\sin(A)}{\tan(\frac{3}{2}A)}+\cos(A)\right)\sqrt{2}}{Zo\tan(\frac{1}{2}A)}\right)Zo\right)$$

```
> S11 := ( Gamma_even + Gamma_odd )/2;
```

$$S11 := \frac{1}{2}\left(-\sin(A)\tan(\frac{1}{2}A)+\%1+I\sqrt{2}\sin(A)\right.$$
$$\left.-\left(\frac{1}{2}\frac{I\tan(\frac{3}{2}A)\sqrt{2}\cos(A)}{Zo}+\frac{1}{2}\frac{I\sin(A)\sqrt{2}}{Zo}+\frac{1}{2}\frac{I\left(-\%1+\cos(A)\right)\tan(\frac{1}{2}A)\sqrt{2}}{Zo}\right)Zo\right)$$

$$
\Bigg/\left(2\cos(A)-\sin(A)\tan(\frac{1}{2}A)-\%1+I\sqrt{2}\sin(A)\right.
$$

$$
\left.+\left(\frac{1}{2}\frac{I\tan(\frac{3}{2}A)\sqrt{2}\cos(A)}{Zo}+\frac{1}{2}\frac{I\sin(A)\sqrt{2}}{Zo}+\frac{1}{2}\frac{I\left(-\%1+\cos(A)\right)\tan(\frac{1}{2}A)\sqrt{2}}{Zo}\right)Zo\right)+
$$

$$
\frac{1}{2}\left(\frac{\sin(A)}{\tan(\frac{1}{2}A)}-\frac{\sin(A)}{\tan(\frac{3}{2}A)}+I\sqrt{2}\sin(A)\right.
$$

$$
\left.-\left(-\frac{1}{2}\frac{I\sqrt{2}\cos(A)}{Zo\tan(\frac{3}{2}A)}+\frac{1}{2}\frac{I\sin(A)\sqrt{2}}{Zo}-\frac{1}{2}\frac{I\left(\frac{\sin(A)}{\tan(\frac{3}{2}A)}+\cos(A)\right)\sqrt{2}}{Zo\tan(\frac{1}{2}A)}\right)Zo\right)
$$

$$
\Bigg/\left(2\cos(A)+\frac{\sin(A)}{\tan(\frac{1}{2}A)}+\frac{\sin(A)}{\tan(\frac{3}{2}A)}+I\sqrt{2}\sin(A)\right.
$$

$$
\left.+\left(-\frac{1}{2}\frac{I\sqrt{2}\cos(A)}{Zo\tan(\frac{3}{2}A)}+\frac{1}{2}\frac{I\sin(A)\sqrt{2}}{Zo}-\frac{1}{2}\frac{I\left(\frac{\sin(A)}{\tan(\frac{3}{2}A)}+\cos(A)\right)\sqrt{2}}{Zo\tan(\frac{1}{2}A)}\right)Zo\right)
$$

$$
\%1:=\tan(\frac{3}{2}A)\sin(A)
$$

```
> S12 := ( Gamma_even - Gamma_odd ) / 2;
```

$$
S12:=\frac{1}{2}\left(-\sin(A)\tan(\frac{1}{2}A)+\%1+I\sqrt{2}\sin(A)\right.
$$

$$
\left.-\left(\frac{1}{2}\frac{I\tan(\frac{3}{2}A)\sqrt{2}\cos(A)}{Zo}+\frac{1}{2}\frac{I\sin(A)\sqrt{2}}{Zo}+\frac{1}{2}\frac{I\left(-\%1+\cos(A)\right)\tan(\frac{1}{2}A)\sqrt{2}}{Zo}\right)Zo\right)
$$

$$
\Bigg/\left(2\cos(A)-\sin(A)\tan(\frac{1}{2}A)-\%1+I\sqrt{2}\sin(A)\right.
$$

$$+\left(\frac{1}{2}\,\frac{I\tan(\frac{3}{2}A)\sqrt{2}\cos(A)}{Zo}+\frac{1}{2}\,\frac{I\sin(A)\sqrt{2}}{Zo}+\frac{1}{2}\,\frac{I\,(-\%1+\cos(A))\tan(\frac{1}{2}A)\sqrt{2}}{Zo}\right)Zo\Bigg)-$$

$$\frac{1}{2}\left(\frac{\sin(A)}{\tan(\frac{1}{2}A)}-\frac{\sin(A)}{\tan(\frac{3}{2}A)}+I\sqrt{2}\sin(A)\right.$$

$$\left.-\left(-\frac{1}{2}\,\frac{I\sqrt{2}\cos(A)}{Zo\tan(\frac{3}{2}A)}+\frac{1}{2}\,\frac{I\sin(A)\sqrt{2}}{Zo}-\frac{1}{2}\,\frac{I\left(\frac{\sin(A)}{\tan(\frac{3}{2}A)}+\cos(A)\right)\sqrt{2}}{Zo\tan(\frac{1}{2}A)}\right)Zo\right)$$

$$\Bigg/\left(2\cos(A)+\frac{\sin(A)}{\tan(\frac{1}{2}A)}+\frac{\sin(A)}{\tan(\frac{3}{2}A)}+I\sqrt{2}\sin(A)\right.$$

$$\left.+\left(-\frac{1}{2}\,\frac{I\sqrt{2}\cos(A)}{Zo\tan(\frac{3}{2}A)}+\frac{1}{2}\,\frac{I\sin(A)\sqrt{2}}{Zo}-\frac{1}{2}\,\frac{I\left(\frac{\sin(A)}{\tan(\frac{3}{2}A)}+\cos(A)\right)\sqrt{2}}{Zo\tan(\frac{1}{2}A)}\right)Zo\right)$$

$$\%1 := \tan(\frac{3}{2}A)\sin(A)$$

```
> S13 := ( T_even + T_odd ) / 2;
```

$$S13 := 1/\left(2\cos(A)-\sin(A)\tan(\frac{1}{2}A)-\tan(\frac{3}{2}A)\sin(A)+I\sqrt{2}\sin(A)+\left(\right.\right.$$

$$\frac{1}{2}\,\frac{I\tan(\frac{3}{2}A)\sqrt{2}\cos(A)}{Zo}+\frac{1}{2}\,\frac{I\sin(A)\sqrt{2}}{Zo}$$

$$\left.\left.+\frac{1}{2}\,\frac{I\,(-\tan(\frac{3}{2}A)\sin(A)+\cos(A))\tan(\frac{1}{2}A)\sqrt{2}}{Zo}\right)Zo\right)+1/\left(2\cos(A)+\frac{\sin(A)}{\tan(\frac{1}{2}A)}\right.$$

$$\left.+\frac{\sin(A)}{\tan(\frac{3}{2}A)}+I\sqrt{2}\sin(A)\right.$$

$$+\left(-\frac{1}{2}\,\frac{I\sqrt{2}\cos(A)}{Zo\tan(\frac{3}{2}A)}+\frac{1}{2}\,\frac{I\sin(A)\sqrt{2}}{Zo}-\frac{1}{2}\,\frac{I\left(\frac{\sin(A)}{\tan(\frac{3}{2}A)}+\cos(A)\right)\sqrt{2}}{Zo\tan(\frac{1}{2}A)}\right)Zo\Bigg)$$

```
> S14 := ( T_even - T_odd ) / 2;
```

$$S14 := 1/\Bigg(2\cos(A)-\sin(A)\tan(\frac{1}{2}A)-\tan(\frac{3}{2}A)\sin(A)+I\sqrt{2}\sin(A)+\Bigg($$

$$\frac{1}{2}\,\frac{I\tan(\frac{3}{2}A)\sqrt{2}\cos(A)}{Zo}+\frac{1}{2}\,\frac{I\sin(A)\sqrt{2}}{Zo}$$

$$+\frac{1}{2}\,\frac{I\left(-\tan(\frac{3}{2}A)\sin(A)+\cos(A)\right)\tan(\frac{1}{2}A)\sqrt{2}}{Zo}\Bigg)Zo\Bigg)-1/\Bigg(2\cos(A)+\frac{\sin(A}{\tan(\frac{1}{2}}$$

$$+\frac{\sin(A)}{\tan(\frac{3}{2}A)}+I\sqrt{2}\sin(A)$$

$$+\left(-\frac{1}{2}\,\frac{I\sqrt{2}\cos(A)}{Zo\tan(\frac{3}{2}A)}+\frac{1}{2}\,\frac{I\sin(A)\sqrt{2}}{Zo}-\frac{1}{2}\,\frac{I\left(\frac{\sin(A)}{\tan(\frac{3}{2}A)}+\cos(A)\right)\sqrt{2}}{Zo\tan(\frac{1}{2}A)}\right)Zo\Bigg)$$

Since the rat-race coupler circuit is symmetrical, $S_{12} = S_{21}$, $S_{13} = S_{31}$, and $S_{14} = S_{41}$.

APPENDIX B
S-PARAMETER EQUATIONS FOR LUMPED ELEMENT COUPLERS

B.1 S-Parameter Equations for the Lumped Element Branch-line Coupler

The even and odd mode analysis and the S-Parameter equations for the Branch-line Coupler are provided in this section. Maple V Release 5 was used for simplification of the analysis and equations. The definitions of the symbols used in the equations are provided below.

shC: shunt capacitor

c: capacitor

I: imaginary number, commonly known as j or i

ω: radian frequency, 2πf, where f is the frequency in Hz.

shL: shunt inductor

seL: series inductor

L1: inductor 1

L2: inductor 2

Gamma(even /odd): even/odd reflection coefficient

T(even/odd): even/odd transmission coefficient

```
> shC :=matrix( [ [1,0], [I*omega*c, 1] ] );
```

$$shC := \begin{bmatrix} 1 & 0 \\ I\,\omega\,c & 1 \end{bmatrix}$$

```
> shL :=matrix( [ [1,0], [-2*I/(omega*L_1), 1] ] );
```

$$shL := \begin{bmatrix} 1 & 0 \\ -2\,\dfrac{I}{\omega\,L\_1} & 1 \end{bmatrix}$$

```
> seL :=matrix( [ [1,I*omega*L_2], [0,1] ] );
```

$$seL := \begin{bmatrix} 1 & I\,\omega\,L\_2 \\ 0 & 1 \end{bmatrix}$$

```
> ABCD_odd := evalm(&*(shC, shL, seL, shL, shC));
```

$$ABCD\_odd := \begin{bmatrix} 1+2\,\dfrac{L\_2}{L\_1}-\omega^2\,L\_2\,c & I\,\omega\,L\_2 \\ I\,\omega\,c-2\,\dfrac{I}{\omega\,L\_1}-2\,\dfrac{I\,\%1}{\omega\,L\_1}+I\,\%1\,\omega\,c & \%1 \end{bmatrix}$$

$$\%1 := I\,(I\,\omega\,c-2\,\frac{I}{\omega\,L\_1})\,\omega\,L\_2+1$$

```
> Gamma_Odd := simplify(( (ABCD_odd[1,1]-ABCD_odd[2,2]) + (ABCD_odd[1,2]/50
- ABCD_odd[2,1]*50) )/( (ABCD_odd[1,1]+ABCD_odd[2,2]) + (ABCD_odd[1,2]/50
+ ABCD_odd[2,1]*50) ));
```

$$Gamma\_Odd := -I(\omega^2\, L\_2\, L\_1^{\,2} - 5000\,\omega^2\, c\, L\_1^{\,2} + 10000\, L\_1 - 10000\, L\_2\,\omega^2\, c\, L\_1 + 10000\, L\_2 + 2500\,\omega^4\, c^2\, L\_1^{\,2}\, L\_2) \Big/ (-100\,\omega\, L\_1^{\,2} - 200\, L\_2\,\omega\, L\_1 + 100\,\omega^3\, L\_2\, c\, L\_1^{\,2} - I\,\omega^2\, L\_2\, L\_1^{\,2} - 5000\, I\,\omega^2\, c\, L\_1^{\,2} + 10000\, I\, L\_1 - 10000\, I\, L\_2\,\omega^2\, c\, L\_1 + 10000\, I\, L\_2 + 2500\, I\,\omega^4\, c^2\, L\_1^{\,2}\, L\_2)$$

```
> T_odd := simplify(2/( (ABCD_odd[1,1]+ABCD_odd[2,2]) + (ABCD_odd[1,2]/50
+ ABCD_odd[2,1]*50) ));
```

$$T\_odd := -100\omega\, L\_1^{\,2}/(-100\,\omega\, L\_1^{\,2} - 200\, L\_2\,\omega\, L\_1 + 100\,\omega^3\, L\_2\, c\, L\_1^{\,2} - I\,\omega^2\, L\_2\, L\_1^{\,2} - 5000\, I\,\omega^2\, c\, L\_1^{\,2} + 10000\, I\, L\_1 - 10000\, I\, L\_2\,\omega^2\, c\, L\_1 + 10000\, I\, L\_2 + 2500\, I\,\omega^4\, c^2\, L\_1^{\,2}\, L\_2)$$

```
> ABCD_even := simplify(evalm(&*(shC, seL, shC)));
```

$$ABCD\_even := \begin{bmatrix} -\omega^2\, L\_2\, c + 1 & I\,\omega\, L\_2 \\ 2\, I\,\omega\, c - I\,\omega^3\, c^2\, L\_2 & -\omega^2\, L\_2\, c + 1 \end{bmatrix}$$

```
> Gamma_Even := ( (ABCD_even[1,1]-ABCD_even[2,2]) + (ABCD_even[1,2]/50-ABCD_even[2,1]*50
)/( (ABCD_even[1,1]+ABCD_even[2,2]) + (ABCD_even[1,2]/50+ABCD_even[2,1]*50)
) ;
```

$$Gamma\_Even := \frac{\frac{1}{50}\, I\,\omega\, L\_2 - 100\, I\,\omega\, c + 50\, I\,\omega^3\, c^2\, L\_2}{-2\,\omega^2\, L\_2\, c + 2 + \frac{1}{50}\, I\,\omega\, L\_2 + 100\, I\,\omega\, c - 50\, I\,\omega^3\, c^2\, L\_2}$$

```
> T_even := 2/( (ABCD_even[1,1]+ABCD_even[2,2]) + (ABCD_even[1,2]/50+ABCD_even[2,1]*50)
);
```

$$T\_even := 2\,\frac{1}{-2\,\omega^2\, L\_2\, c + 2 + \frac{1}{50}\, I\,\omega\, L\_2 + 100\, I\,\omega\, c - 50\, I\,\omega^3\, c^2\, L\_2}$$

```
> S11 :=simplify((Gamma_Even + Gamma_Odd)/2);
```

$$S11 := -I(-100\, L\_2^{\,2}\,\omega^2\, L\_1 - 500000\, L\_1 - 500000\, L\_2 + 1500000\, L\_2\,\omega^2\, c\, L\_1 + 500000\,\omega^2\, c\, L\_1^{\,2} - 750000\,\omega^4\, c^2\, L\_1^{\,2}\, L\_2 - 100\,\omega^2\, L\_2\, L\_1^{\,2} + 75000000\, I\, L\_2\,\omega^3\, c^2\, L\_1 - 25000000\, I\,\omega^5\, c^3\, L\_1^{\,2}\, L\_2 - 25000000\, I\,\omega^5\, c^3\, L\_2^{\,2}\, L\_1 + 6250000\, I\,\omega^7\, c^4\, L\_2^{\,2}\, L\_1^{\,2} + 25000000\, I\,\omega^3\, c^2\, L\_1^{\,2} - 750000\,\omega^4\, c^2\, L\_2^{\,2}\, L\_1 + 250000\,\omega^6\, c^3\, L\_2^{\,2}\, L\_1^{\,2} + 25000000\, I\,\omega^3\, c^2\, L\_2^{\,2} - 50000000\, I\,\omega\, c\, L\_2 - 50000000\, I\,\omega\, c\, L\_1 + 100\,\omega^4\, L\_2^{\,2}\, c\, L\_1^{\,2} - I\,\omega^3\, L\_2^{\,2}\, L\_1^{\,2} + 500000\,\omega^2\, L\_2^{\,2}\, c) \Big/ ((100\,\omega^2\, L\_2\, c - 100 - I\,\omega\, L\_2 - 5000\, I\,\omega\, c + 2500\, I\,\omega^3\, c^2\, L\_2)(-100\,\omega\, L\_1^{\,2} - 200\, L\_2\,\omega\, L\_1 + 100\,\omega^3\, L\_2\, c\, L\_1^{\,2} - I\,\omega^2\, L\_2\, L\_1^{\,2} - 5000\, I\,\omega^2\, c\, L\_1^{\,2} + 10000\, I\, L\_1 - 10000\, I\, L\_2\,\omega^2\, c\, L\_1 + 10000\, I\, L\_2 + 2500\, I\,\omega^4\, c^2\, L\_1^{\,2}\, L\_2))$$

```
> S12 := simplify((T_even+T_odd)/2);
```

$$S12 := -100(-100\,\omega\, L\_1^{\,2} - 100\, L\_2\,\omega\, L\_1 + 100\,\omega^3\, L\_2\, c\, L\_1^{\,2} - I\,\omega^2\, L\_2\, L\_1^{\,2} - 5000\, I\,\omega^2\, c\, L\_1^{\,2} + 5000\, I\, L\_1 - 5000\, I\, L\_2\,\omega^2\, c\, L\_1 + 5000\, I\, L\_2 + 2500\, I\,\omega^4\, c^2\, L\_1^{\,2}\, L\_2) \Big/ ((100\,\omega^2\, L\_2\, c - 100 - I\,\omega\, L\_2 - 5000\, I\,\omega\, c + 2500\, I\,\omega^3\, c^2\, L\_2)(-100\,\omega\, L\_1^{\,2} - 200\, L\_2\,\omega\, L\_1 + 100\,\omega^3\, L\_2\, c\, L\_1^{\,2} - I\,\omega^2\, L\_2\, L\_1^{\,2} - 5000\, I\,\omega^2\, c\, L\_1^{\,2} + 10000\, I\, L\_1 - 10000\, I\, L\_2\,\omega^2\, c\, L\_1 + 10000\, I\, L\_2 + 2500\, I\,\omega^4\, c^2\, L\_1^{\,2}\, L\_2))$$

```
> S13 := simplify((T_even-T_odd)/2);
```

$$S13 := 10000(L\_2\,\omega\,L\_1 - 50\,I\,L\_1 + 50\,I\,L\_2\,\omega^2\,c\,L\_1 - 50\,I\,L\_2) \Big/ ($$
$$(100\,\omega^2\,L\_2\,c - 100 - I\,\omega\,L\_2 - 5000\,I\,\omega\,c + 2500\,I\,\omega^3\,c^2\,L\_2)(-100\,\omega\,L\_1{}^2$$
$$- 200\,L\_2\,\omega\,L\_1 + 100\,\omega^3\,L\_2\,c\,L\_1{}^2 - I\,\omega^2\,L\_2\,L\_1{}^2 - 5000\,I\,\omega^2\,c\,L\_1{}^2$$
$$+ 10000\,I\,L\_1 - 10000\,I\,L\_2\,\omega^2\,c\,L\_1 + 10000\,I\,L\_2 + 2500\,I\,\omega^4\,c^2\,L\_1{}^2\,L\_2))$$

```
> S14 := simplify((Gamma_Even-Gamma_Odd)/2);
```

$$S14 := -100I(-L\_2{}^2\,\omega^2\,L\_1 + 5000\,L\_1 + 5000\,L\_2 - 5000\,L\_2\,\omega^2\,c\,L\_1$$
$$+ 2500\,\omega^4\,c^2\,L\_2{}^2\,L\_1 - 5000\,\omega^2\,L\_2{}^2\,c + 100\,I\,\omega\,L\_2{}^2 - 100\,I\,L\_2{}^2\,\omega^3\,c\,L\_1$$
$$+ 100\,I\,\omega\,L\_2\,L\_1) \Big/ ($$
$$(100\,\omega^2\,L\_2\,c - 100 - I\,\omega\,L\_2 - 5000\,I\,\omega\,c + 2500\,I\,\omega^3\,c^2\,L\_2)(-100\,\omega\,L\_1{}^2$$
$$- 200\,L\_2\,\omega\,L\_1 + 100\,\omega^3\,L\_2\,c\,L\_1{}^2 - I\,\omega^2\,L\_2\,L\_1{}^2 - 5000\,I\,\omega^2\,c\,L\_1{}^2$$
$$+ 10000\,I\,L\_1 - 10000\,I\,L\_2\,\omega^2\,c\,L\_1 + 10000\,I\,L\_2 + 2500\,I\,\omega^4\,c^2\,L\_1{}^2\,L\_2))$$

Since the branch-line coupler circuit is symmetrical, $S_{12} = S_{21}$, $S_{13} = S_{31}$, and $S_{14} = S_{41}$.

B.2 S-Parameter Equations for the Lumped Element Rat-Race Coupler

The even and odd mode analysis and the S-Parameter equations for the rat-race coupler are provided in this section. Maple V Release 5 was used for simplification of the analysis and equations. The definitions of the symbols used in the equations are provided below. For the rat-race coupler with a zero degree phase difference between output ports 2 and 3 the coupler ports and lumped elements were labeled as shown in Figure B.1.

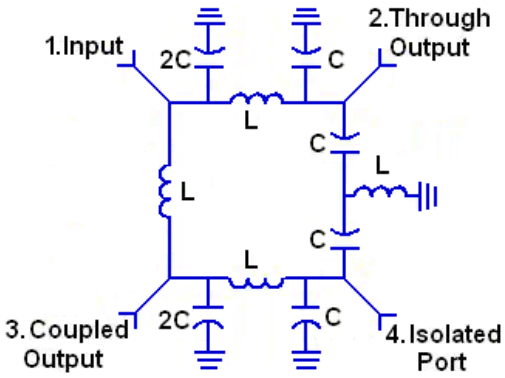

Figure B.1: Rat-Race Coupler with Zero Degree Phase Shift between Output Ports 2 and 3

C: capacitor

2C: a capacitor of double C's value

sh_2C: shunt capacitor with double C's value

I: imaginary number, commonly known as j or i

ω: radian frequency, 2πf, where f is the frequency in Hz.

se_L: series inductor

L: inductor

sh_2C: shunt capacitor that is double C's value

sh_C: shunt capacitor

shC_2Lse: shunt capactor with a series inductor of that is the double the value of L

Gamma(even /odd): Even/Odd Reflection Coefficient

T(even/odd): Even/Odd Transmission Coefficient

```
> sh_2C := matrix([ [1,0], [I*2*omega*C,1] ]);
```

$$sh\_2C := \begin{bmatrix} 1 & 0 \\ 2\,I\,\omega\,C & 1 \end{bmatrix}$$

```
> se_L := matrix([ [1, I*omega*L], [0,1] ]);
```

$$se\_L := \begin{bmatrix} 1 & I\,\omega\,L \\ 0 & 1 \end{bmatrix}$$

```
> sh_C := matrix([ [1,0], [I*omega*C,1] ]);
```

$$sh\_C := \begin{bmatrix} 1 & 0 \\ I\,\omega\,C & 1 \end{bmatrix}$$

```
> sh_C2Lse := matrix([ [1,0], [I*omega*C/(1-2*omega^2*L*C),1] ]);
```

$$sh\_C2Lse := \begin{bmatrix} 1 & 0 \\ \dfrac{I\,\omega\,C}{1-2\,\omega^2\,L\,C} & 1 \end{bmatrix}$$

```
> ABCD_even := evalm(&*(sh_2C, se_L, sh_C, sh_C2Lse));
```

$$ABCD\_even := \begin{bmatrix} 1-\omega^2\,L\,C-\dfrac{\omega^2\,L\,C}{1-2\,\omega^2\,L\,C} & I\,\omega\,L \\ 3\,I\,\omega\,C+I\,(1-2\,\omega^2\,L\,C)\,\omega\,C & 1-2\,\omega^2\,L\,C \end{bmatrix}$$

```
> Gamma_even := simplify(( (ABCD_even[1,1]-ABCD_even[2,2]) + (ABCD_even[1,2]/50
- ABCD_even[2,1]*50) )/( (ABCD_even[1,1]+ABCD_even[2,2]) + (ABCD_even[1,2]/50
+ ABCD_even[2,1]*50) ));
```

$$Gamma\_even := -\omega(100\,\omega^3\,L^2\,C^2-I\,L+2\,I\,L^2\,\omega^2\,C+10000\,I\,C-25000\,I\,C^2\,\omega^2\,L$$
$$+10000\,I\,C^3\,\omega^4\,L^2)\Big/(100-400\,\omega^2\,L\,C+300\,\omega^4\,L^2\,C^2+I\,\omega\,L-2\,I\,\omega^3\,L^2\,C$$
$$+10000\,I\,\omega\,C-25000\,I\,\omega^3\,C^2\,L+10000\,I\,\omega^5\,C^3\,L^2)$$

```
> T_even := simplify(2/( (ABCD_even[1,1]+ABCD_even[2,2]) + (ABCD_even[1,2]/50+ABCD_even
));
```

$$T\_even := -100(-1+2\,\omega^2\,L\,C)\Big/(100-400\,\omega^2\,L\,C+300\,\omega^4\,L^2\,C^2+I\,\omega\,L$$
$$-2\,I\,\omega^3\,L^2\,C+10000\,I\,\omega\,C-25000\,I\,\omega^3\,C^2\,L+10000\,I\,\omega^5\,C^3\,L^2)$$

```
> sh_halfL := matrix( [ [1,0], [-2*I/(omega*L),1] ] );
```

$$sh\_halfL := \begin{bmatrix} 1 & 0 \\ -2\,\dfrac{I}{\omega\,L} & 1 \end{bmatrix}$$

```
> ABCD_odd := simplify(evalm(&*(sh_halfL, sh_2C, se_L, sh_2C)));
```

$$ABCD\_odd := \begin{bmatrix} 1-2\,\omega^2\,L\,C & I\,\omega\,L \\ -2\,\dfrac{I\,(1-4\,\omega^2\,L\,C+2\,\omega^4\,L^2\,C^2)}{\omega\,L} & 3-2\,\omega^2\,L\,C \end{bmatrix}$$

```
> Gamma_Odd := simplify(( (ABCD_odd[1,1]-ABCD_odd[2,2]) + (ABCD_odd[1,2]/
- ABCD_odd[2,1]*50) )/( (ABCD_odd[1,1]+ABCD_odd[2,2]) + (ABCD_odd[1,2]/50
+ ABCD_odd[2,1]*50) ));
```

$$Gamma\_Odd := -\frac{-100\,\omega\,L + I\,\omega^2\,L^2 + 5000\,I - 20000\,I\,\omega^2\,C\,L + 10000\,I\,\omega^4\,L^2\,C^2}{-200\,\omega\,L + 200\,\omega^3\,L^2\,C - I\,\omega^2\,L^2 + 5000\,I - 20000\,I\,\omega^2\,C\,L + 10000\,I\,\omega^4\,L^2\,C^2}$$

```
> T_odd := simplify(2/( (ABCD_odd[1,1]+ABCD_odd[2,2]) + (ABCD_odd[1,2]/50
+ ABCD_odd[2,1]*50) ));
```

$$T\_odd := -100\,\frac{\omega\,L}{-200\,\omega\,L + 200\,\omega^3\,L^2\,C - I\,\omega^2\,L^2 + 5000\,I - 20000\,I\,\omega^2\,C\,L + 10000\,I\,\omega^4\,L^2\,C^2}$$

```
> S11 :=simplify((Gamma_even + Gamma_Odd)/2);
```

$$\begin{aligned} S11 := {} & (-100\,I\,\omega^2\,L^2 + L^3\,\omega^3 + 3500000\,I\,\omega^2\,C\,L + 25000\,\omega^5\,L^3\,C^2 - 10000\,\omega^7\,L^4\,C^3 \\ & - 10250000\,I\,\omega^4\,L^2\,C^2 - 250000\,I + 50000000\,\omega\,C + 5000\,\omega\,L - 20000\,\omega^3\,L^2\,C \\ & - 325000000\,C^2\,\omega^3\,L + 650000000\,C^3\,\omega^5\,L^2 - 450000000\,C^4\,\omega^7\,L^3 \\ & + 100000000\,C^5\,\omega^9\,L^4 - 2\,L^4\,\omega^5\,C - 300\,I\,\omega^6\,L^4\,C^2 + 10000000\,I\,\omega^6\,L^3\,C^3 \\ & - 3000000\,I\,\omega^8\,L^4\,C^4 + 400\,I\,L^3\,\omega^4\,C) \Big/ ((100 - 400\,\omega^2\,L\,C + 300\,\omega^4\,L^2\,C^2 \\ & + I\,\omega\,L - 2\,I\,\omega^3\,L^2\,C + 10000\,I\,\omega\,C - 25000\,I\,\omega^3\,C^2\,L + 10000\,I\,\omega^5\,C^3\,L^2) \\ & (-200\,\omega\,L + 200\,\omega^3\,L^2\,C - I\,\omega^2\,L^2 + 5000\,I - 20000\,I\,\omega^2\,C\,L + 10000\,I\,\omega^4\,L^2\,C^2)) \end{aligned}$$

```
> S12 := simplify((T_even+T_odd)/2);
```

$$\begin{aligned} S12 := {} & -100(150\,\omega\,L - 500\,\omega^3\,L^2\,C + I\,\omega^2\,L^2 - 2500\,I + 20000\,I\,\omega^2\,C\,L \\ & - 37500\,I\,\omega^4\,L^2\,C^2 + 350\,\omega^5\,L^3\,C^2 - 2\,I\,L^3\,\omega^4\,C + 15000\,I\,\omega^6\,L^3\,C^3) \Big/ ((100 \\ & - 400\,\omega^2\,L\,C + 300\,\omega^4\,L^2\,C^2 + I\,\omega\,L - 2\,I\,\omega^3\,L^2\,C + 10000\,I\,\omega\,C \\ & - 25000\,I\,\omega^3\,C^2\,L + 10000\,I\,\omega^5\,C^3\,L^2) \\ & (-200\,\omega\,L + 200\,\omega^3\,L^2\,C - I\,\omega^2\,L^2 + 5000\,I - 20000\,I\,\omega^2\,C\,L + 10000\,I\,\omega^4\,L^2\,C^2)) \end{aligned}$$

```
> S13 := simplify((Gamma_even-Gamma_Odd)/2);
```

$$\begin{aligned} S13 := {} & -100(I\,\omega^2\,L^2 + 100\,\omega\,L + 15000\,I\,\omega^2\,C\,L + 300\,\omega^5\,L^3\,C^2 - 27500\,I\,\omega^4\,L^2\,C^2 \\ & - 2500\,I - 400\,\omega^3\,L^2\,C + 10000\,I\,\omega^6\,L^3\,C^3 - 2\,I\,L^3\,\omega^4\,C) \Big/ ((100 - 400\,\omega^2\,L\,C \\ & + 300\,\omega^4\,L^2\,C^2 + I\,\omega\,L - 2\,I\,\omega^3\,L^2\,C + 10000\,I\,\omega\,C - 25000\,I\,\omega^3\,C^2\,L \\ & + 10000\,I\,\omega^5\,C^3\,L^2) \\ & (-200\,\omega\,L + 200\,\omega^3\,L^2\,C - I\,\omega^2\,L^2 + 5000\,I - 20000\,I\,\omega^2\,C\,L + 10000\,I\,\omega^4\,L^2\,C^2)) \end{aligned}$$

```
> S14 := simplify((T_even-T_odd)/2);
```

$$\begin{aligned} S14 := {} & -5000(\omega\,L - 2\,\omega^3\,L^2\,C - 50\,I + 200\,I\,\omega^2\,C\,L - 250\,I\,\omega^4\,L^2\,C^2 + \omega^5\,L^3\,C^2 \\ & + 100\,I\,\omega^6\,L^3\,C^3) \Big/ ((100 - 400\,\omega^2\,L\,C + 300\,\omega^4\,L^2\,C^2 + I\,\omega\,L - 2\,I\,\omega^3\,L^2\,C \\ & + 10000\,I\,\omega\,C - 25000\,I\,\omega^3\,C^2\,L + 10000\,I\,\omega^5\,C^3\,L^2) \\ & (-200\,\omega\,L + 200\,\omega^3\,L^2\,C - I\,\omega^2\,L^2 + 5000\,I - 20000\,I\,\omega^2\,C\,L + 10000\,I\,\omega^4\,L^2\,C^2)) \end{aligned}$$

Since the rat-race coupler circuit is symmetrical, $S_{12} = S_{21}$, $S_{13} = S_{31}$, and $S_{14} = S_{41}$.

For the rat-race coupler with a 180 degree phase difference between output ports 2 and 3 the coupler ports and lumped elements were labeled as shown in Figure B.2. The definitions of the symbols are the same as the rat-race coupler with zero degree phase difference between output ports 2 and 3.

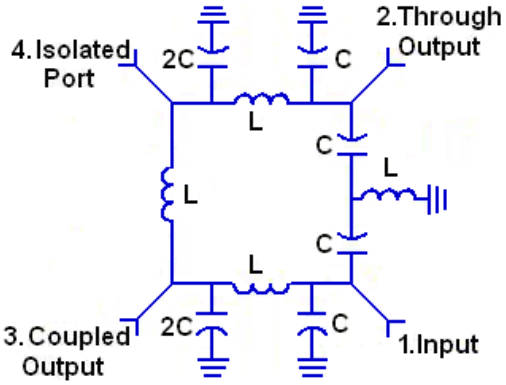

Figure B.2: Lumped Element Rat-Race Coupler with 180 Degree Phase Shift Between Output Ports 2 and 3

```
> sh_2C := matrix([ [1,0], [I*2*omega*C,1] ]);
```

$$sh\_2C := \begin{bmatrix} 1 & 0 \\ 2\,I\,\omega\,C & 1 \end{bmatrix}$$

```
> se_L := matrix([ [1, I*omega*L], [0,1] ]);
```

$$se\_L := \begin{bmatrix} 1 & I\,\omega\,L \\ 0 & 1 \end{bmatrix}$$

```
> sh_C := matrix([ [1,0], [I*omega*C,1] ]);
```

$$sh\_C := \begin{bmatrix} 1 & 0 \\ I\,\omega\,C & 1 \end{bmatrix}$$

```
> sh_C2Lse := matrix([ [1,0], [I*omega*C/(1-2*omega^2*L*C),1] ]);
```

$$sh\_C2Lse := \begin{bmatrix} 1 & 0 \\ \dfrac{I\,\omega\,C}{1-2\,\omega^2\,L\,C} & 1 \end{bmatrix}$$

```
> ABCD_even := evalm(&*(sh_C2Lse, sh_C, se_L, sh_2C));
```

$$ABCD\_even := \left[1-2\,\omega^2\,L\,C,\ I\,\omega\,L\right],\left[\frac{I\,\omega\,C}{1-2\,\omega^2\,L\,C}+I\,\omega\,C+2\,I\,(I\,(\frac{I\,\omega\,C}{1-2\,\omega^2\,L\,C}+I\,\omega\,C)\,\omega\,L+1)\,\omega\,C,\ I\,(\frac{I\,\omega\,C}{1-2\,\omega^2\,L\,C}+I\,\omega\,C)\,\omega\,L+1\right]$$

```
> sh_L_over_2 := matrix([ [1,0], [-2*I/(omega*L),1] ]);
```

$$sh\_L\_over\_2 := \begin{bmatrix} 1 & 0 \\ -2\dfrac{I}{\omega L} & 1 \end{bmatrix}$$

```
> ABCD_odd := evalm(&*(sh_2C,se_L,sh_2C,sh_L_over_2));
```

$$ABCD\_odd := \begin{bmatrix} 3-2\omega^2 L C & I\omega L \\ 2I\omega C + 2I(1-2\omega^2 L C)\omega C - 2\dfrac{I(1-2\omega^2 L C)}{\omega L} & 1-2\omega^2 L C \end{bmatrix}$$

```
> Gamma_even := simplify(( (ABCD_even[1,1]-ABCD_even[2,2]) + (ABCD_even[1,2]/50
- ABCD_even[2,1]*50) )/( (ABCD_even[1,1]+ABCD_even[2,2]) + (ABCD_even[1,2]/50
+ ABCD_even[2,1]*50) ));
```

$$Gamma\_even := -\omega(-100\omega^3 L^2 C^2 - I L + 2I L^2 \omega^2 C + 10000 I C - 25000 I C^2 \omega^2 L + 10000 I C^3 \omega^4 L^2) \Big/ (100 - 400\omega^2 L C + 300\omega^4 L^2 C^2 + I\omega L - 2I\omega^3 L^2 C + 10000 I\omega C - 25000 I\omega^3 C^2 L + 10000 I\omega^5 C^3 L^2)$$

```
> T_even := simplify(2/( (ABCD_even[1,1]+ABCD_even[2,2]) + (ABCD_even[1,2]/50+ABCD_even
));
```

$$T\_even := -100(-1+2\omega^2 L C) \Big/ (100 - 400\omega^2 L C + 300\omega^4 L^2 C^2 + I\omega L - 2I\omega^3 L^2 C + 10000 I\omega C - 25000 I\omega^3 C^2 L + 10000 I\omega^5 C^3 L^2)$$

```
> Gamma_Odd := simplify(( (ABCD_odd[1,1]-ABCD_odd[2,2]) + (ABCD_odd[1,2]/50
- ABCD_odd[2,1]*50) )/( (ABCD_odd[1,1]+ABCD_odd[2,2]) + (ABCD_odd[1,2]/50
+ ABCD_odd[2,1]*50) ));
```

$$Gamma\_Odd := -\frac{100\omega L + I\omega^2 L^2 - 20000 I\omega^2 C L + 10000 I\omega^4 C^2 L^2 + 5000 I}{-200\omega L + 200\omega^3 L^2 C - I\omega^2 L^2 - 20000 I\omega^2 C L + 10000 I\omega^4 C^2 L^2 + 5000 I}$$

```
> T_odd := simplify(2/( (ABCD_odd[1,1]+ABCD_odd[2,2]) + (ABCD_odd[1,2]/50
+ ABCD_odd[2,1]*50) ));
```

$$T\_odd := -100 \frac{\omega L}{-200\omega L + 200\omega^3 L^2 C - I\omega^2 L^2 - 20000 I\omega^2 C L + 10000 I\omega^4 C^2 L^2 + 5000 I}$$

```
> S11 := simplify((Gamma_even+Gamma_Odd)/2);
```

$$S11 := (50000000\omega C + L^3\omega^3 - 200 I\omega^2 L^2 - 25000\omega^5 L^3 C^2 - 5000\omega L + 10000\omega^7 L^4 C^3 - 250000 I + 2500000 I\omega^2 C L - 7250000 I\omega^4 C^2 L^2 + 20000\omega^3 L^2 C - 400 I\omega^6 L^4 C^2 + 7000000 I\omega^6 L^3 C^3 - 2000000 I\omega^8 L^4 C^4 + 600 I L^3\omega^4 C - 2L^4\omega^5 C - 325000000\omega^3 C^2 L + 650000000\omega^5 C^3 L^2 - 450000000 C^4\omega^7 L^3 + 100000000 C^5\omega^9 L^4) \Big/ ((100 - 400\omega^2 L C + 300\omega^4 L^2 C^2 + I\omega L - 2I\omega^3 L^2 C + 10000 I\omega C - 25000 I\omega^3 C^2 L + 10000 I\omega^5 C^3 L^2)(-200\omega L + 200\omega^3 L^2 C - I\omega^2 L^2 - 20000 I\omega^2 C L + 10000 I\omega^4 C^2 L^2 + 5000 I))$$

```
> S12 := simplify((Gamma_even-Gamma_Odd)/2);
```

$$S12 := 100(-200\,\omega^5 L^3 C^2 + 200\,\omega^7 L^4 C^3 + 2500\,I - 5000\,I\,\omega^2 C\,L + 7500\,I\,\omega^4 C^2 L^2 - I\,\omega^6 L^4 C^2 - 20000\,I\,\omega^6 L^3 C^3 + 10000\,I\,\omega^8 L^4 C^4) \Big/ ((100 - 400\,\omega^2 L\,C + 300\,\omega^4 L^2 C^2 + I\,\omega\,L - 2\,I\,\omega^3 L^2 C + 10000\,I\,\omega\,C - 25000\,I\,\omega^3 C^2 L + 10000\,I\,\omega^5 C^3 L^2)(-200\,\omega\,L + 200\,\omega^3 L^2 C - I\,\omega^2 L^2 - 20000\,I\,\omega^2 C\,L + 10000\,I\,\omega^4 C^2 L^2 + 5000\,I))$$

```
> S13 := simplify((T_even+T_odd)/2);
```

$$S13 := -100(150\,\omega\,L - 500\,\omega^3 L^2 C + I\,\omega^2 L^2 + 20000\,I\,\omega^2 C\,L - 37500\,I\,\omega^4 C^2 L^2 - 2500\,I + 350\,\omega^5 L^3 C^2 - 2\,I\,L^3\omega^4 C + 15000\,I\,\omega^6 L^3 C^3) \Big/ ((100 - 400\,\omega^2 L\,C + 300\,\omega^4 L^2 C^2 + I\,\omega\,L - 2\,I\,\omega^3 L^2 C + 10000\,I\,\omega\,C - 25000\,I\,\omega^3 C^2 L + 10000\,I\,\omega^5 C^3 L^2)(-200\,\omega\,L + 200\,\omega^3 L^2 C - I\,\omega^2 L^2 - 20000\,I\,\omega^2 C\,L + 10000\,I\,\omega^4 C^2 L^2 + 5000\,I))$$

```
> S14 := simplify((T_even-T_odd)/2);
```

$$S14 := -5000(\omega\,L - 2\,\omega^3 L^2 C + 200\,I\,\omega^2 C\,L - 250\,I\,\omega^4 C^2 L^2 - 50\,I + \omega^5 L^3 C^2 + 100\,I\,\omega^6 L^3 C^3) \Big/ ((100 - 400\,\omega^2 L\,C + 300\,\omega^4 L^2 C^2 + I\,\omega\,L - 2\,I\,\omega^3 L^2 C + 10000\,I\,\omega\,C - 25000\,I\,\omega^3 C^2 L + 10000\,I\,\omega^5 C^3 L^2)(-200\,\omega\,L + 200\,\omega^3 L^2 C - I\,\omega^2 L^2 - 20000\,I\,\omega^2 C\,L + 10000\,I\,\omega^4 C^2 L^2 + 5000\,I))$$

Since the rat-race coupler circuit is symmetrical, $S_{12} = S_{21}$, $S_{13} = S_{31}$, and $S_{14} = S_{41}$.

APPENDIX C
MASK LAYOUTS

The layout of mask 1 and mask 2 are provided in this appendix.

C.1 Layout of Mask 1

The layout of mask 1 is shown in Figure C.1. Each of the coupler structures is labeled 1 through 12.

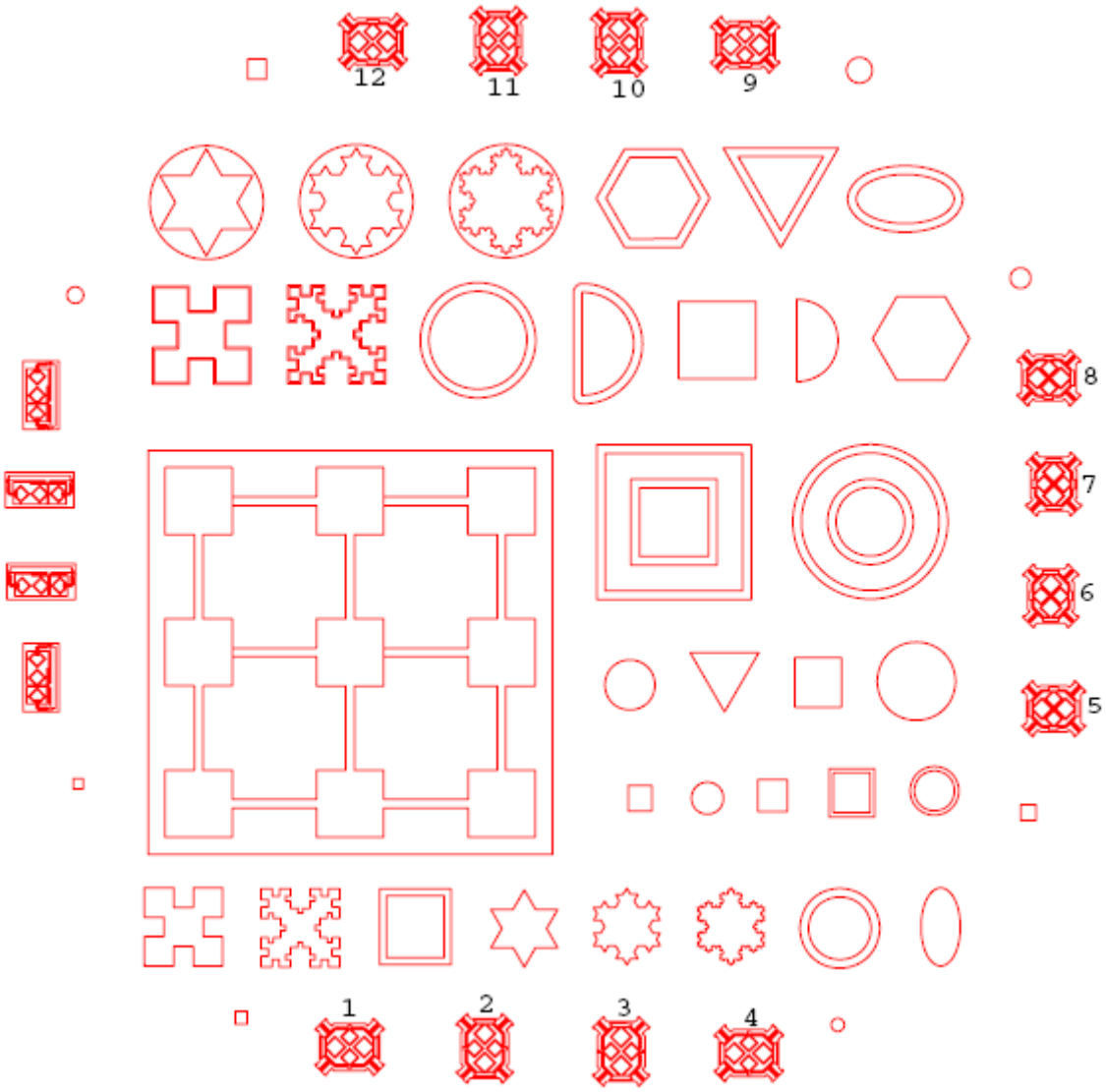

Figure C.1: Layout of Mask 1

C.2 Layout of Mask 2

The layout of mask 2 is provided in Figure C.2. Each of the coupler structures is labeled 1 through 17.

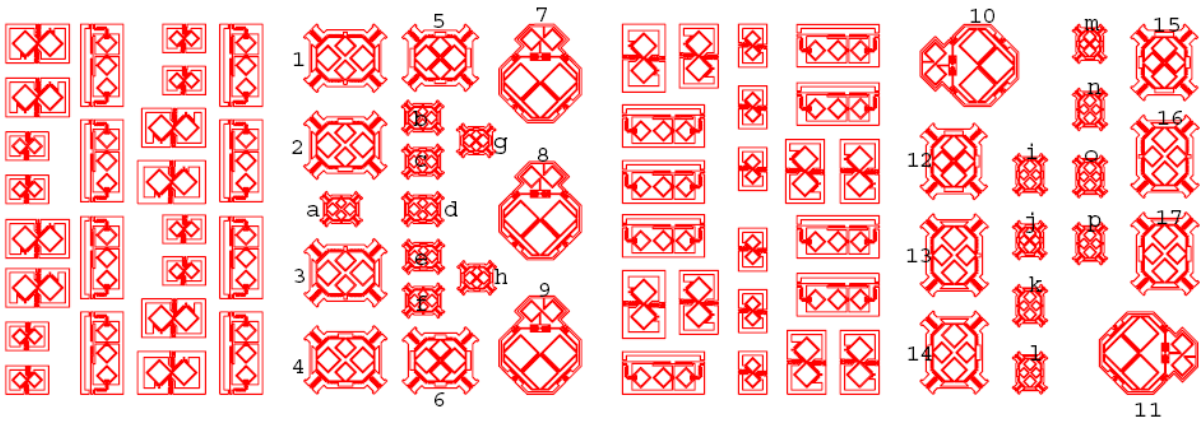

Figure C.2: Layout of Mask 2

.